Exploiting Simultaneous Transmitting and Reflecting Reconfigurable Intelligent Surfaces (STAR-RISs) in Wireless Communications

by

Jiaqi Xu

Doctor of Philosophy

School of Electronic Engineering and Computer Science
Queen Mary University of London
United Kingdom

May 2023

TO MY FAMILY

Acknowledgments

Foremost, I would like to express my sincere gratitude to my supervisors, Dr. Yuanwei Liu, Dr. Yue Chen, Dr. Andrea Cavallaro, and Dr. Joey Tianyi Zhou, for their continuous support of my Ph.D research. Special thanks to my primary supervisor, Dr. Yuanwei Liu, who provided valuable technical guidance and constructive suggestions on my research works and directions. During the past four years, working with Dr. Liu has been a wonderful experience. His wide knowledge, strong research enthusiasm and hard-working attitude have inspired me during all my PhD period, and will have a profound effect on my future carrier.

I would like to thank all my collaborators: Prof. Robert Schober, Prof. H. Vincent Poor, Prof. Octavia A. Dobre, Prof. Marco Di Renzo, Prof. Naofal Al-Dhahir, Prof. Lajos Hanzo, Prof. Yang Hao, Prof. Lingyang Song, and Dr. Xidong Mu for their helpful suggestions and comments on my research. I would like to special thank Dr. Joey Tianyi Zhou for hosting my visit in A*STAR, Singapore.

Last and the most importantly, I would like to express my deepest gratitude to my beloved wife, parents, and grandparents, who always support me at any time. Meanwhile, this thesis is specially dedicated to my deeply loved maternal grandmother. May her soul rest in peace.

Abstract

As of 2023, wireless technology has become an essential part of work and life for people in most parts of the world. The concept of reconfigurable intelligent surfaces (RISs) as a means of manipulating the wireless communication channel emerged in early 2019. RISs are two-dimensional material structures composed of a large number of low-cost programmable elements. The introduction of RISs presents a paradigm shift in wireless transmissions, as it allows for beneficial reconfiguration of the wireless environment between transmitters and receivers. However, due to the nascent stage of RIS research and development, there exists a knowledge gap between the physical/hardware aspect and the communication aspect of RISs, posing challenges in performance analysis and system optimization for RIS-aided communication networks. This thesis leverages knowledge in Electromagnetics, antenna theory, and information theory to provide a review of the fundamentals of RISs. Building on the understanding of RISs, this thesis proposes and studies the novel concept of simultaneous transmitting and reflecting reconfigurable intelligent surface (STAR-RISs). Specifically, the device, channel, and signal modeling for STAR-RISs are the focus of this thesis. Based on the proposed models, the performance of STAR-RIS in terms of their power scaling law, diversity gain, multiplexing gain, and coverage are analyzed.

First, this thesis proposes the novel concept of STAR-RIS. To investigate the performance of STAR-RIS-aided wireless communications, independent and correlated transmission and reflection phase-shift models are proposed. Furthermore, considering a STAR-RIS-aided two-user communication system employing orthogonal multiple access (OMA) and non-orthogonal multiple access (NOMA), three practical phase-shift configuration strategies are introduced. To evaluate and compare the performance achieved with different STAR-RIS phase-shift configuration strategies, the asymptotic behavior of the outage probabilities for both OMA and NOMA are derived. Moreover, the diversity orders

and the power scaling laws for the considered phase-shift configuration strategies are investigated.

Second, this thesis investigates two STAR-RIS variants: the dual-sided STAR-RISs and the active STAR-RISs. Hardware models and signal models are proposed for both variants. For dual-sided STAR-RISs, expressions for the outage probability of a STAR-RIS assisted two-user uplink communication system in high transmit SNR regime are derived. It is also revealed that the error floor for the uplink NOMA transmission can be lowered by adjusting the power ratios of STAR elements. For active STAR-RISs, expressions for the asymptotic received SNRs and outage probabilities of both users for the case of coupled phase-shift and independent phase-shift are derived. It is proved that both user can achieve full diversity order under independent phase-shift active STAR-RIS.

Third and last, a channel model based on Green's function method is proposed for investigating the performance limit of metasurface-based STAR-RISs. Instead of modeling the RIS elements with the transmission and reflection coefficients, this thesis uses the distribution of the induced electric currents within the metasurface-based RIS. This thesis reveals how transmitting-only RISs, reflecting-only RISs and STAR-RISs can be achieved by configuring the distribution of the induced electric current. For the single-user scenario with transmitting/reflecting-only RISs, the upper bound of the end-to-end channel gain is derived by choosing the current distribution that is optimized for the receiver. In addition, the position of the near-field and far-field boundary, the maximum DoF of the channel, and the power scaling law are derived. It was shown that the size of RIS, the carrier signal frequency, and the size of the receiver all affect the above performance metrics.

Table of Contents

List of Figures

List of Tables

List of Abbreviations

AF/DF	Amplify-and-Forward/Decode-and-Forward
AWGN	Additive White Gaussian Noise
BER	Bit Error Rate
BS	Base Station
CLT	Central Limit Theorem
DoF	Degree-of-Freedom
EM	Electromagnetic
eMBB	Enhanced Mobile Broadband
FD	Full-Duplex
FDMA	Frequency-Division Multiple Access
FPGA	Field-Programmable Gate Array
ISAC	Integrated Sensing and Communication
LIS	Large Intelligent Surface
LoS	Line-of-Sight
MIMO	Multiple-Input and Multiple-Output
MISO	Multiple-Input and Single-Output
mMTC	Massive Machine-Type Communications
MS	Mode Switching
NFC	Near-Field Communications
NLoS	Non-Line-of-Sight
NOMA	Non-Orthogonal Multiple Access

OMA	Orthogonal Multiple Access
PDF	Probability Density Function
PIN	Positive-Intrinsic-Negative
PLS	Physical Layer Security
PSC	Phase-Shift Configuration
RF	Radio Frequency
RIS	Reconfigurable Intelligent Surfaces
Rx	Receiver
SEP	Surface Equivalence Principle
SIC	Successive Interference Cancellation
SINR	Signal-to-Interference-Plus-Noise Ratio
SNR	Signal-to-Noise Ratio
STAR	Simultaneous Transmitting and Reflecting
SRE	Smart Radio Environment
T&R	Transmission and Reflection
Tx	Transmitter
URLLC	Ultra-Reliable, Low Latency Communications
2D	Two-Dimensional
5G	Fifth-Generation
6G	Sixth-Generation

List of Mathematical Symbols

Symbol	Meaning	Section first use
A_e	area of RIS elements	3.2.1
α_0	path loss coefficient	3.2.1
β_m	amplitude response	2.2.2
c_R, c_T	power allocation coefficients	3.4.1
d	diversity order	3.7.2
D	directivity of antenna	5.2.3
ΔV_T	characteristic volume	5.3.1
D_{KL}	Kullback–Leibler divergence	4.1.2
$\mathbf{E}$	electric field	2.1.1
ϵ_0	free space permittivity	5.2.3
η_0	impedance of free space	3.2
$\mathbb{E}[x]$	expected value of x	3.8.2
$F(\mathbf{r}')$	focusing phase function	5.3.2
$F(\theta)$	leaning factor	3.2.1
G	amplifier gain	4.2.1
$\overline{\overline{\mathbf{G}}}(\mathbf{r}, \mathbf{r}')$	tensor Green's function	5.2.1
$\gamma_{r/t}$	target SNR	4.1.2
$\gamma_{\mathrm{transmit}}$	transmit SNR	4.1.2
G_{yy}	(y, y)-element of the Green's tensor	5.2.3
$\mathbf{H}$	magnetic field	2.1.1

H, h, g	wireless channels	2.4
$I_0(x)$	modified Bessel function of the first kind	3.8.2
$\mathbf{I}_2$	two-by-two identity matrix	4.2
j	imaginary unit	2.2.2
$\mathbf{J}_s$	electric current density	2.1.1
$J_y(\mathbf{r}')$	electric current in y direction	5.2.3
k_0	wave number	2.2.3
K_h	the Rician factor	3.4
$K(\mathbf{r}'_1, \mathbf{r}'_2)$	kernel function	5.2.3
$\mathbf{K}_s$	magnetic current density	2.1.1
λ	carrier wavelength	2.2.3
$\mathcal{L}\{f(x)\}$	Laplace transform of $f(x)$	4.2.3
M	number of RIS elements	3.3.2
μ_h	expected value of channel	3.8.2
μ_0	free space permeability	5.2.3
N	DoF of channel	5.3.3
N_R	number receive antenna	5.3.3
N_T	number of antenna elements	5.3.3
ν_m	the auxiliary bit	3.3.2
ω	signal frequency in radians	5.2.3
Ω_h	scale parameter of channel	4.2.2
ϕ_m	phase-shift	2.2.2
$\Phi(y)$	error function	4.1.2
P_{out}	outage probability	3.7.2
p, p_t, P_{BS}	transmit power	2.4
r_b	field boundary distance	5.3.1
ρ	correlation coefficient	4.1.2
R_m	reflection coefficient	2.2.2
R^{OMA}, R^{NOMA}	data rates	3.4.1

σ_0^2	variance of AWGN	3.4.1
σ_h^2	variance of channel	3.8.2
T_m	transmission coefficient	3.2
$U(Q)$	aperture distribution	3.2.1
V^-	output signal voltages	4.2.1
V^+	input signal voltage	4.2.1
$\mathrm{Var}[x]$	variance of x	3.8.2
V_R	volume of the receiver	5.2.1
V_T	volume of the STAR-RIS	5.2.1
W	energy of EM wave	3.3.2
$\mathbf{\Xi}_m$	T&R matrix	4.2
Z_{e}	electric impedance	3.2
Z_{m}	magnetic impedance	3.2

Chapter 1

Introduction

1.1 Background

1.1.1 On the Way to Sixth-Generation (6G)

The unprecedented demands for high quality and ubiquitous wireless services impose enormous challenges to existing cellular networks. Applications like rate-centric enhanced mobile broadband (eMBB), ultra-reliable, low latency communications (URLLC), and massive machine-type communications (mMTC) services are the targets for designing the fifth-generation (5G) of communication systems. However, the sixth-generation (6G) wireless communication networks are envisioned to deliver significant performance improvements beyond existing technologies [2]. The goals of the sixth-generation (6G) of wireless communication systems are expected to be transformative and revolutionary encompassing applications like data-driven, instantaneous, ultra-massive, and ubiquitous wireless connectivity. Therefore, new transmission technologies are needed in order to support these new applications and services.

1.1.2 Reconfigurable Intelligent Surfaces (RISs)

Reconfigurable intelligent surfaces (RISs) [3, 4] comprise an array of reflecting elements for reconfiguring the incident signals. Owing to their capability of proactively modifying the wireless communication environment, RISs have become a focal point of research in wireless communications to mitigate a wide range of challenges encountered in diverse wireless networks [5]. Through a smart controller (e.g., a field-programmable gate array (FPGA)) attached to the RIS, the phase and even the amplitude of these reconfigurable elements can be beneficially controlled, thus reconfiguring the propagation of the incident wireless signals and realizing a "Smart Radio Environment (SRE)" [6]. Since no radio frequency (RF) chains are required, RISs are more economical and environmentally friendly than conventional multi-antenna and relaying technologies. The advantages of RISs are listed as follows:

- **Easy to deploy:** RISs are nearly-passive devices, made of electromagnetic (EM) material. RISs can be deployed on several structures, including but not limited to building facades, indoor walls, aerial platforms, roadside billboards, highway polls, vehicle windows, as well as pedestrians' clothes due to their low-cost.

- **Spectral efficiency enhancement:** RISs are capable of reconfiguring the wireless propagation environment by compensating for the power loss over long distances. Virtual line-of-sight (LoS) links between base stations (BSs) and mobile users can be formed via passively reflecting the impinging radio signals. The throughput enhancement becomes more significant when the LoS link between BSs and users is blocked by e.g., high-rise buildings. Due to the intelligent deployment and design of RISs, a software-defined wireless environment may be constructed, which, in turn, provides potential enhancements of the received signal-to-interference-plus-noise ratio (SINR).

- **Environment friendly:** In contrast to conventional relaying systems, e.g., amplify-and-forward (AF) and decode-and-forward (DF) [7], RISs are capable of shaping

the incoming signal by controlling the phase shift of each reflecting element instead of employing a power amplifier [8]. Thus, deploying RISs is more energy-efficient and environment friendly than conventional AF and DF systems.

- **Compatibility:** RISs support full-duplex (FD) and full-band transmission due to the fact that they only reflect the EM waves. Additionally, RIS-enhanced wireless networks are compatible with the standards and hardware of existing wireless networks.

1.1.3 Simultaneous Transmitting and Reflecting Reconfigurable Intelligent Surfaces (STAR-RISs)

Despite the above-mentioned benefits, existing contributions mainly focus on RISs whose only function is to reflect an incident signal, hence both the source and the destination have to be at the same side of the RISs [3, 4], i.e., within the same *half-space* of the SRE. Unfortunately, this topological constraint limits the flexibility of employing conventional RISs. To address this issue, in 2021, we proposed the concept of simultaneous transmitting and reflecting RISs (STAR-RISs), where the incident wireless signals can be reflected within the half-space of the SRE at the same side of the RISs, but they can also be transmitted into the other side of the RISs. As a result, a *full-space* SRE can be created by STAR-RISs.

Considering the above unique feature, the use of STAR-RISs has the following advantages in wireless communication systems:

- Thanks to their capability of simultaneously transmitting and reflecting the incident signals, the coverage of STAR-RISs is extended to the entire space, thus serving both half-spaces using a single RIS, which is not possible for conventional reflecting-only RISs.

- STAR-RISs provide enhanced degrees-of-freedom (DoFs) for signal propagation manipulation, which significantly increases the design flexibility in satisfying strin-

gent communication requirements.

- Since STAR-RISs are generally designed to be optically transparent [9], they are aesthetically pleasing and readily compatible with existing building structures, such as windows. Therefore, STAR-RISs will have no undesired aesthetic effect, which is of vital importance for practical implementations.

1.2 Motivation and Contributions

Motivated by the aforementioned advantages of STAR-RISs, and along with the recent developments on RISs in general, this thesis spans the device modeling, channel modeling, and performance analysis of STAR-RISs. This thesis makes contributions to the field of wireless communications by focusing on the modeling and analysis of STAR-RISs. Through performance evaluations and simulations, the effectiveness of STAR-RISs in improving coverage, received power, and receiving diversity orders is demonstrated. This research provides valuable insights and practical solutions for harnessing the potential of RISs in future wireless communication networks.

More particularly, in the following technical chapters (Chapter. 3–5), the research of this thesis first proposes the independent and *correlated* transmission and reflection (T&R) phase-shift model for STAR-RISs. Based on the proposed models, the fundamental performance of STAR-RISs is compared with that of RISs. Secondly, this thesis discusses dual-sided STAR-RISs and active STAR-RISs, which are two types of STAR-RIS variants. Finally, it studies the metasurface-based STAR-RISs for which a continuous electric current distribution is used to capture their electromagnetic response instead of discrete phase-shift matrices. In contrast to the phase-shift characterization, the proposed Green's function-based channel modeling method reveals the best-achievable RIS-aided channel gain between the transmitter and receiver in both the near-field and far-field regimes.

1.3 Dissertation Organization

The remainder of this thesis is organized as follows. Chapter 2 introduces background information and fundamental principles, including Electromagnetics basics, RIS fundamentals, channel modeling methods, and principles of non-orthogonal multiple access (NOMA). Chapter 3 proposes independent and correlated T&R phase-shift models for STAR-RISs. This chapter is based on *publication 1* and *publication 4* as listed bellow. Chapter 4 studies two type of STAR-RIS variants: dual-sided STAR-RISs and active STAR-RISs. This chapter is based on *publication 5* and *publication 6*. Chapter 5 investigates near-field channel modeling of metasurface-based STAR-RISs which is based on *publication 7*. Finally, Chapter 6 concludes this thesis and discusses promising future research directions.

1.4 Author's Publications

1. **J. Xu**, Y. Liu, X. Mu, and O. A. Dobre, "STAR-RISs: Simultaneous Transmitting and Reflecting Reconfigurable Intelligent Surfaces", *IEEE Communications Letters*; vol. 25, no. 9, pp. 3134-3138, Sept. 2021.

2. **J. Xu**, Y. Liu, X. Mu, J. Zhou, L. Song, H. V. Poor, and L. Hanzo, "Simultaneously Transmitting and Reflecting (STAR) Intelligent Omni-Surfaces, Their Modeling and Implementation", *IEEE Vehicular Technology Magazine*; vol. 17, no. 2, pp. 46-54, June 2022.

3. **J. Xu** and Y. Liu, "A Novel Physics-based Channel Model for Reconfigurable Intelligent Surface-assisted Multi-user Communication Systems", *IEEE Transactions on Wireless Communications*; vol. 21, no. 2, pp. 1183-1196, Feb. 2022.

4. **J. Xu**, Y. Liu, X. Mu, and R. Schober "STAR-RISs with Correlated Phase-Shift Controls: Their Modeling and Practical Phase-Shift Designs", *IEEE Journal of Selected Topics in Signal Processing*; vol. 16, no. 5, pp. 1097-1111, Aug. 2022.

5. **J. Xu**, X. Mu, J. T. Zhou and Y. Liu, "Simultaneously Transmitting and Reflecting (STAR)-RISs: Are They Applicable to Dual-Sided Incidence?" *IEEE Wireless Communications Letters*, vol. 12, no. 1, pp. 129-133, Jan. 2023.

6. **J. Xu**, J. Zuo, J. T. Zhou and Y. Liu, "Active Simultaneously Transmitting and Reflecting (STAR)-RISs: Modelling and Analysis", *IEEE Wireless Communications Letters*, doi: 10.1109/LCOMM.2023.3289066, Feb. 2023.

7. **J. Xu**, X. Mu, and Y. Liu, "Exploiting STAR-RISs in Near-Field Communications", submitted to *IEEE Transactions on Wireless Communications* (under revision), Nov. 2022.

8. **J. Xu** and Y. Liu, "A Novel Channel Model for Reconfigurable Intelligent Surface-assisted Wireless Networks", *Proc. IEEE Global Communications Conf. (GLOBECOM'20)*, December 2020.

9. **J. Xu** and Y. Liu, "Reconfigurable Intelligent Surface-assisted Networks: Phase Alignment Categories", *Proc. IEEE Int. Communications Conf. (ICC'21)*, June 2021.

10. **J. Xu**, Y. Liu, and X. Mu, "Performance Analysis for the Coupled Phase-Shift STAR-RISs", *IEEE Wireless Communications and Networking Conference (WCNC'22)*, April 2022.

11. X. Mu, Y. Liu, **J. Xu**, L. Guo and J. Lin, "Joint Beamforming Optimization for Simultaneously Transmitting And Reflecting (STAR) RIS Aided Communications : (Invited Paper)," *55th Asilomar Conference on Signals, Systems, and Computers*; pp. 709-714, 2021.

12. Z. Wang, X. Mu, **J. Xu**, and Y. Liu, "Simultaneously Transmitting and Reflecting Surface (STARS) for Terahertz Communications", submitted to *IEEE Journals, arXiv:2212.00497* (under revision), Dec. 2022.

13. Z. Xie, Y. Liu, **J. Xu**, X. Wu, and A. Nallanathan, "Performance Analysis for Near-Field MIMO: Discrete and Continuous Aperture Antennas", submitted to *IEEE Journals*, Apr. 2023.

14. Y. Liu, X. Liu, X. Mu, T. Hou, **J. Xu**, M. Di Renzo, and N. Al-Dhahir, "Reconfigurable Intelligent Surfaces: Principles and Opportunities", *IEEE Communications Surveys and Tutorials*; vol. 23, no. 3, pp. 1546-1577, thirdquarter 2021.

15. Y. Liu, X. Mu, **J. Xu**, R. Schober, Y. Hao, H.V. Poor and L. Hanzo, "STAR: Simultaneous Transmission And Reflection for 360° Coverage by Intelligent Surfaces", *IEEE Wireless Communications*; vol. 28, no. 6, pp. 102-109, December 2021.

16. X. Liu, Y. Xu, P. Liu, T. Yang, **J. Xu**, L. Wang, G. Xie, X. Li, S .Uhlig, "SEAD Counter: Self-Adaptive Counters With Different Counting Ranges", *IEEE/ACM Transactions on Networking*; vol. 30, no. 1, pp. 90-106, Feb. 2022.

Chapter 2

Background Information and Fundamental Principles

In this chapter, we present crucial background information and fundamental principles that form the basis of this thesis. The following four topics are specifically addressed: electromagnetics (EM) basics, fundamentals of RIS, channel modeling methods, and principles of power-domain NOMA.

2.1 Electromagnetics Basics

At the heart of studying the reflection and refraction of intelligent surfaces lies the investigation of the interaction between electromagnetic waves and dielectric materials. This interaction is governed by the physics principle known as Maxwell's equations. From these equations, two fundamental laws of physics can be derived: the boundary conditions for EM fields and the equivalence principle. These laws serve as the theoretical foundations for all the channel models discussed in this thesis. In the following section, we provide a concise introduction to these two EM principles.

2.1.1 Boundary Conditions for EM Fields

Boundary conditions for EM fields encompass specific rules that dictate the behavior of electric and magnetic fields at interfaces or boundaries between different materials or regions. Within the context of STAR-RIS, particular emphasis is placed on the boundary conditions of a current layer. This is because when a wireless signal impinges upon a STAR-RIS, it induces electric and magnetic currents within the surface, effectively transforming the STAR-RIS into a current layer.

Let $\mathbf{J}_s$ denote the electric current density. Since the electric field component of the impinging EM field is oscillating, $\mathbf{J}_s$ also oscillates and thus produces EM radiation with electric field $\mathbf{E}^J$, and magnetic fields $\mathbf{H}_1^J$ and $\mathbf{H}_2^J$ on the two sides of the STAR-RIS, respectively. The magnetic current density, $\mathbf{K}_s$, is generated by vortex (circular) currents within the layer [10]. These currents are induced by the oscillating magnetic component of the EM field and they produce EM radiation with electric fields $\mathbf{E}_1^K$ and $\mathbf{E}_2^K$, and magnetic field $\mathbf{H}^K$. The strengths of these two types of currents are assumed to be proportional to the sum of the incident and radiated fields at the surface.

Finally, the boundary conditions for EM field at the considered current layer are given as follows [11]:

$$\mathbf{n} \times (\mathbf{H}_1^J - \mathbf{H}_2^J) = \mathbf{J}_s \text{ and } \mathbf{n} \times (\mathbf{E}_1^K - \mathbf{E}_2^K) = \mathbf{K}_s, \tag{2.1}$$

where $\mathbf{n}$ is the unit vector perpendicular to the STAR-RIS. By considering these boundary conditions at a current layer, we can analyze and model the behavior of EM fields and the interaction of EM waves with the RIS or any other current-carrying surface. These conditions play a significant role in understanding the performance and design of RIS-based systems and their impact on wireless communication and electromagnetic wave propagation.

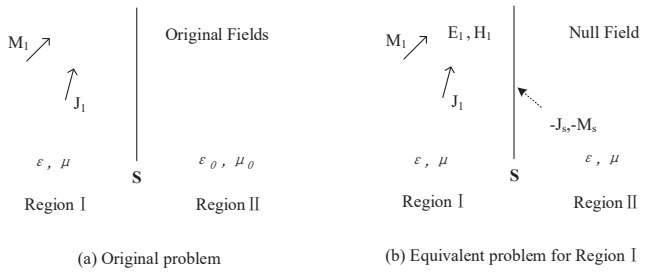

Figure 2.1: Love's equivalence internal problem (for region I).

2.1.2 Equivalence Principle

A wireless signal is essentially an EM wave propagating in a three-dimensional space. Attenuation or reduction of the signal strength occurs as the EM wave propagates through the space and interacts with the scattering objects. From basic principles of electromagnetism, the signal power per unit area is proportional to the square of the electric field of the corresponding wave in a given media. As far as reflective and refractive smart surfaces are concerned, this requires the need of understanding how the EM waves interact with the surrounding objects. The equivalence principle, especially the surface equivalence principle (SEP), is the building block for studying the EM wave transformations. Some authors also call it Love's field equivalence principle. The principle can be adopted for both external problems (source-free region) and internal problems. The SEP states that the EM field outside or inside a close surface can be uniquely determined by the electric and magnetic currents on the surface. As shown in Fig. 2.1, the equivalent problem for the region I can be reformulated by placing equivalent currents on S that satisfy the boundary condition for each particular case and filling the region II with the same medium of constitutive parameters ϵ and μ. Thus, the equivalent currents ($-J_s$,$-M_s$), together with the original source currents (J_1,M_1), radiate the correct fields in region I. The equivalent problem for region II can be formulated similarly.

Love's field equivalence principle is the theoretical foundation for analyzing the radiation pattern of RISs. However, the SEP does not specify how to calculate the EM field produced by the surface currents. To obtain the signal strength at an arbitrary field

point, the Huygens-Fresnel principle can be employed. The Huygens-Fresnel principle is a method of analysis applied to problems of wave propagation, which states that every point on a wavefront is itself the source of spherical wavelets, and the secondary wavelets emanating from different points mutually interfere. The sum of these spherical wavelets forms the wavefront. Based on the Huygens-Fresnel principle, the EM field scattered by an RIS (in reflection and transmission) can be quantified analytically.

In summary, the SEP provide a valuable framework for modeling RIS in wireless communication systems. By representing the RIS as an equivalent surface with appropriate electric and magnetic surface currents, their electromagnetic interactions can be effectively studied and integrated into electromagnetic models for performance analysis and optimization.

2.2 RIS Fundamentals

An RIS is a two-dimensional (2D) material structure with programmable macroscopic physical characteristics. In this section, we first introduce the different device implementations of RISs. Next, we discuss how RIS elements can be made tunable by using varactor diode. Finally, we introduce the fundamental principles which govern the operation of RISs, namely, the generalized laws of refraction and reflection and the cophase condition.

2.2.1 Different Device Implementations of RISs

There are various tunable surface designs which are potential candidates for realizing RISs. In [5], the authors pointed out an intuitive difference between natural and artificial materials (RISs in general), namely that natural materials exhibit uniform EM properties along their tangential directions, while artificial materials exhibit either a periodic or quasi-periodic nature. In terms of the periodic structure, we can loosely classify RISs into two categories, namely the patch-array based solutions and the metasurface based solutions. The patch-array based RISs consist of periodic cells having sizes

on the order of a few centimetres. Because of their relatively large sizes, each cell (patch) can be made tunable by incorporating either PIN diodes or delay lines. By contrast, the matasurface based RISs have periodic cells on the order of a few millimetres, possibly micrometres, or even molecular sizes. Hence they require more sophisticated controls of their EM properties, such as the conductivity and permittivity. Below, we provide a brief overview of patch-array based and metasurface based RISs. All these mentioned device characteristics have had successful prototypes built or rely on strong theoretical evidence in support of their feasibility. In the following, we discuss these device implementations for RISs.

For patch-array-based RISs, elements accommodate positive-intrinsic-negative (PIN) diodes or varactor diodes to configure phase-shift states. The power consumption is composed of two parts, namely the static power consumption of the control circuit and the dynamic power consumption of each element. Depending on the size of the RIS, the power consumption of the control circuit range from 0.72 watts (W) to 10 W [12]. For the case where PIN diodes are used to control the phase-shift states of each elements, they typically consume 0.33 mW per diode in "on" state [12].

In [13], the authors presented a prototype relying on the PIN diode empowered implementation. This implementation is the most popular design for both RISs and STAR-RISs since PIN diodes are of low-cost and are voltage-controlled. The drawback of this implementation is that since PIN diodes only have two states, namely, "ON" or "OFF", this implementation can only support a finite-cardinality reflection and transmission coefficient set. In [14], the authors showed the antenna-empowered RIS cell consists of two antenna elements, which are connected by a tunable delay line. However, the drawback of this implementation is that the delay line may impose a considerable energy loss. A popular prototype of the metasurface based RISs is the *transparent dynamic metasurface* designed by researchers at NTT DOCOMO, Japan. According to [9], the metasurface supports the manipulation of 28 GHz (5G) radio signals. It allows dynamic control of both of the signal's reflection and transmission while maintaining transparency

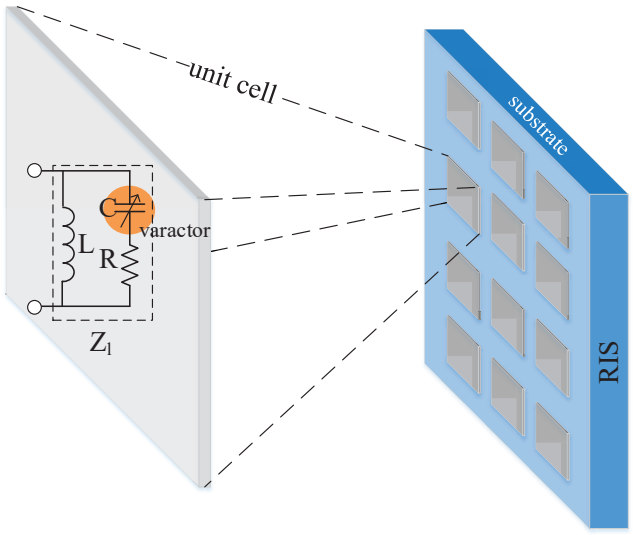

Figure 2.2: Schematic diagram of the varactor RIS.

of the window. However, its drawback is that it does not have the ability to dynamically reconfigure itself as the PIN diode empowered implementations. Moreover, adjusting the distance between substrates may affect the reflection coefficient of the entire surface instead of only reconfiguring a particular element. Lastly, there are already experimental graphene-based RF devices [15]. To achieve reconfigurability, a single layer of graphene has tunable reflection and transmission coefficients by adjusting its conductivity. Recent advancements in device engineering and material science have led to the development of more efficient and low-power graphene-based devices. The precise power consumption and voltage values needed to control the transmission properties of a graphene layer can vary depending on factors such as the device structure and doping levels.

2.2.2 Achieving Tunability

The EM characteristics of an RIS, such as the phase discontinuity, can be reconfigured by tuning the surface impedance, through various mechanisms. Apart from electrical voltage, other mechanisms can be applied, including thermal excitation, optical pump, and physical stretching. Among them, electrical control is the most convenient choice, since the electrical voltage is easier to be quantized and controlled by FPGA chips. The

choice of RIS materials include semiconductors [16] and graphene [17].

Regardless of the tuning mechanisms, we focus our attention on patch-array smart surfaces in the following text. The general geometry layout of this type of RIS can be modeled as a periodic (or quasi-periodic in the most general case) collection of unit cells integrated on a substrate. For ease of description, in addition, we limit our discussion to RISs that are based on a local design, in which the cells do not interact with each other (which is referred to as a non-local design). A local design usually results in the design of sub-optimal RISs. A comprehensive discussion about local and non-local designs can be found in [5]. When designing RIS-assisted communication systems based on a local design, the most important RIS parameter is the reflection coefficient of R at each element (unit cell or scatter). To characterize the tunability of the RIS, the method of equivalent lumped-element circuits can be adopted. As shown in Fig. 2.2, the unit cell is equivalent to a lumped-element circuit with a load impedance Z_l. Particularly, the equivalent load impedance can be tuned by changing the bias voltage of the varactor diode. When modeling patch-array RISs in wireless communication systems, we can characterize, under a local design, each of its unit cells through an equivalent reflection coefficient. For example, the reflection coefficient of the m-th cell can be modeled as:

$$R_m = \beta_m \cdot e^{j\phi_m} \tag{2.2}$$

where β_m and ϕ_m correspond to the amplitude response and the phase response, respectively. The equivalent reflection coefficient depends on the tuning impedance of the lumped circuit that controls each unit cell, as well as the self and mutual impedances (if mutual coupling cannot be ignored) at the ports of the RIS. In particular, as shown in [18], β_m and ϕ_m in (2.2) are usually not independent of each other, i.e., $\beta_m = f(\phi_m)$. In the following sections, $\Phi(\vec{r_x})$ refers to the phase discontinuity introduced by the RIS as a function of the position on the RIS, and ϕ_{mn} refers to the phase discontinuity of the (m, n)-th element of a patch-array RIS.

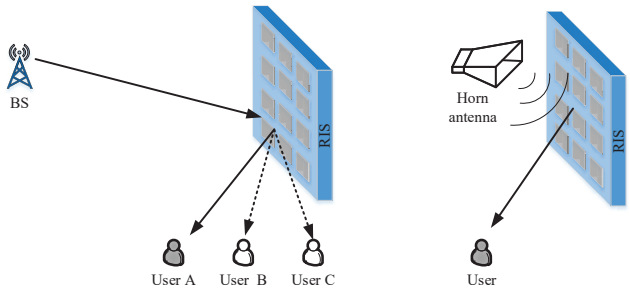

(a). Beam steering (b). Beam focusing

Figure 2.3: Typical functions of reflecting surfaces.

2.2.3 RIS Operating Principles

Among the many operating functions and configurations of RISs, *anomalous reflection* and *beamforming* are widely used in the context of wireless communications. Adopting the wave-optics perspective, anomalous reflection is a wavefront transformation from a plane wave to another plane wave, while beaforming is a wavefront transformation from a plane wave to a desired wavefront. Adopting the ray-optics perspective, we present the operating principles of these two configurations in the following text. As far as anomalous reflection is concerned, the RIS is designed to reflect an incident beam to a far-field terminal, following the generalized laws of reflection [19]. As far as beamforming (also called focusing) is concerned, the incident wave is focused towards a targeted region, often referred to as the *focal point*. The required RIS configuration follows the co-phase condition [20]. The relation between these two operating principles is discussed in detail in [21]. Before presenting these two different principles, the physical distinction between the near-field region and the far-field region needs to be clarified.

In the following text, adopting the ray-optics perspective, we discuss the generalized laws of refraction and reflection, as well as the corresponding co-phase condition.

2.2.3.1 The Generalized Laws of Refraction and Reflection

From a geometrical optics perspective, anomalous reflection and refraction from an RIS can be described by using the generalized laws of refraction and reflection [19], which is

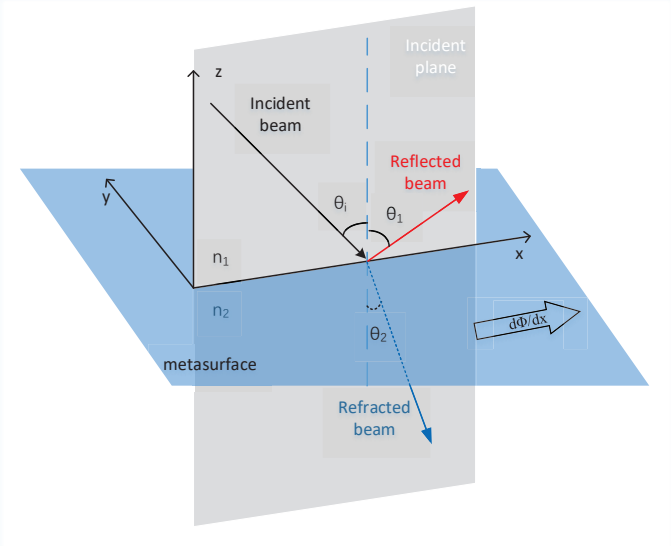

Figure 2.4: Illustration of the generalized laws of refraction and reflection.

a natural derivation of both Fermat's principle and the boundary conditions governed by Maxwell's equations.

Principle 1. *Achieving anomalous reflection (beam-steering) (Fig. 2.3(a))*

Suppose that the phase discontinuity at the boundary is a function of the position along the x direction $\Phi(\vec{r_x})$, where $\vec{r_x}$ is the position vector on the boundary. Moreover, suppose that the derivative of the phase discontinuity exists. Then, the angle of reflection (θ_1) and the angle of refraction (θ_2) are [22]:

$$\theta_1 = \sin^{-1}\left[\sin\theta_i + \frac{\lambda}{2\pi n_1}\frac{\mathrm{d}\Phi}{\mathrm{d}x}\right], \tag{2.3}$$

$$\theta_2 = \sin^{-1}\left[\frac{n_1}{n_2}\sin\theta_i + \frac{\lambda}{2\pi n_2}\frac{\mathrm{d}\Phi}{\mathrm{d}x}\right], \tag{2.4}$$

where θ_i is the angle of incidence, λ is the wavelength of the transmitted signal in vacuum, and n_1, n_2 are the refractive indexes, as shown in Fig. 2.4. □

There are other results related to the generalized laws of refraction and reflection, including the critical angles for total internal reflection or refraction. The main result

just presented here states that, when a phase discontinuity is introduced at the boundary surface, the angles of reflection and refraction depend not only on the angle of incidence but also on the wavelength, refractive indexes, and the gradient of the phase discontinuity. This gives extra controllable parameters to manipulate the reflected and refracted EM waves. As a result, anomalous reflection can be achieved by tuning the phase gradient ($\mathrm{d}\Phi/\mathrm{d}x$) based on (2.3) or, in the discrete patch-array RISs, by tuning the length of the super-lattice. However, the assumption that the derivative of the phase discontinuity is constant ($\mathrm{d}\Phi/\mathrm{d}x = \text{const.}$) does not necessary hold if different wave transformations are needed.

2.2.3.2 Cophase condition

Focusing is usually implemented when the RIS is within the near-field of the source or the terminal is close to the RIS. In these cases, the curvatures of the incident and reflected wavefront are non-negligible. The optimization of the surface aims to produce a pencil-beam pointing towards the direction of the terminal. When the link between the source and the RIS, as well as the link between the RIS and the terminal are in LoS, the following cophase condition [20] can be applied.

Principle 2. *Achieving beamforming (focusing) (Fig. 2.3(b))*

Let r_{mn} denote the position of the (m,n)-th RIS element, r_s denote the position of the source, $\hat{u}$ denote the direction of the observer with respect to the surface. As shown in Fig. 2.5, ϕ_{mn} can be chosen as follows:

$$-k_0(|\vec{r}_{mn} - \vec{r}_s| - \vec{r}_{mn} \cdot \hat{u}) + \phi_{mn} = 2\pi \cdot t, \tag{2.5}$$

where $t = 1, 2, 3...$ and $k_0 = 2\pi/\lambda_c$. □

In conclusion, this section has provided a brief overview of the fundamentals of RIS in the context of wireless communication. We have explored the key concepts and prin-

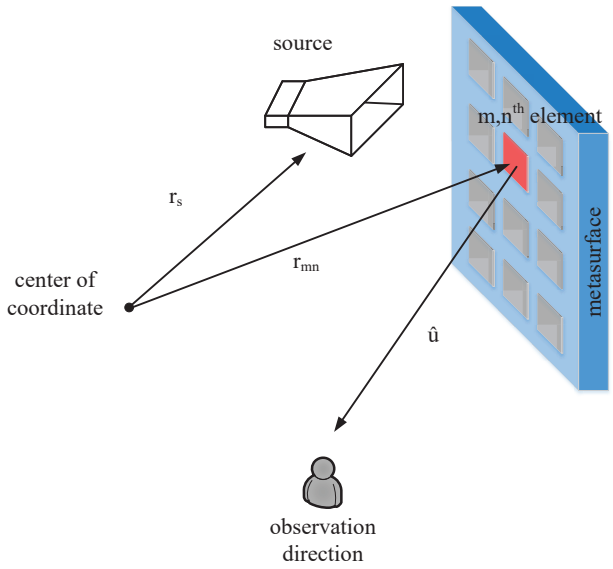

Figure 2.5: Coordinate representation of cophase condition.

ciples that underpin the functionality and operation of RISs. By understanding the underlying principles of electromagnetic wave propagation, reflection, and transmission, we have gained insight into how RIS can manipulate and control these waves to achieve various objectives such as beamforming, beam-steering, and signal enhancement. The fundamentals covered in this section provide a solid foundation for further investigation into the modeling of STAR-RISs.

2.3 Channel Modeling Methods

Various channel modeling methods are employed to capture the characteristics of wireless communication channels, facilitating the design and analysis of wireless systems. Two common approaches are deterministic channel modeling and statistical channel modeling. Deterministic channel modeling focuses on accurately representing the wireless channel by considering the geometric properties of the environment, such as transmitter and receiver locations, as well as obstacles. It utilizes techniques like ray tracing or electromagnetic wave propagation theories to simulate the channel response in detail. On the other hand, statistical models describe the statistical properties of the wireless chan-

nel based on empirical measurements. These models capture average behavior, fading effects, and time-varying characteristics of the channel. They provide a more generalized representation of the channel and are often used when precise geometric information is not available or necessary.

Channel models can also be classified based on the physical principles used to calculate path loss. Ray-tracing-based models rely on geometric properties and are primarily accurate in the far-field region, while EM-wave-propagation-theory-based models provide greater accuracy and reliability within the near-field region.

In the following of this section, we provide a brief overview of the far-field and near-field regions, followed by a discussion of different channel modeling methods and their respective advantages and disadvantages. This exploration will shed light on the appropriateness of each method for different scenarios, enabling a better understanding of their applications in wireless communication systems.

2.3.1 Near-Field v.s. Far-Field

In the spirit of dimensional analysis, the characteristics of a system can be represented by dimensionless numbers. In order to separate the near-field region from the far-field region, a proper dimensionless number is needed. Let L and R_F denote the antenna aperture size of the RIS and the focal distance, respectively. Assume that z is the distance of a particular field point to the RIS. Theoretically, the far-field and near-field regimes can be differentiated as follows: The distance of $2L^2/\lambda$ is a commonly used criterion to decided the boundary between the near-field and far-field regions. The position corresponding to $z = 2L^2/\lambda$ is the boundary between the near-field region and the far-field region. This result comes from the inspection of the power density variation with the distance between a field point and the RIS. Within the near field where $z < 2L^2/\lambda$, the power density shows significant variations. The peak position of the power density in the near-field region, namely R_F, changes with different RIS configurations. Using proper co-phase conditions, beam focusing can be achieved within

the near-field of the RIS. It is worth mentioning that, in general, the boundary between the near-field and far-field regimes depends on the specific configuration of the RIS, as it was recently remarked in [21].

In general, the essential difference between the near-field region and the far-field region is how the power density changes with distance. Consider, for example, that the RIS focuses the wave within an area a. The total energy incident on the RIS is proportional to the solid angle (Ω) spanned by the surface area of the RIS with respect to the location of the transmitter. After the reflection, the transmitted energy is spread over the area a. Thus, the power density around the focal point is proportional to Ω/a. Moreover, according to [23], the area a is proportional to $\lambda^2(1 + 4z^2/L^2)$, as a result of the Abbe diffraction limit. In the far-field region, the second term inside the brackets dominates and Ω/a is proportional to $L^2\Omega/z^2$, which is the typical spherical dissipation of the signal power with the distance. In the near-field region, the first term dominates and the area a becomes very small. As a result, a high focusing gain can be achieved.

2.3.2 Far-Field Channel Models

One of the most widely-accepted far-field channel models is the ray-tracing based one [24]. The ray-tracing technique has long been adopted as an efficient way to simplify the calculation of wave propagation and obtain the channel gains of receivers located within the far-field region. In addition, the conventional ray-tracing technique is compatible with the phase-shift device modeling of RISs. However, the ray-tracing technique assumes a finite number of scatterers and studies their sum, hence it cannot deal with continuous phase profiles. In the context of analyzing RISs, the ray-tracing technique relies on the following assumptions:

1. Each element is treated as a distinct scatterers having a known location and dielectric properties.

2. The wave impinging on the RIS is regarded as a collection of rays, each falling on a single element. Thus, the received bundle of rays is constituted by a discrete 2-D

array instead of a EM field in 3-D space.

3. The interactions between each ray and each element, including the reflection and transmission, are studied using geometrical optics instead of wave optics.

The simplicity of the ray-tracing far-field model is one of its key advantages. However, it may not be suitable for accurately modeling the near-field region. In the subsequent sections, we explore alternative models that are specifically designed to capture the characteristics of the near-field channel.

2.3.3 Near-Field Channel Models

2.3.3.1 Huygens-Fresnel Principle Based Channel Models

The Huygens-Fresnel principle is a powerful method of solving the problems of wave propagation in both the far-field and near-field regions. It states that every point on a wavefront is itself the source of spherical wavelets, and the sum of these spherical wavelets forms the wavefront. The 2-D wavefront should preferably be located in the same plane as the RIS and the contribution to the received field at each wave point is proportional to several factors. These include the receiving aperture size on the wavefront, the amplitude of the corresponding wavelet, the leaning factor at each point on the wavefront, and to the reciprocal of the distance between each point on the wavefront and the receiver.

2.3.3.2 Green's Function Method Based Channel Models

The Green's function method is a mathematical procedure of solving inhomogeneous linear differential equations. According to Maxwell's equations, the electromagnetic field surrounding a RIS satisfies the inhomogeneous Helmholtz equation. The Helmholtz equation represents the wave function, that links the spatial derivative and the time derivative of the field with the source. Additionally, for fully characterizing the field, a boundary condition [21] is needed. Depending on the type receiver analyzed, the closed surface boundary should enclose the space, where the target receiver is located. This closed surface is formed by an infinitely large plane at the smart surface and a hemisphere

having a radius tending to infinity. The boundary condition can be expressed as the complex value of the EM field at the surface, which is known as the Dirichlet boundary condition, or as the derivative of the EM field along the direction perpendicular to the surface, which is known as the Neumann boundary condition. The critical challenge of the Green's function based channel model is to choose the appropriate boundary conditions. This is because in Green's function method, all phase-shifts the RIS impose on wireless signals are characterize through the boundary conditions. In light of this, the Green's function based channel models require detailed characterization of the smart surface.

In Chapter 5, we study the near-field performance of metasurface-based STAR-RIS using Green's function method based channel models. The detailed formulation of the Green's function will be given in Section. 5.2.

2.3.3.3 Angular Spectrum Based Channel Models

This method also relies on the Huygens-Fresnel principle. However, instead of calculating the channel gain using the Fresnel-Kirchhoff diffraction formula, the model exploits the fact that the EM fields radiated by a RIS having any arbitrary distributions can be regarded as a collection of plane waves traveling in different directions. In light of this, provided that the spectrum of this collection of plane waves can be determined, the channel gain can also be derived at any point. In angular spectrum based channel models, the wavefront is chosen as the plane in which the RIS lies. In the field of antenna design, the 2-D spatial distribution of the EM field at this chosen wavefront is referred to as the *aperture distribution* [25], characterizing the complex-valued amplitude as a function of position on the smart surface. An essential statement that enables the use of angular spectrum based channel models is the fact that the plane-wave angular spectrum of an arbitrary wave form can be given by the Fourier transform of the aperture distribution [26]. In general, an arbitrary aperture distribution can be expressed as a Fourier expansion of a series of plane waves having different wave numbers. Correspond-

Table 2-A: Comparing different channel models for STAR-RISs.

Channel Models	Advantages	Disadvantages	Challenges
Ray-tracing	Simplistic in form and easy to calculate channel gain	Only applies under certain conditions in far-field regions	Describing the channel in the near-field regions
Huygens-Fresnel principle	Fundamental and applies to near-field regions	Applies only to free-space scenarios or LoS-dominated links	Choosing proper wave-front to characterize the STAR-RIS
Angular spectrum	Convenient for designing desired aperture distributions	Applies only to free-space scenarios or LoS-dominate links	Deciding the boundaries between different field regions
Green's function method	Fundamental and apply to general cases	Complex and requires detailed system specifications	Proper boundary conditions to characterize the environment

ingly, the radiation obeying this aperture distribution can be expressed as a spectrum of plane waves. More detailed inspection shows that not all the wave numbers in the Fourier expansion of the aperture distribution correspond to propagating waves. In fact, aperture distributions having large wave number values give rise to *evanescent waves*. These waves does not propagate well, because they decay exponentially with distance, hence they do not usefully contribute to the received power beyond a few wavelengths.

2.3.3.4 Summary

This section discusses different channel modeling methods used in wireless communication. Deterministic modeling accurately represents the channel based on geometric properties, while Statistical modeling captures average behavior. Far-field models, such as ray-tracing, calculate channel gains efficiently. Near-field models include Huygens-Fresnel principle-based, Green's function-based, and angular spectrum-based models. Understanding these methods helps analyze and design wireless systems considering accuracy and complexity.

2.4 Power-Domain NOMA

Power-domain NOMA is a technique in wireless communication where multiple users share the same time-frequency resources by allocating different power levels to their signals. Consider a downlink scenario with a base station transmitting signals to two users, user 1 and user 2. In power-domain NOMA, the transmitted signal can be expressed as:

$$x = \sqrt{p_1}s_1 + \sqrt{p_2}s_2, \tag{2.6}$$

where p_1 and p_2 represent the power levels allocated to user 1 and user 2, respectively. s_1 and s_2 are the symbols intended for user 1 and user 2, respectively. At the receiver side, the received signal for user 1 and user 2 can be represented as:

$$y_1 = h_1\sqrt{p_1}s_1 + h_1\sqrt{p_2}s_2 + n_1, \tag{2.7}$$

$$y_2 = h_2\sqrt{p_1}s_1 + h_2\sqrt{p_2}s_2 + n_2, \tag{2.8}$$

where h_1 and h_2 denote the channel coefficients for User 1 and User 2, respectively. n_1 and n_2 represent the additive white Gaussian noise (AWGN) for user 1 and user 2, respectively.

To decode the signals at the receiver, successive interference cancellation (SIC) is applied. User 1, being the strong user, is decoded first. The received signal is processed as:

$$\hat{s}_1 = \frac{y_1 - h_2\sqrt{p_1}s_1}{h_1\sqrt{p_1}}, \tag{2.9}$$

where $\hat{s}_1$ is the estimated symbol for User 1. After decoding signal for user 1, the interference caused by user 1 can be subtracted from the received signal of user 2:

$$\hat{y}_2 = y_2 - h_1\sqrt{p_2}\hat{s}_1. \tag{2.10}$$

Finally, user 2's signal can be decoded using the modified received signal:

$$\hat{s}_2 = \frac{\hat{y}_2}{h_2\sqrt{p_2}}. \tag{2.11}$$

By utilizing power-domain NOMA and performing successive interference cancellation, both users can decode their messages successfully. NOMA offers advantages over OMA in terms of spectral efficiency, user fairness, increased connectivity, enhanced coverage and reliability, and future compatibility. It allows for more efficient spectrum utilization, better fairness among users, accommodates a larger number of users, improves coverage and reliability, and is compatible with future communication systems. How-

ever, one challenge of NOMA is the increased complexity in receiver design and signal decoding due to the overlapping nature of the transmitted signals. Additionally, NOMA may face interference issues between users, requiring effective interference management techniques to mitigate their impact.

2.5 State-of-the-Art Advancements in RIS Research

In the following, we briefly summarize the recent advancements in RIS and highlight the motivations behind the technical sections of this thesis.

2.5.1 Recent Advancements in RIS

Early in 2018, Liaskos *et al.* demonstrated the potential of the concept of HyperSurfaces [27]. In [28], Huang *et al.* further introduced the concept of holographic multiple-input and multiple-output (MIMO) surfaces, which is envisioned as a key technology for the physical layer of future 6G wireless networks. In 2019, the authors of [29] demonstrated the benefits of RISs for wireless communications and separated the concept of RIS from other fields of study including meta-materials and optics. In [29], the basic device model of RISs was given, where each element was characterized by a phase-shift value.

The pioneering works on the path loss model of the RIS channel are as follows: In [12], three path loss formulas were proposed for far-field beamforming case, near-field beamforming case, and near-field broadcasting case. For the near-field broadcasting case, the path loss is proportional to $(d_1+d_2)^2$, where d_1 and d_2 denotes the distance from the transmitter to the RIS and from the RIS to the receiver, respectively. For other cases, the path loss is proportional to $(d_1 d_2)^2$. In [30], Özdogan *et al.* further disproved the $(d_1 + d_2)^2$ formula for the far-field case and present the path loss model at an arbitrary observation angle.

At the same time, representative works on the multipath fading (small-scale fad-

ing) characterize each half-channel from the transmitter to the n-th element on the RIS and from the n-th element to the receiver by well-known distribution, such as Rayleigh fading [31] and Rician fading [32]. The overall multipath fading channel was the multiplication of the above two types of links and the phase shift matrix. In [33] and [34], Badiu *et al.* and Qian *et al.* considered the fading channel with the presence of phase errors and its influence on the signal-to-noise ratio.

Finally, research contributions of applying OMA and non-orthogonal multiple access (NOMA) in RIS-assisted networks includes [35–38]. In [35], Ding *et al.* proposed an RIS-assisted NOMA transmission architecture where the RIS only serves cell-edge users. In [36], Fu *et al.* investigated the joint beamforming design of the downlink multiple-input single-output (MISO) RIS-assisted NOMA networks. In [37], Mu *et al.* optimized the sum rate of MISO RIS-NOMA networks. In [38], Hou *et al.* compared the performance of power-domain NOMA and OMA in RIS-assisted networks under the best-case and worst-case of new channel statistics.

2.5.2 Knowledge Gaps and Motivations

Although numerous works have been published that demonstrated the benefit of RISs, at the time when I started my Ph.D. research, there was a huge knowledge gap between the physical/hardware and communication aspects of RISs. In addition, the function of RISs was mostly limited to passive reflection. To elaborate, I found knowledge gaps in the following aspects of RIS research:

1. Existing research contributions on RISs [8, 39–43] mainly considered the use of the reflecting-only RISs, which brings extra topological constraints to the wireless system. Specifically, to receive signals from the reflecting-only RISs, users have to be on the same side as the transmitter. In addition, existing research contributions [44–46] mainly focused on studying particular physical properties of the designed surface. There is a lack of communication models for the RISs that are both physically-compliant and mathematically-tractable.

2. From existing research, it is not yet clear how wireless signals can be manipulated when the signals incident on both sides of the RIS simultaneously. This is practically relevant to the uplink communication scenario, where multiple users surrounding the RIS have to upload their information to the base station (BS). In addition, RISs suffer from the "double-fading" effect where the small-scale fading of the base station (BS)-RIS link and the RIS-receiver link are multiplied [39]. As a result, a huge number of passive elements is required to achieve any practical performance gain. At the same time, the large surface area of STAR-RISs imposes challenges in terms of its deployment and maintenance.

3. While various research contribution focused on patch-array-based RISs, the modeling and analysis of metasurface-based RISs are still in their infancy. Particularly, as the aperture size of RIS is envisioned to become extremely large, their near-field effects will become dominant. The near-field regime exhibits distinctive features that diverge from those observed in the far-field region, thereby necessitating the development of novel channel modeling techniques.

In the following chapters, this thesis leverages knowledge in Electromagnetics, antenna theory, and information theory to bridge these knowledge gaps. In Chapter 3-5, the aforementioned knowledge gaps are addressed, respectively.

Chapter 3

Independent and Correlated T&R Phase-Shift Models and Practical Phase-Shift Configuration Strategies

This chapter is organized as follows. The main contributions of this work is first introduced in Section 3.1. Then the proposed independent and correlated transmission and reflection (T&R) phase-shift model is given in Section 3.2 and 3.3. Three practical phase-shift configuration (PSC) strategies are further introduced in Section 3.5. Section 3.6 delves into the exploration of relaxing the T&R phase-shift correlation by incorporating lossy STAR elements. Additionally, Section 3.7 introduces the commonly used performance metrics and gives the mathematical definitions for outage probability and diversity order. Section 3.8 presents the performance analysis of the proposed PSC strategies in terms of their power scaling laws and diversity orders. Finally, Section 3.9 shows the numerical results which verifies the obtained analytical results. Section 3.10 concludes this chapter.

3.1 Motivation and Contributions

To investigate the performance of STAR-RIS-aided wireless network, a accurate signal model is required. However, existing research contributions [44–46] mainly focused on reflecting-only RISs or studying particular physical properties of STAR-RISs. There is a lack of communication models for the STAR-RISs that are both physically-compliant and mathematically-tractable. To facilitate the research on STAR-RISs in the field of wireless communications, we first present a independent T&R phase-shift model and two channel models for the near-field region and the far-field region. Still, for passive lossless STAR-RISs, independent T&R phase-shift is difficult to achieve without additional power source. To reveal practical insights into the design and performance analysis of STAR-RISs, a *correlated* T&R phase-shift model is proposed for passive lossless STAR-RISs. Based on the correlated T&R phase-shift model, a STAR-RIS-aided two-user downlink communication system is investigated for both OMA and NOMA. To evaluate the impact of the correlated T&R phase-shift model on the communication performance, three phase-shift configuration strategies are developed, namely the primary-secondary phase-shift configuration (PS-PSC), the diversity preserving phase-shift configuration (DP-PSC), and the T/R-group phase-shift configuration (TR-PSC) strategies. Furthermore, we derive the outage probabilities for the three proposed phase-shift configuration strategies as well as for those of the random phase-shift configuration and the independent phase-shift model, which constitute performance lower and upper bounds, respectively. Then, the diversity order of each strategy is investigated based on the obtained analytical results. It is shown that the proposed DP-PSC strategy achieves full diversity order simultaneously for users located on both sides of the STAR-RIS. Moreover, power scaling laws are derived for the three proposed strategies and for the random phase-shift configuration. Numerical simulations reveal a performance gain if the users on both sides of the STAR-RIS are served by NOMA instead of OMA. Moreover, it is shown that the proposed DP-PSC strategy yields the same diversity order as achieved by STAR-RISs under the independent phase-shift model and a comparable power scaling law with only

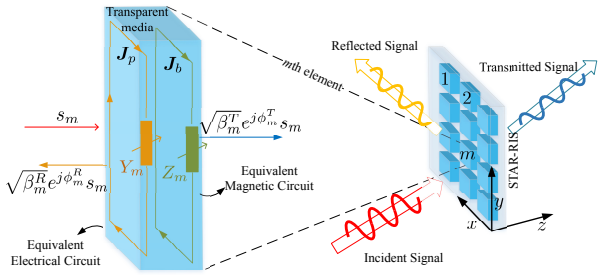

Figure 3.1: Schematic illustration of the STAR-RIS.

4 dB reduction in received power.

3.2 Independent STAR-RIS Phase-Shift Model and Channel Models

As shown in Fig. 3.1, a schematic representation of the structure of STAR-RISs is presented. Based on the field equivalence principle [39], as the STAR-RIS elements are excited by the incident signal, the transmitted and reflected signals can be equivalently treated as waves radiated from the time-varying surface equivalent electric currents $\mathbf{J}_s$ and magnetic currents $\mathbf{K}_s$ (also referred to as the bound currents). Within each element, the strengths and distribution of these surface equivalent currents are determined by the incident narrowband signal s_m as well as the local surface averaged electric and magnetic impedances Z_{e} and Z_{m}. Assume that the STAR-RIS produces both transmitted and reflected signals with the same polarization. At the mth element, these signals can be expressed as:

$$s_m^T = T_m s_m, \;\; s_m^R = R_m s_m, \tag{3.1}$$

where T_m and R_m are the transmission and reflection coefficients of the mth element, respectively. According to the law of energy conservation, for passive STAR-RIS elements, the following constraint on the local transmission and reflection coefficients must be satisfied:

$$|T_m|^2 + |R_m|^2 \leq 1. \tag{3.2}$$

According to electromagnetic theory, the phase delays of both the transmitted and reflected field are related to Z_{e} and Z_{m}. In Fig. 3.1, the reconfigurability of the element is reflected in the change of the surface impedances, since the transmission and reflection coefficients of the mth element is related to the surface impedances as: $T_m = \frac{2-\eta_0(Z_{\mathrm{e}})_m}{2+\eta_0(Z_{\mathrm{e}})_m} - R_m$, and $R_m = -\frac{2(\eta_0^2(Z_{\mathrm{e}})_m-(Z_{\mathrm{m}})_m)}{(2+\eta_0(Z_{\mathrm{e}})_m)(2\eta_0+(Z_{\mathrm{m}})_m)}$, where η_0 is the impedance of free space [47]. From the perspective of metasurface design, supporting the magnetic currents is the key to achieve independent control of both the transmitted and reflected signals. According to [48], single-layered RISs with non-magnetic elements can only produce identical radiation on different sides, which is referred to as the symmetry limitation. By introducing the equivalent surface electric and magnetic currents into the model, the proposed hardware model is able to independently characterize the transmission and reflection of each element. To facilitate the design of the STAR-RISs in wireless communication systems, we rewrite these narrowband frequency-flat coefficients in the form of their amplitudes and phase shifts as follows:

$$T_m = \sqrt{\beta_m^T} e^{j\phi_m^T},\ R_m = \sqrt{\beta_m^R} e^{j\phi_m^R}, \tag{3.3}$$

where $\beta_m^T, \beta_m^R \in [0,1]$ are real-valued coefficients satisfying $\beta_m^T + \beta_m^R \leq 1$, and $\phi_m^T, \phi_m^R \in [0, 2\pi)$ are the phase shifts introduced by element m for the transmitted and reflected signals, $\forall m \in \{1, 2, \cdots, M\}$. Note that different from the amplitudes (β_m^T and β_m^R) which are coupled due to the law of energy conservation, the phase shifts (i,e, ϕ_m^T and ϕ_m^R) can be independently adjusted.

3.2.1 Channel Models

Based on the proposed hardware model, in this section, we study the communication channels of the STAR-RISs. As shown in Fig. 3.2, a narrowband STAR-RIS-assisted wireless network is considered, where the transmitter (Tx) and receivers (Rxs) are equipped with single antenna and the STAR-RIS consists of M reconfigurable elements. As an initial analysis to demonstrate the extended coverage of the STAR-RIS, we consider a

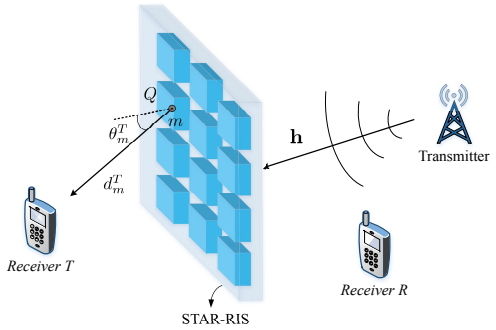

Figure 3.2: Illustration of the considered STAR-RIS-assisted network.

two-user setup. In particular, the Tx sends information to the two Rxs employing orthogonal frequency bands of equal sizes. Suppose that receiver T is located on the opposite side of Tx, with respect to the STAR-RIS, and thus, it can only receives the transmitted signals of the STAR-RIS. Receiver R and Tx are located on the same side of STAR-RIS. Let h^χ denote the direct link between Tx and receiver T or receiver R, where the notation $\chi \in \{T, R\}$ is an indicator representing "T" or "R". Let g^χ denote the effective channel between Tx and receiver χ through STAR-RIS transmission or reflection.

3.2.1.1 Far-field channel model

In this case, the Rxs are located in the far-field region of the STAR-RIS. We denote the channel between Tx and the STAR-RIS by $\mathbf{h} = (h_1, \cdots, h_M)^T$, where h_m is the channel between Tx and the mth element. In addition, let $\mathbf{r}^\chi = (r_1^\chi, \cdots, r_M^\chi)^T$ denote the channel between STAR-RIS and receiver χ. Since both Rxs are located in the far-field region of the STAR-RIS, the ray tracing technique can be adopted by studying a number of M geometrical rays, each corresponding to a multipath signal propagating through an element. This leads to the channel model as follows:

$$g^\chi = (\mathbf{r}^\chi)^H \text{diag}(\sqrt{\beta_1^\chi} e^{j\phi_1^\chi}, \cdots, \sqrt{\beta_M^\chi} e^{j\phi_M^\chi}) \mathbf{h}, \tag{3.4}$$

where $\mathbf{a}^H$ denotes the conjugate transpose of a complex vector $\mathbf{a}$. For convenience, we denote $\text{diag}(T_1, T_2, \cdots, T_M)$ by $\mathbf{\Phi}^T$ and $\text{diag}(R_1, R_2, \cdots, R_M)$ by $\mathbf{\Phi}^R$. In addition, in

the far-field channel model, $\mathbf{r}^{\chi}$ and $\mathbf{h}$ can be written in the form of path loss (large-scale fading) multiplied with the normalized small-scale fading channels. The large-scale fading depends on the distance between Tx, the STAR-RIS, and Rxs, while the small-scale fading depends on the scattering environment. Let d^{χ} denote the distances between the STAR-RIS and receiver χ, and d_0 denote the distance between Tx and the STAR-RIS. The channel gains can be expressed as:

$$|g^{\chi}| = \frac{1}{(d^{\chi})^{\alpha_{\chi}}(d_0)^{\alpha_0}} |(\widetilde{\mathbf{r}}^{\chi})^H \mathbf{\Phi}^{\chi} \widetilde{\mathbf{h}}|, \tag{3.5}$$

where $\widetilde{\mathbf{r}}^{\chi}$ and $\widetilde{\mathbf{h}}$ are the corresponding small-scale fading components. In addition, α_{χ} and α_0 are the path loss coefficients of the corresponding channels. Note that in Fig. 3.2, each RIS element behaves like a key-hole. The channel through a RIS element has the same structure as the keyhole MIMO channel, which was well-studied in [49]. As a result, the multiplicative channel formulated in (3.5) is consistent with the keyhole channel.

3.2.1.2 Near-field channel model

In scenarios where Rxs are located within the near-field region of the STAR-RIS, the conventional ray tracing technique based channel models can not be adopted. Based on the Huygens-Fresnel principle [39], A. Fresnel and Kirchhoff arrived at the analytical result which is known as the Fresnel-Kirchhoff diffraction formula. As illustrated in Fig. 3.2, the electromagnetic signal at Rx can be calculated by summing up the contribution of every elements on the wavefront. The wavefront is chosen as the plane where the STAR-RIS is located.

$$g^{\chi} = \frac{1}{j\lambda} \iint_{(\Sigma)} U^{\chi}(Q) F(\theta^{\chi}) \frac{e^{2j\pi d_m^{\chi}/\lambda}}{d^{\chi}} d\Sigma, \tag{3.6}$$

where j is the imaginary unit, (Σ) denotes a closed surface (wavefront) which contains the RIS elements and the scatterers in the environment, $U^{\chi}(Q)$ is the aperture distributions for the transmitted or reflected waves at point Q on (Σ), $F(\theta^{\chi})$ is the leaning factor at point Q, d^{χ} are the distances between Q and the receiver χ, and λ is the free-space

wavelength of the signal. The integral in (3.6) can be evaluated element by element. Assuming that the aperture distributions $U^{\chi}(Q)$ is uniform within each element, at the mth element, we have $U^{T}(Q) = \Phi_m^T h_m$ and $U^{R}(Q) = \Phi_m^R h_m$. Thus, (3.6) can be expressed as:

$$g^{\chi} = \frac{A_e}{j\lambda} \sum_m \Phi_m^{\chi} h_m F(\theta_m^{\chi}) \frac{e^{2j\pi d_m^{\chi}/\lambda}}{d_m^{\chi}}, \tag{3.7}$$

where A_e is the area of each element, and θ_m^{χ} is the direction of receiver χ, with respect to the normal direction of STAR-RIS, as illustrated in Fig. 3.2. According to the Fresnel-Kirchhoff diffraction formula, the leaning factor is $F(\theta_m^{\chi}) = (1 + \cos\theta_m^{\chi})/2$, which holds for both *receiver T* and *receiver R*. Thus, the channel gain can be expressed as:

$$|g^{\chi}| = \frac{A_e}{\lambda} \left| \sum_m \Phi_m^{\chi} h_m (1 + \cos\theta_m^{\chi}) \frac{e^{2j\pi d_m^{\chi}/\lambda}}{2d_m^{\chi}} \right|. \tag{3.8}$$

By comparing these results with the channel gains of the far-field channel model, it can be noticed that the distances between STAR-RIS elements and Rx can not be treated as the same and be brought outside of the summation. In addition, the contribution of the leaning factor should be explicitly considered in the near-field model.

3.3 Correlated STAR-RIS Phase-Shift Model

In this section, we present the proposed correlated T&R phase-shift model for STAR-RIS. Note that the independent phase-shift model presented in the last section impose no constraints on the surface impedance Z_{e} and Z_{m}. However, for passive lossless STAR element, these impedances needs to be purely imaginary, which give raise to the correlated phase-shift model. Before presenting the correlated model, we first introduce some prerequisites from physics to capture the characteristics of STAR-RIS.

3.3.1 Surface Equivalent Currents

Consider a STAR-RIS whose elements are made of a single-layered passive material. Upon being illuminated by the incident EM wave, multiple currents are induced in each element, cf. Fig. 3.3. For STAR-RIS modeling, it is sufficient to consider only two types

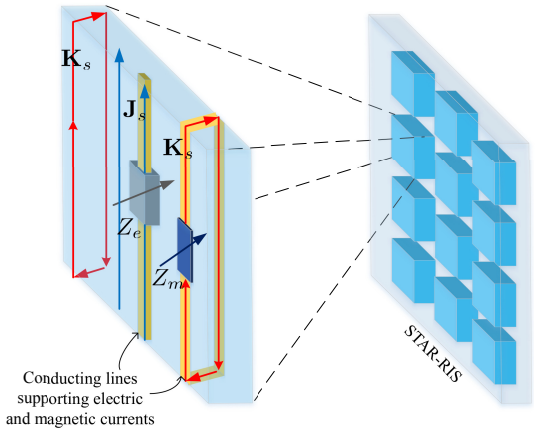

Figure 3.3: Conceptual illustration of the hardware model of the STAR-RIS.

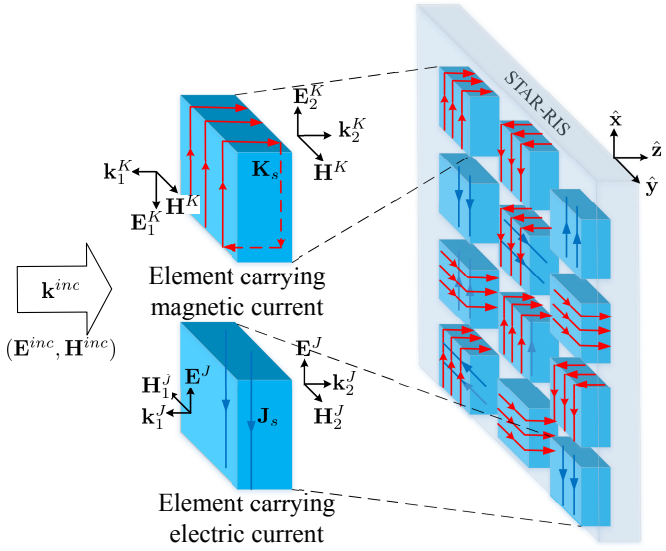

Figure 3.4: EM radiations of STAR-RIS elements carrying induced currents $\mathbf{J}_s$ and $\mathbf{K}_s$, where $\mathbf{k}^{inc}$, $\mathbf{k}_1^J$, $\mathbf{k}_2^J$, $\mathbf{k}_1^K$, and $\mathbf{k}_2^K$ denote the wave vector (wave number) of the corresponding waves.

of currents[1], namely the electric current and the magnetic current [11]. The electric current is generated by the flow of free electrical charges within the conducting part of the element media. Let $\mathbf{J}_s$ denote the electric current density. As shown in Fig. 3.4, since the electric field component of the impinging EM field is oscillating, $\mathbf{J}_s$ also oscillates and

[1]This is because in terms of radiation, the electric/magnetic charge layers and electric/magnetic current layers are equivalent [11].

thus produces EM radiation with electric field $\mathbf{E}^J$, and magnetic fields $\mathbf{H}_1^J$ and $\mathbf{H}_2^J$ on the two sides of the STAR-RIS, respectively. The magnetic current density, $\mathbf{K}_s$, is generated by vortex (circular) currents within each STAR-RIS element [10]. These currents are induced by the oscillating magnetic component of the EM field and they produce EM radiation with electric fields $\mathbf{E}_1^K$ and $\mathbf{E}_2^K$, and magnetic field $\mathbf{H}^K$. The strengths of these two types of currents are assumed to be proportional to the sum of the incident and radiated fields at the STAR-RIS. Thus, the density of the electric and magnetic currents are respectively given by

$$\mathbf{J}_s = Z_{\mathrm{e}}(\mathbf{E}^{inc} + \mathbf{E}^J), \tag{3.9}$$

$$\mathbf{K}_s = Z_{\mathrm{m}}(\mathbf{H}^{inc} + \mathbf{H}^K), \tag{3.10}$$

where Z_{e} and Z_{m} are the scalar electric and magnetic impedances of a particular element, respectively, and $\mathbf{E}^{inc}$ and $\mathbf{H}^{inc}$ are the electric and magnetic components of the incident field, respectively. To connect the EM fields on both sides of the STAR-RIS, we take into account the boundary conditions of the EM field as follows [11]:

$$\mathbf{n} \times (\mathbf{H}_1^J - \mathbf{H}_2^J) = \mathbf{J}_s \text{ and } \mathbf{n} \times (\mathbf{E}_1^K - \mathbf{E}_2^K) = \mathbf{K}_s, \tag{3.11}$$

where $\mathbf{n}$ is the unit vector perpendicular to the STAR-RIS.

3.3.2 Correlated T&R Phase-Shift Model

The strengths of the transmitted and reflected signals are determined by the magnitudes of the electric components of the transmitted and reflected EM fields. Assuming a vertically polarized wireless signal, the $\mathbf{E}$ fields are in the x-direction and the $\mathbf{H}$ fields are in the y-direction (see Fig. 3.4). Omitting the superscripts, we can rewrite these fields as $\mathbf{E} = \hat{\mathbf{x}}E$ and $\mathbf{H} = \hat{\mathbf{y}}H$, where $\hat{\mathbf{x}}$ and $\hat{\mathbf{y}}$ are the unit vectors in x-direction and y-direction, respectively, and E and H denote the complex amplitudes of the corresponding fields. Specifically, considering an element with both induced electric and magnetic currents

($\mathbf{J}_s$ and $\mathbf{K}_s$), the transmission and reflection coefficients can be expressed as follows:

$$T = \beta^T \cdot e^{j\phi^T} = (E^J + E_2^K + E^{inc})/E^{inc}, \tag{3.12}$$

$$R = \beta^R \cdot e^{j\phi^R} = (E^J + E_1^K)/E^{inc}, \tag{3.13}$$

where β^T and β^R are the real-valued transmission and reflection amplitudes, respectively, and ϕ^T and ϕ^R are the corresponding phase-shift values for transmission and reflection. Next, we study the correlation between ϕ^T and ϕ^R for a lossless STAR-RIS element. According to EM theory, the change in energy of an EM field within an arbitrary volume V is given as follows [10]:

$$\frac{\mathrm{d}W}{\mathrm{d}t} = -\int_{(\Sigma)} (\mathbf{E} \times \mathbf{H})\, \mathrm{d}\Sigma - \int_{(V)} \mathbf{J} \cdot \mathbf{E}\, \mathrm{d}V, \tag{3.14}$$

where W is the EM energy within the volume V, d/dt denotes the time derivative, $\mathbf{E}$ and $\mathbf{H}$ denote the EM fields at the boundary of V, $\mathbf{J}$ denotes the surface electric and magnetic current densities, operators $\times$ and $\cdot$ denote the cross product and dot product between two vectors, respectively, and Σ denotes the closed surface of the chosen volume V. The second term in (3.14) is the integration of the Poynting vector evaluated at the closed surface Σ, which reflects the energy loss due to EM radiation. The third term is a volume integration and it reflects the Ohmic heating and the power of other non-electrostatic forces within volume V. According to (3.14), if we choose V as the volume of a STAR-RIS element, the second term represents the EM energy radiated towards the target users, while the third term represents the energy loss in the volume. Thus, a locally lossless element requires that the time-averaged value of $\mathbf{J} \cdot \mathbf{E}$ is equal to zero for the entire element. In the context of (3.9) and (3.10), this indicates that Z_{e} and Z_{m} should have purely imaginary values. By exploiting (3.9)-(3.14), we obtain the coupled phase-shift model for passive lossless STAR-RIS as given in the following proposition.

Proposition 1. *(Proposed correlated T&R phase-shift model) For passive lossless STAR-RISs, the transmission and reflection amplitudes β_m^T and β_m^R and the phase shifts ϕ_m^T and*

ϕ_m^R of the mth element have to meet the following constraints:

$$\beta_m^T = \sqrt{1-(\beta_m^R)^2}, \tag{3.15}$$

$$\phi_m^R - \phi_m^T = \frac{\pi}{2} + \nu_m \pi,\ \nu_m = 0 \text{ or } 1,\ \forall m = 1, 2, \cdots, M, \tag{3.16}$$

where M denotes the total number of STAR-RIS elements. ν_m is referred to as the auxiliary bit[2] for the lossless STAR-RIS in the following and provides an additional degree of freedom which links the possible phase shift values between the transmission and reflection coefficients.

Proof. The relation in (3.15) is a direct consequence of the law of energy conservation, i.e., the sum of the radiation power of both sides should be equal to the power of the incident signal [50]. For (3.16), by exploiting (3.9)-(3.13), it can be shown that the complex-valued T&R coefficients of the passive STAR-RIS elements have to satisfy $|T + R| = 1$ or $|T - R| = 1$, or equivalently, $\beta_m^R \sqrt{1-(\beta_m^R)^2} \cos(\phi_m^R - \phi_m^T) = 0$. Thus, for non-zero β_m^R, the phase difference must fulfill $\phi_m^R - \phi_m^T = \pi/2$ or $3\pi/2$. □

Remark 1. *The T&R phase correlation in* (3.16) *is a consequence of Maxwell's Equations and the boundary conditions. We note that independent phase shifts are achievable if the impedances Z_{e} and Z_{m} in* (3.9) *and* (3.10) *can take on arbitrary complex values. However, a non-zero real part of Z_{e} and Z_{m} indicates that the STAR-RIS requires active or lossy elements, which might significantly increase the manufacturing cost.*

3.4 System Model

To investigate the impact of the proposed correlated T&R phase-shift model given in (3.16) on wireless system performance, we consider a STAR-RIS-aided two-user downlink system, as illustrated in Fig. 3.5. A single-antenna base station (BS) serves two single-

[2] ν_m can only take on two values, 0 or 1. Thus, its value represents the two possible phase difference between ϕ_m^R and ϕ_m^T, i.e., the phase difference is either $\pi/2$ or $3\pi/2$.

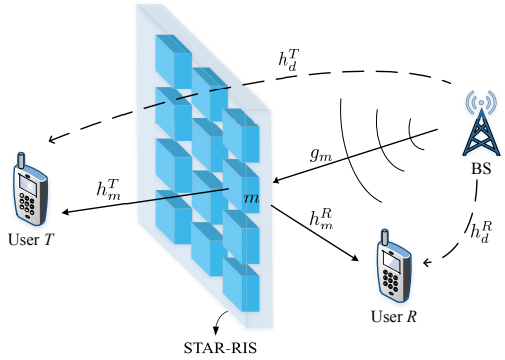

Figure 3.5: System model.

antenna users, which are located on different sides of the STAR-RIS. The user located in the transmission region of the STAR-RIS is referred to as user T, while the user located in the reflection region is referred to as user R. The channel between the BS and the mth STAR-RIS element is denoted by g_m and the channels between the mth STAR-RIS element and user T and user R are denoted by h_m^T and h_m^R, respectively. Let $h_d^{T/R}$ denote the direct link between the BS and user T/R. All channels are assumed to be independent and identically distributed (i.i.d.) Rician fading channels[3]. Thus, for $\chi \in \{T, R\}$, indicating user T/R, h_m^χ can be expressed as follows:

$$h_m^\chi = \sqrt{\frac{\rho_0^\chi}{(d_m^\chi)^\alpha}} \left(\sqrt{\frac{K_h^\chi}{K_h^\chi+1}} h_m^{\mathrm{LoS},\chi} + \sqrt{\frac{1}{K_h^\chi+1}} h_m^{\mathrm{NLoS},\chi} \right), \tag{3.17}$$

where d_m^χ denotes the distance between the mth STAR-RIS element and user χ, α is the path loss exponent, K_h^χ denotes the Rician factor, ρ_0^χ is the path loss at a reference distance of 1 meter, $h_m^{\mathrm{LoS},\chi}$ is the LoS component, and $h_m^{\mathrm{NLoS},\chi}$ is the non-line-of-sight (NLoS) component which is Rayleigh fading. Channels g_m and h_d^χ are modeled similarly to (3.17) with Rician factors K_g and K_d^χ, respectively.

In the following analysis, we assume that the statistical channel state information of the STAR-RIS cascaded channel $g_m h_m^\chi$ and the direct channel h_d^χ are known at the STAR-RIS. This can be done by using the channel estimation scheme proposed in [52].

[3]According to [51], i.i.d. fading can be achieved by employing uniform linear arrays with $\lambda/2$-separation between adjacent antennas.

With channel information known, the performance of STAR-RIS-aided networks depends on the choice of the phase shifts (ϕ_m^T, ϕ_m^R) and the amplitudes (β_m^T, β_m^R) applied by each element. This is because the end-to-end channel between the BS and user χ is given by:

$$H^{\chi} = \sum_{m=1}^{M} g_m h_m^{\chi} \beta_m^{\chi} e^{j\phi_m^{\chi}} + h_d^{\chi}, \ \chi \in \{T, R\}. \tag{3.18}$$

For ease of presentation, we rewrite the overall channel by separating the amplitude terms and the phase-shift terms as follows:

$$H^{\chi} = \sum_{m=1}^{M} \beta_m^{\chi} |g_m||h_m^{\chi}| \exp\{j(\angle g_m + \angle h_m^{\chi} + \phi_m^{\chi})\} + h_d^{\chi}, \tag{3.19}$$

where $\angle\xi$ denotes the argument (complex angle) of a complex number ξ.

3.4.1 Multiple Access

In this chapter, both OMA and NOMA are considered for the BS to serve the users. In OMA, the BS serves both users in orthogonal frequency bands of equal size. In NOMA, the BS sends a superimposed signal to both users in the same time/frequency resource block. Let s^{χ} and c_{χ} denote the information symbol and the power allocation coefficient for user χ, respectively. In the following, we outline both considered multiple access schemes.

3.4.1.1 OMA

In this case, the BS communicates with both users in orthogonal frequency bands employing frequency-division multiple access (FDMA). Thus, the achievable rate for user χ is given by:

$$R_{\chi}^{\mathrm{OMA}} = \frac{1}{2} \log_2 \left(1 + \frac{P_{BS} c_{\chi}^2 |H^{\chi}|^2}{\sigma_0^2/2} \right) \quad [\mathrm{bit/s/Hz}], \tag{3.20}$$

where P_{BS} and σ_0^2 are the transmit power of the BS and the variance of the additive white Gaussian noise (AWGN) at both users, respectively. In (3.20), we assume that the users employ orthogonal frequency bands of equal size. Thus, the bandwidth and the

noise are both reduced by 1/2.

3.4.1.2 NOMA

For NOMA, successive interference cancellation (SIC) is employed at the user enjoying better channel conditions. For simplicity, we assume that user R has the better channel, i.e., $|H^R| \geq |H^T|$. Recall that in Fig. 3.5, user R and the BS are on the same side of the STAR-RIS. As a result, the direct link of user R is stronger than user T due to the shorter path-length. To ensure that SIC is successfully carried out and to guarantee user fairness, the power allocation coefficients follow $c_R < c_T$. Therefore, user R will first detect the signal of user T via SIC, before detecting its own signal. The achievable rate for user R to detect the message of user T is given by

$$R_{R,T}^{\mathrm{NOMA}} = \log_2\left(1 + \frac{P_{BS}c_T^2|H^R|^2}{P_{BS}c_R^2|H^R|^2 + \sigma_0^2}\right) \quad [\mathrm{bit/s/Hz}]. \tag{3.21}$$

Then, user R can detect its own signal after subtracting the signal of user T via SIC. Hence, the achievable rate of user R is given as follows:

$$R_{R,R}^{\mathrm{NOMA}} = \log_2\left(1 + \frac{P_{BS}c_R^2|H^R|^2}{\sigma_0^2}\right) \quad [\mathrm{bit/s/Hz}]. \tag{3.22}$$

In contrast, user T will directly detect its own signal by treating the signal of user R as interference. The corresponding achievable rate is given by:

$$R_{T,T}^{\mathrm{NOMA}} = \log_2\left(1 + \frac{P_{BS}c_T^2|H^T|^2}{P_{BS}c_R^2|H^T|^2 + \sigma_0^2}\right) \quad [\mathrm{bit/s/Hz}]. \tag{3.23}$$

3.5 Practical Phase-Shift Configuration Strategies for STAR-RISs

In this section, we propose three STAR-RIS PSC strategies for the proposed correlated phase-shift model in (3.16), namely the primary-secondary (PS)-PSC, the diversity pre-

serving (DP)-PSC, and the T/R-Group (TR)-PSC strategies. We note that due to the T&R phase-shift correlation in (3.16), existing results on phase-shift optimization for conventional RISs and STAR-RISs with independent phase shifts are not applicable for the considered passive STAR-RISs.

3.5.1 Primary-Secondary Phase-Shift Configuration (PS-PSC) Strategy

For the PS-PSC strategy, we adjust the phases of the T&R coefficients while assuming that the power ratio between the amplitudes of the T&R coefficients is fixed to the same value for each STAR-RIS element. The STAR-RIS can be optimized for enhancing the channel gain of one user, referred to as the primary user, while simultaneously serving the other user, referred to as the secondary user. Based on this strategy, the PSC of the STAR-RIS elements can be determined in the following two steps. Without loss of generality, assume that user R is the primary user. In the first step, the phase terms $\{\phi_1^R, \cdots, \phi_M^R\}$ are configured to maximize the channel gain of user R without considering the phase-shift correlation constraint in (3.16). This yields the following optimization problem:

$$\max_{\phi_1^R, \cdots, \phi_M^R} |H^R|^2, \text{ s.t. } \phi_m^R \in [0, 2\pi), \ \forall m = 1, 2, \cdots, M. \tag{3.24}$$

In the second step, the $\{\phi_1^T, \cdots, \phi_M^T\}$ are optimized to maximize the overall channel gain of user T for given $\{\phi_1^{R^*}, \cdots, \phi_M^{R^*}\}$ taking into account the phase-shift correlation model in (3.16). In this case, the optimization of ϕ_m^T under constraint (3.16) is equivalent to optimizing the auxiliary bits $\{\nu_1, \cdots, \nu_M\}$ of the STAR-RIS, which leads to the following optimization problem:

$$\max_{\nu_1, \cdots, \nu_M} |H^T|^2, \text{ s.t. } \nu_m = 0 \text{ or } 1, \ \forall m = 1, 2, \cdots, M. \tag{3.25}$$

Since constraint (3.16) is not taken into account for the maximization with respect to $\phi_1^R, \cdots, \phi_M^R$ in (3.24), the optimal values of both $\phi_1^R, \cdots, \phi_M^R$ and $\nu_1, \cdots, \nu_M$ can be

$(\Delta\phi_m^R - \Delta\phi_m^T) \in$	$[0, \pi)$	$[\pi, 2\pi)$	$[-\pi, 0)$	$(-2\pi, -\pi)$
$\phi_m^{T^*}$	$\phi'_m - \frac{\pi}{4}$	$\phi'_m - \frac{3\pi}{4}$	$\phi'_m + \frac{\pi}{4}$	$\phi'_m + \frac{3\pi}{4}$
ν^*	0	1	1	0
$\phi_m^{R^*}$	$\phi'_m + \frac{\pi}{4}$	$\phi'_m + \frac{3\pi}{4}$	$\phi'_m - \frac{\pi}{4}$	$\phi'_m - \frac{3\pi}{4}$

Table 3-A: Diversity preserving phase-shift configuration strategy, $\phi'_m = (\Delta\phi_m^R + \Delta\phi_m^T)/2$.

obtained in closed form if the channel state information is known. According to the cophase condition [39], the optimal solution to problem (3.24) is given by:

$$\phi_m^{R^*} = (\angle h_d^R - \angle h_m^R - \angle g_m) \mod 2\pi. \tag{3.26}$$

For the secondary user, the phase shift according to the cophase condition would follow as $\phi_m^{T'} = (\angle h_d^T - \angle h_m^T - \angle g_m) \mod 2\pi$. However, this phase shift value might not be possible because of (3.16) for the given $\phi_m^{R^*}$. Thus, we obtain the optimal choice of the auxiliary bits as follows:

$$\nu_m^* = \begin{cases} 0 & \text{if } \phi_0^T \le \phi_m^{R^*} < \phi_0^T + \pi, \\ 1 & \text{if } \phi_0^T - \pi \le \phi_m^{R^*} < \phi_0^T, \end{cases} \tag{3.27}$$

where $\phi_0^T = \angle h_d^T$ is the phase of the direct link between user T and the BS. The PSC in (3.27) effectively selects the ϕ_m^T value which is closer to $\phi_m^{T'}$ given the two possible choices, i.e., $\phi_m^T = \phi_m^{R^*} - \pi/2$ and $\phi_m^T = \phi_m^{R^*} - 3\pi/2$.

3.5.2 Diversity Preserving Phase-Shift Configuration (DP-PSC) Strategy

One of the claimed benefits of STAR-RISs is that they can achieve full diversity orders for both the user T and the user R [24]. Here, we show that this is possible even for STAR-RISs with correlated T&R phase shifts. To this end, we propose a DP-PSC strategy. For given amplitude coefficients, the phase shifts and the values of the auxiliary bits are determined as follows: First, according to the cophase condition, we calculate the

phase-shift value that would maximize the channel gains of both users without taking into account the phase-shift correlation constraint. This leads to

$$\Delta\phi_m^{\chi} = (\angle h_d^{\chi} - \angle h_m^{\chi} - \angle g_m) \mod 2\pi. \tag{3.28}$$

Then, taking the phase correlation into account, the PSC for the DP-PSC strategy is determined based on the calculated phase-shift values $\Delta\phi_m^R$ and $\Delta\phi_m^T$, and is given in Table 3-A along with the corresponding auxiliary bit ν. To illustrate the idea behind this PSC, let $\delta_m^{\chi} = |\phi_m^{\chi^*} - \Delta\phi_m^{\chi}|$ denote the phase error for user χ. The PSC given in Table 3-A imposes identical phase errors on both users, i.e., $\delta_m^R = \delta_m^T$. Moreover, it can be verified that $\delta_m^{\chi} \leq \pi/4$. This property is crucial for the DP-PSC strategy to exploit the spatial diversity of the STAR-RIS, cf. Section 3.8.

3.5.3 T/R-Group Phase-Shift Configuration (TR-PSC) Strategy

Similar to the mode-switching protocol in [53], for the proposed TR-PSC strategy, the elements of the STAR-RIS are partitioned into two groups. The elements in the T group employ full transmission and serve only the user T, while the elements in the R group employ full reflection and serve only the user R. For the fully reflecting elements, we have $\beta_m^R = 1$ and $\beta_m^T = 0$, and for the fully transmitting elements, we have $\beta_m^T = 1$ and $\beta_m^R = 0$. Due to the decoupling of transmission and reflection at the element level, the phase correlation constraint in (3.16) does not apply to the TR-PSC strategy. Let $\mathcal{T}$ denote the set of indices of the elements in the T group. Then, the transmission and reflection coefficients for the TR-PSC strategy are given by:

$$\phi_m^R = \angle h_d^R - \angle h_m^R - \angle g_m, \ m \notin \mathcal{T}, \tag{3.29}$$

$$\phi_m^T = \angle h_d^T - \angle h_m^T - \angle g_m, \ m \in \mathcal{T}. \tag{3.30}$$

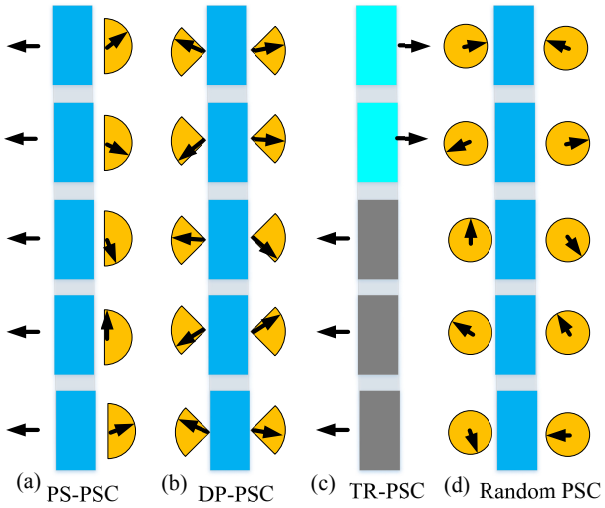

Figure 3.6: Conceptual illustration of different STAR-RIS PSC strategies.

3.5.4 Summary and Discussion

In Fig. 3.6, we illustrate the three proposed PSC strategies for STAR-RISs and the random PSC as a baseline scheme. According to (3.19), at user χ, the overall phase of the signal received from element m is $\angle g_m + \angle h_m^{\chi} + \phi_m^{\chi}$. The small arrows in Fig. 3.6 indicate these overall phase terms. Under the assumption of i.i.d. fading channels, the yellow areas denote the possible ranges of the values of the overall phase terms. Note that these sectors are different in size for the different users and for different designs, and indicate the possible deviation of the actual phase shift from the optimal values given by the cophase condition. As shown in Fig. 3.6(a), the overall phase terms for the primary user under the PS-PSC strategy and for both users under the TR-PSC strategy are equal to the values obtained from the cophase condition. In contrast, the yellow sectors of the secondary user for the PS-PSC strategy have central angles of 180 degrees. The central angles of the yellow sectors of users under the DP-PSC strategy and the random PSC are 90 and 360 degrees, respectively. These deviations of the overall phase terms are different for different PSC strategies, which leads to significant performance difference for the users.

3.6 Relaxing Phase-Shift Correlation using Lossy Elements

In the previous section, we have shown that correlation between the T&R phase-shift coefficients impose significant limitation on the passive-beamforming design of STAR-RIS. However, it is also possible to allow energy loss to obtain more flexibility in T&R phase-shift design. In practice, using a very thin and lossy STAR-RIS element may be beneficial and significantly simplify T&R phase-shift design. In the following, we present the device model for these thin and lossy elements.

Corollary 1. *For patch-array based STAR-RISs with negligible thicknesses, the discontinuity of only the electric component of the field is supported, and we have* $Z_{\mathrm{m}} = 0$*. This means there is no discontinuity for the transverse component of the magnetic field at the surface. By substituting* $Z_{\mathrm{m}} = 0$ *into* (3.10)*, we have:*

$$T_m - R_m = 1. \tag{3.31}$$

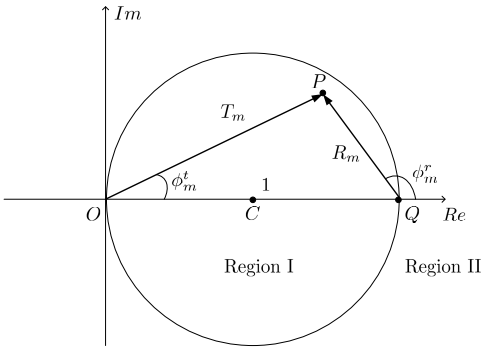

Figure 3.7: Illustration of R_m and T_m on the complex plane.

In this case, we arrive at (3.31) as another fundamental condition on reflection and refraction coefficients for passive lossless or lossy STAR-RISs. The diagram in Fig. 3.7 illustrates these conditions for the amplitudes and phases for R_m and T_m on the complex plane. In Fig. 3.7, the circle is centered at point C with diameter OQ of length equals to one. With condition (3.31), the T&R coefficients for each element are determined corresponding to the position of point P in Fig. 3.7. According to (3.2), if point P is in

Region I (within the circle), $\vec{QP}$ and $\vec{OP}$ represent legitimate reflection and refraction coefficients for a lossy STAR-RIS. If point P is on the circle, the corresponding vectors represent the reflection and refraction coefficients for a lossless element. If point P is in *Region II* (outside of the circle), the corresponding reflection and refraction coefficients can only be achieved by an active element.

As can be observed in the figure, if point P is on the circle, we have $\phi_m^R - \phi_m^T = \phi/2$, which satisfy the correlated T&R phase-shift model given in (3.16). However, if we allow point P to freely move inside the unit circle, i.e., using lossy elements, this phase-shift correlation is relaxed. In practice, a group of N PIN diodes or varactor diodes are used to configure the STAR element into different phase-shift states [5]. Specifically, each one state in the overall 2^N states corresponds to one T&R phase-shift tuple, i.e., (T_m, R_m). If lossy elements are used, more flexibility is allowed so that the phase of R_m can be continuously changed while T_m takes on a fixed value.

3.7 Key Performance Metrics

In wireless communications, several performance metrics are used to evaluate the quality and efficiency of a communication system. Some of these metrics include bit error rate (BER), outage probability, diversity order, spectral efficiency, and capacity region. In the following, we first discuss these performance metrics in the context of RIS-aided wireless communication networks. Then, we provide the mathematical definitions of outage probability and diversity order which are chosen as the key performance metrics in our analysis.

3.7.1 Performance Metrics in the Context of RIS-Aided Wireless Communications

By examining different performance metrics in RIS-aided wireless communication, the impact of RIS deployment, channel characteristics, and system parameters on key performance indicators can be evaluated. This analysis aids in optimizing RIS configuration,

power allocation, and transmission strategies to achieve higher reliability, improved spectral efficiency, and enhanced overall system capacity.

1. Bit Error Rate (BER): BER quantifies the probability of bit errors in the received signal. In RIS-aided systems, BER reflects the accuracy of data transmission considering the effects of RIS-induced channel impairments, such as fading and reflections. Analyzing BER helps in evaluating the performance of modulation and coding schemes and assessing the system's error resilience.

2. Outage Probability: Outage probability refers to the probability that the received signal falls below a certain threshold, resulting in an outage or loss of communication. In RIS-aided systems, outage probability accounts for the impact of RIS deployment, channel fading, and interference. Analyzing outage probability helps in understanding the system's reliability and determining appropriate power allocation and resource allocation strategies.

3. Diversity Order: Diversity order characterizes the system's ability to combat fading and improve reliability by exploiting multiple independent signal paths. In RIS-aided systems, diversity order relates to the number of independent paths created by the RIS reflections, which can mitigate fading effects and enhance signal strength. A higher diversity order implies improved system performance in terms of error probability and outage resilience.

4. Spectral Efficiency: Spectral efficiency measures the amount of information that can be reliably transmitted over a given bandwidth. In RIS-aided systems, spectral efficiency considers the impact of RIS-induced beamforming and channel reflections on enhancing signal strength and reducing interference. Maximizing spectral efficiency enables higher data rates and improved utilization of available spectrum resources.

5. Capacity Region: The capacity region represents the set of all achievable rate tuples in a multi-user communication system. It characterizes the system's max-

imum achievable data rates for different users or channels. In RIS-aided systems, the capacity region takes into account the unique properties of RIS-assisted communication, such as beamforming, interference mitigation, and channel enhancements. Analyzing the capacity region helps in optimizing resource allocation, user scheduling, and achieving efficient multi-user communication.

3.7.2 Outage Probability and Diversity Order

In the following analysis, we focus on outage probability and diversity order. The reasons are as follows: In RIS-aided systems, outage probability accounts for the impact of RIS deployment, channel fading, and interference. For STAR-RIS, the phase-shift alignment of the T&R coefficients are directly reflected on the users outage probabilities. Furthermore, STAR-RISs can create additional signal paths through simultaneous transmission and reflection, effectively increasing the diversity order. A higher diversity order implies improved system performance in terms of error probability and outage resilience. By analyzing the diversity order, we can understand the benefits of STAR-RIS-induced transmission/reflections in mitigating fading effects and enhancing signal strength. It guides further optimization to the STAR-RIS PSC strategies proposed in Section. 3.5 to achieve higher diversity order and improve overall system performance.

- Outage Probability: The outage probability, denoted as P_{out}, is defined as the probability that the received signal power falls below a certain threshold γ_{th}. Mathematically, it can be expressed as:

$$P_{\text{out}} = \Pr(\text{SNR} < \gamma_{\text{th}}). \tag{3.32}$$

- Diversity Order: The diversity order, denoted as d, quantifies the rate of decay of the error probability with respect to the transmit power or SNR. The diversity

order of a user is defined as follows [54]:

$$d = -\lim_{P_{BS}\to\infty} \frac{\log P_{\text{out}}}{\log P_{BS}}, \tag{3.33}$$

where P_{BS} represents the transmit power. The diversity order d indicates the slope of the outage probability curve in logarithmic scale, representing the system's ability to combat fading. A higher diversity order implies a faster decay of error probability with increasing SNR, indicating better system performance in terms of reliability and robustness against channel impairments.

3.8 Performance Analysis

In the following, the communication performance of the T and R users is analyzed for the proposed PSC strategies and performance lower and upper bounds are established. Specifically, we first derive the outage probabilities and diversity orders for the proposed PSC strategies. Then, we study the power scaling law, which quantifies how the average received power scales with the number of STAR-RIS elements.

3.8.1 Outage Probability

3.8.1.1 OMA

For FDMA, the BS serves the users in two orthogonal frequency bands of equal sizes employing frequency-flat STAR-RIS transmission and reflection coefficients. Suppose that for user χ the target data rate is $\tilde{R}_\chi$. Then, according to (3.20), the outage probability for the user is given by

$$P_{\text{out},\chi}^{\text{OMA}} = \Pr\left\{R_\chi^{\text{OMA}} < \tilde{R}_\chi\right\} = \Pr\left\{|H^\chi|^2 < \frac{(2^{2\tilde{R}_\chi}-1)\sigma_0^2}{2c_\chi^2 P_{BS}}\right\}, \tag{3.34}$$

where $\Pr\{A\}$ denotes the probability of event A. For ease of exposition, we define the following term as the OMA channel gain threshold for target data rate $\tilde{R}_\chi$:

$$\tau_\chi^{\text{OMA}}(\tilde{R}_\chi) \triangleq (2^{2\tilde{R}_\chi} - 1)\sigma_0^2/(2c_\chi^2). \tag{3.35}$$

3.8.1.2 NOMA

Suppose that for NOMA user χ, the target data rate is $\tilde{R}_\chi$. Moreover, we consider the case where user R has the better channel condition. For given target data rates $\tilde{R}_T$ and $\tilde{R}_R$ of the users, their outage probabilities can be formulated as follows:

$$P_{\text{out},R}^{\text{NOMA}} = \Pr\left\{|H^R|^2 < \max\left\{\frac{(2^{\tilde{R}_T} - 1)\sigma_0^2}{\left[c_T^2 - (2^{\tilde{R}_T} - 1)c_R^2\right]P_{BS}}, \frac{(2^{\tilde{R}_R} - 1)\sigma_0^2}{c_R^2 P_{BS}}\right\}\right\}, \tag{3.36}$$

$$P_{\text{out},T}^{\text{NOMA}} = \Pr\left\{|H^T|^2 < \frac{(2^{\tilde{R}_T} - 1)\sigma_0^2}{\left[c_T^2 - (2^{\tilde{R}_T} - 1)c_R^2\right]P_{BS}}\right\}. \tag{3.37}$$

For convenience, we define the following two NOMA channel gain thresholds:

$$\tau_R^{\text{NOMA}} \triangleq \max\left\{\frac{(2^{\tilde{R}_T} - 1)\sigma_0^2}{c_T^2 - (2^{\tilde{R}_T} - 1)c_R^2}, \frac{(2^{\tilde{R}_R} - 1)\sigma_0^2}{c_R^2}\right\}, \tag{3.38}$$

$$\tau_T^{\text{NOMA}} \triangleq \frac{(2^{\tilde{R}_T} - 1)\sigma_0^2}{c_T^2 - (2^{\tilde{R}_T} - 1)c_R^2}. \tag{3.39}$$

Since both $\tilde{R}_R$ and $\tilde{R}_T$ appear in (3.36), for NOMA, user R will experience an outage if the target data rate of user T is chosen too large. This is because in SIC, user R will declare an outage either when it cannot decode its own message or when it cannot decode the message of user T.

3.8.2 PS-PSC Strategy

For the the primary user (user R in the considered case), the overall channel gain in (3.19) can be rewritten as follows:

$$H^R = \beta^R \sum_{m=1}^{M} |g_m||h_m^R| + h_d^R, \tag{3.40}$$

where β^R is the amplitude of the reflection coefficient shared by all STAR-RIS elements, i.e., $\beta_m^R = \beta^R$, $\forall m = 1, 2, \cdots, M$, in (3.15).

3.8.2.1 Outage Probability

Given the overall channel gain in (3.40), we obtain the following result:

Theorem 1. *For the primary user (user R), the asymptotic outage probability for NOMA and OMA can be expressed as follows:*

$$\begin{aligned} P_{out}^R(\tau_R) = &\frac{2^{M+1}(K_h^R+1)^M(K_g+1)^M(K_d+1)}{(2M+2)!\ \Omega_h^M\Omega_g^M\Omega_d^\chi}(\beta^R)^{-2M} \\ &\cdot e^{-MK_h^R-MK_g-K_d^R}(\tau_R)^{M+1}P_{BS}^{-(M+1)}, \end{aligned} \tag{3.41}$$

where $\tau_R = \tau_R^{NOMA}$ for NOMA and $\tau_R = \tau_R^{OMA}$ for OMA, and Ω_d^χ is the scale parameter of the direct link of user χ.

Proof. See Appendix A.1. □

Next, we investigate the diversity order of user χ, which is defined in (3.33).

Corollary 2. *The diversity orders of the primary user for the PS-PSC strategy are identical for both NOMA and OMA. Exploiting* (3.41) *and using* (3.33)*, the diversity order for the primary user is given by:*

$$d_{primary} = M + 1. \tag{3.42}$$

Proof. Combining (3.41) with (3.33), it is straightforward to obtain (3.42). □

For the secondary user, the overall channel can be rewritten as follows:

$$H^T = \sum_{m=1}^{M} |g_m||h_m^T| e^{j\phi'_m} \beta^T e^{j\phi_m^T} + h_d^T, \tag{3.43}$$

$$= \beta^T \sum_{m=1}^{M} |g_m||h_m^T| e^{j(\phi_0^T + \delta_m)} + h_d^T, \tag{3.44}$$

where $e^{j\phi'_m}$ is the phase of $g_m h_m^T$, $\delta_m = \phi'_m + \phi_m^T - \phi_0^T$ is the residual phase, which satisfies $-\pi/2 < \delta_m < \pi/2$ according to (3.16) and (3.27), ϕ_0^T is the phase of the direct channel between user T and the BS, and β^T is the amplitude of the transmission coefficient which is assumed to be equal for all STAR-RIS elements, i.e., $\beta_m^T = \beta^T = \sqrt{1-(\beta^R)^2}$, $\forall m = 1, 2, \cdots, M$. As a result, for the secondary user, the STAR-RIS elements can be regarded as a one-bit phase shifter. The asymptotic behaviour and diversity order for one-bit phase shifters has been studied in [55]. Hence, given the presence of the direct BS-user link, the diversity order of the secondary user (user T) for both NOMA and OMA is given by[4]:

$$d_{secondary} = \frac{M+3}{2}. \tag{3.45}$$

Remark 2. *The diversity orders given in* (3.42) *and* (3.45) *include the contribution of the direct channel h_d^χ. For the scenario where the direct link is blocked, it can be shown that the diversity orders decrease by one, which leads to the following results:*

$$d'_{primary} = M, \; d'_{secondary} = \frac{M+1}{2}. \tag{3.46}$$

3.8.2.2 Power Scaling Law

Due to the asymmetric PSC, the power scaling laws will be different for user R and user T. For convenience, let μ_h^χ and σ_h^χ denote the expected value and the variance of the

[4]The diversity order of user R and user T switches if user T is the primary user.

amplitude of h_m^{χ}, respectively. The following results hold [56]

$$\mu_h^{\chi} = \frac{1}{2}\sqrt{\frac{\pi\Omega_h^{\chi}}{(K_h^{\chi}+1)}}L_{1/2}(-K_h^{\chi}), \tag{3.47}$$

$$\sigma_h^{\chi} = \Omega_h^{\chi} - (\mu_h^{\chi})^2, \tag{3.48}$$

where $L_{1/2}(x)$ denotes the Laguerre polynomial. For the primary user, according to (3.40) and given that the $|h_m^R|$ are assumed to be i.i.d. Rician random variables, the expected value and variance of H^R can be express as follows:

$$\begin{aligned}\mathbb{E}[|H^R|] &= |g|\beta^R \sum_m \mathbb{E}[|h_m^R|] + \mathbb{E}[|h_d^R|] \\ &= M\mu_h^R|g|\beta^R + \mathbb{E}[|h_d^R|],\end{aligned} \tag{3.49}$$

$$\mathrm{Var}[|H^R|] = M\sigma_h^R|g|^2(\beta^R)^2 + \mathrm{Var}[|h_d^R|], \tag{3.50}$$

where $|g| = \mathbb{E}[|g_m|]$ is the expected magnitude of the channel between the mth STAR-RIS element and the BS.

For the secondary user, according to (3.44), the overall channel H^T is a complex-valued sum of the channel amplitude terms $|h_m^T|$ and the phase-shift terms $e^{j(\phi_0^T+\delta_m)}$. Due to the complexity of this mathematical expression, we first present a lemma as a building block for the power scaling analysis for the secondary user. We rewrite the overall channel of the secondary user as $H^T = h_s^T + h_d^T$, where $h_s^T = \beta^T \sum_{m=1}^{M} |g_m||h_m^T|e^{j(\phi_0^T+\delta_m)}$ is the STAR-RIS-aided channel.

Lemma 1. *The PDF of the magnitude of h_s^T can be approximated as follows*[5]*:*

$$f_{|h_s^T|}(x) = \frac{x}{\beta^2}e^{-\frac{x^2+\alpha^2}{2\beta^2}}I_0\left(\frac{x\alpha}{\beta}\right), \tag{3.51}$$

[5]Numerical results presented in [8] showed that the Kullback–Leibler (KL) divergence between the approximated PDF in (3.51) and the exact distribution of $|h_s^T|$ is less than 0.05 for a 16×16 element RIS.

where

$$\alpha = 2M\mu_h^T/\pi,\ \beta^2 = \frac{M}{2}\Omega_h^T, \tag{3.52}$$

and $I_0(x)$ *denotes the modified Bessel function of the first kind.*

Proof. See Appendix A.2. □

Theorem 2. *Under the PS-PSC strategy, the power scaling laws of the two users are given by:*

$$\begin{aligned} P_{primary} = P_r^R =& M^2 \cdot (\mu_h^R|g|\beta^R)^2 + M \cdot \Big\{\sigma_h^R|g|^2(\beta^R)^2 \\ &+ 2\mu_h^R|g|\beta^R\mathbb{E}[|h_d^R|]\Big\} + \mathbb{E}[|h_d^R|^2], \end{aligned} \tag{3.53}$$

and

$$\begin{aligned} P_{secondary} = P_r^T =& \frac{4}{\pi^2}M^2 \cdot (\mu_h^T|g|\beta^T)^2 + M \cdot \Big\{\sigma_h^R|g|^2(\beta^T)^2 \\ &+ 2\mu_h^T|g|\beta^T\mathbb{E}[|h_d^T|]\Big\} + \mathbb{E}[|h_d^T|^2]. \end{aligned} \tag{3.54}$$

Proof. For the primary user, the received power can be calculated as follows:

$$P_r^R = \mathbb{E}[|H^R|^2] = \mathrm{Var}[|H^R|] + (\mathbb{E}[|H^R|])^2. \tag{3.55}$$

Thus, the power scaling law of the primary user can be obtained by substituting (3.49) and (3.50) into (3.55). For the secondary user, we have $P_r(T) = \int_0^\infty x^2 f_{|h_s^T|}(x)dx + \mathbb{E}[|h_d^T|^2]$. By using the the PDF of $|h_s^T|$ in (3.51), the scaling law in (3.54) is proved. □

Remark 3. *The power scaling law in* (3.53) *can be further simplified for STAR-RISs with sufficiently large numbers of elements. For the case where* $M \gg 1$*, the received*

power simply scales with M^2 in the large M regime, i.e.,

$$P_r^{\chi} \propto \tilde{f}_{\chi} \cdot M^2, \tag{3.56}$$

where $\tilde{f}_R = (\mu_h^R \beta^R)^2$ and $\tilde{f}_T = (\frac{2}{\pi}\mu_h^T \beta^T)^2$. This result is consistent with the existing power scaling analysis for conventional reflecting-only RIS [29]. However, the received power of the secondary user is reduced by a factor of $(2/\pi)^2$ compared with that of the primary user.

3.8.3 DP-PSC Strategy

In this subsection, we demonstrate that the DP-PSC strategy indeed achieves full diversity order for the users on both sides of the STAR-RIS. For the convenience of the subsequent analysis, we rewrite the phase-shift value of the mth element for user χ as follows:

$$\phi_m^{\chi} = \Delta\phi_m^{\chi} + \delta_m^{\chi}, \tag{3.57}$$

where $\Delta\phi_m^{\chi}$ is the phase shift that achieves cophasing for user χ and $\delta_m^{\chi} = \phi_m^{\chi} - (\angle h_d^{\chi} - \angle h_m^{\chi} - \angle g_m) \mod 2\pi$ is the deviation from this optimal value due to the phase correlation. Based on the channel model presented in Section 3.5, by plugging (3.57) into (3.19), the overall channel for user χ can be rewritten as follows:

$$H^{\chi} = \beta^{\chi} \sum_{m=1}^{M} |g_m||h_m^{\chi}| \exp\{j(\angle h_d^{\chi} + \delta_m^{\chi})\} + h_d^{\chi}. \tag{3.58}$$

3.8.3.1 Outage Probability

Due to the complexity of the DP-PSC strategy, it is very challenging to obtain the exact channel distribution for both users. To address this issue, we introduce the following theorem based on which the diversity orders of user T and user R can be obtained.

Theorem 3. *The outage probabilities of user T and user R are upper-bounded by:*

$$\begin{aligned} P_{out}^{\chi}(\tau_\chi) \leq & \left(F(\tau_\chi, K_g, K_h^\chi, \Omega_g, \Omega_h^\chi)\right)^M \\ & \cdot \left(1 - Q(\sqrt{2K_d^\chi}, \sqrt{2\tau_\chi(K_d^\chi+1)/\Omega_d^\chi P_{BS}})\right), \end{aligned} \tag{3.59}$$

where $\tau_\chi = \tau_\chi^{NOMA}$ *for NOMA and* τ_χ^{OMA} *for OMA,* $Q(a,b)$ *is the Marcum Q-function, which is defined as follows:*

$$Q(a,b) = \int_b^\infty x \cdot \exp\left(-\frac{x^2+a^2}{2}\right) I_0(ax)dx, \tag{3.60}$$

$I_0(x)$ *denotes the modified Bessel function of the first kind, and* $F(\tau_\chi, K_g, K_h^\chi, \Omega_g, \Omega_h^\chi) = \Pr\left\{|g_m||h_m^\chi| \leq \sqrt{\frac{\tau_\chi}{P_{BS}}}\right\}$. *A closed-form expression for F can be obtained using the exact PDF of* $|g_m||h_m^\chi|$*, i.e., a product of two Rician variables [56], which is omitted here for brevity.*

Proof. In (3.58), the phase difference between any two terms in the summation is always less than π, i.e., $|\delta_p^\chi - \delta_q^\chi| \leq \pi,\ \forall p, q \in \{1, 2, \cdots, M\}$. Thus, according to the law of cosines, we have the following proposition:

$$\begin{aligned} |H^\chi| < \sqrt{\frac{\tau_\chi}{P_{BS}}} \ \Rightarrow \ & \left(|h_d^\chi| < \sqrt{\frac{\tau_\chi}{P_{BS}}}\right) \wedge \\ & \left(|g_1||h_1^\chi| < \sqrt{\frac{\tau_\chi}{P_{BS}}}\right) \wedge \cdots \wedge \left(|g_M||h_M^\chi| < \sqrt{\frac{\tau_\chi}{P_{BS}}}\right), \end{aligned} \tag{3.61}$$

where P $\Rightarrow$ Q means proposition P leads to Q and $\wedge$ is the *logical AND operator*. Since $|H_1|, |H_2|, \cdots, |H_M|$ are i.i.d. random variables, according to probability theory, we have the following result:

$$P_{out}^{\chi} \leq \left(\Pr\left\{|g_m||h_m^\chi| \leq \sqrt{\frac{\tau_\chi}{P_{BS}}}\right\}\right)^M \cdot \Pr\left\{|h_d^\chi| \leq \sqrt{\frac{\tau_\chi}{P_{BS}}}\right\}. \tag{3.62}$$

Finally, the second term on the right-hand side of (3.62) can be calculated using the

Rician PDF of $|h_d^\chi|$ as follows:

$$\Pr\left\{|h_d^\chi| \leq \sqrt{\frac{\tau_\chi}{P_{BS}}}\right\} = 1 - Q\left(\sqrt{2K_d^\chi}, \sqrt{\frac{2\tau_\chi(K_d^\chi+1)}{\Omega_d^\chi P_{BS}}}\right). \tag{3.63}$$

This completes the proof. □

Corollary 3. *For the DP-PSC strategy, full diversity order is achieved for both user R and user T, i.e.,*

$$d^R = d^T = M + 1. \tag{3.64}$$

Proof. The right-hand side of (3.62) is a multiplication of $M+1$ terms. According to the system model, $|h_d^\chi|$ is Rician distributed with shape prameter K_d and scale parameter $\Omega_d = \mathbb{E}[|h_d^\chi|^2]$. Since in the high transmit power regime, i.e., $P_{BS} \to \infty$, the outage probability is determined by the PDF of $|h_d^\chi|$ near zero. So, we consider the Taylor expansion of the PDF near the origin: $f_{|h_d^\chi|}(x) = \frac{2(K_d^\chi+1)}{\Omega_d}x + o(x)$. Therefore, we have the following result:

$$\Pr\left\{|h_d^\chi| \leq \sqrt{\frac{\tau_\chi}{P_{BS}}}\right\} = \int_0^{\sqrt{\frac{\tau_\chi}{P_{BS}}}} f_{|h_d^\chi|}(x)dx \approx \frac{2}{\Omega_h}(K_d^\chi+1)\frac{\tau_\chi}{P_{BS}}. \tag{3.65}$$

The remaining terms in (3.62), i.e., $\Pr\left\{|g_m||h_m^\chi| \leq \sqrt{\frac{\tau_\chi}{P_{BS}}}\right\}$ can be evaluated in a similar manner. Thus, we obtain for $P_{out}^\chi(\tau_\chi)$ the following expression:

$$P_{out}^\chi(\tau_\chi) \sim (P_{BS})^{-(M+1)}. \tag{3.66}$$

Based on the definition of the diversity order given in (3.33), we conclude that the full diversity order $M+1$ is achieved for both users. □

3.8.3.2 Power Scaling Law

As can be observed from Fig. 3.6(b), the DP-PSC strategy is symmetric for the two users. As a result, similar power scaling laws apply for both users. For simplicity, we

consider the scenario, where M is large and the power carried by the direct channel is negligible. For the end-to-end channel given in (3.58), we obtain the following theorem.

Theorem 4. *For the DP-PSC strategy, the power scaling laws for both users can be expressed as follows:*

$$P_r^{\chi} \propto \frac{8}{\pi^2} M^2 (\mu_h^{\chi} |g| \beta^{\chi})^2 + \left(1 - \frac{2}{\pi}\right) M \sigma_h^{\chi} |g|^2 (\beta^{\chi})^2. \tag{3.67}$$

Proof. The received power can be expressed as $P_r^{\chi} = \mathbb{E}[|H^{\chi}|^2]$. Furthermore, by substituting $\Delta^{\chi} = \pi/2$ in the proof process given in Appendix A.2, the approximate PDF of $|H^{\chi}|$ is obtained as:

$$f_{|H^{\chi}|}(x) = \frac{x}{\beta^2} e^{-\frac{x^2+\alpha^2}{2\beta^2}} I_0\left(\frac{x\alpha}{\beta}\right), \tag{3.68}$$

where

$$\alpha = 2\sqrt{2} M \mu_h^{\chi}/\pi, \ \beta^2 = (1 - 2/\pi)\frac{M}{2}\Omega_h^{\chi}. \tag{3.69}$$

Finally, by integrating the PDF obtained in (3.68), the proof is completed. □

Remark 4. *Similar to the PS-PSC strategy, the average received power under the DP-PSC strategy also scales with M^2 in the large M regime. However, under the same channel conditions and using equal power splitting, i.e., $\beta^R = \beta^T$, comparing the average power received by the primary user and secondary user for the PS-PSC strategy, $P_{PS\text{-}PSC}^{primary}$ and $P_{PS\text{-}PSC}^{secondary}$, respectively, and the average power received by the users for the DP-PSC strategy, $P_{DP\text{-}PSC}$, we have:*

$$P_{PS\text{-}PSC}^{primary} > P_{DP\text{-}PSC} > P_{PS\text{-}PSC}^{secondary}. \tag{3.70}$$

3.8.4 TR-PSC Strategy

For the TR-PSC strategy, the STAR-RIS is equivalent to a composite smart surface containing a reflecting-only RIS with M_R elements and a transmitting-only RIS with M_T elements, where $M_R + M_T = M$. As a result, for each reflecting-only/transmitting-only element, the phase shift of the reflection/transmission coefficient can be configured without taking into account the correlation in (3.16). As cophasing can be achieved on both sides, the end-to-end channel for user χ is given by

$$H^{\chi} = \sum_{m'=1}^{M_{\chi}} |g_{m'}||h_{m'}^{\chi}| + h_d^{\chi}. \tag{3.71}$$

3.8.4.1 Outage Probability

Considering (3.71), the end-to-end channel is the sum of the amplitudes of the cascaded channels $|g_{m'}||h_{m'}^{\chi}|$, which are perfectly aligned in phase. Thus, this expression is in a similar form as the end-to-end channel of the primary user for the PS-PSC strategy.

Theorem 5. *For the TR-PSC strategy, the asymptotic outage probability for both users can be expressed as follows:*

$$\begin{aligned} P_{out}^{\chi}(\tau_{\chi}) = &\frac{2^{M_{\chi}+1}(K_h^R+1)^{M_{\chi}}(K_d^R+1)}{(2M_{\chi}+2)!\ (\Omega_h^R)^{M_{\chi}}\Omega_d^R}(\beta^R)^{-M_{\chi}/2} \\ &\cdot e^{-M_{\chi}K_s-K_d}(\tau_{\chi})^{M_{\chi}+1}P_{BS}^{-(M_{\chi}+1)}, \end{aligned} \tag{3.72}$$

where $\tau_{\chi} = \tau_{\chi}^{NOMA}$ for NOMA and $\tau_{\chi} = \tau_{\chi}^{OMA}$ for OMA.

Proof. The proof of this theorem is similar to that of **Theorem 1**, and is omitted here for brevity. □

According to (3.72), for the TR-PSC strategy, the diversity orders are given by

$$d^R = M_R + 1 \ \text{ and } \ d^T = M_T + 1. \tag{3.73}$$

3.8.4.2 Power Scaling Law

By comparing the PSC of the TR-PSC strategy in (3.29) and (3.30) with the configuration in (3.26), we observe that the power scaling laws of the TR-PSC strategy can be deduced from **Theorem 2**.

Corollary 4. *For the TR-PSC strategy, the power scaling law for both users can be expressed as follows:*

$$\begin{aligned} P_r^{\chi} \propto & M_{\chi}^2 \cdot (\mu_h^{\chi}|g|\beta^{\chi})^2 \\ & + M_{\chi} \cdot \left\{ \sigma_h^{\chi}|g|^2(\beta^{\chi})^2 + 2\mu_h^{\chi}|g|\beta^{\chi}\mathbb{E}[|h_d^R|] \right\} + \mathbb{E}[|h_d^R|^2]. \end{aligned} \tag{3.74}$$

Proof. The proof of this corollary is similar to the proof of **Theorem 2**, and is omitted for brevity. □

Remark 5. ***Corollary 4*** *provides an important insight regarding the differences between the power scaling laws for the DP-PSC and TR-PSC strategies. For a STAR-RIS with a total of M elements, in the large M regime, the received power for DP-PSC scales with M^2 on both sides of the surface while TR-PSC can only produce powers that scale with respectively M_R^2 and M_T^2 on the two sides of the STAR-RIS. Furthermore, since $M_R, M_T \leq M$, the power differences between the two strategies are more pronounced for large numbers of elements.*

3.8.5 Performance Lower and Upper Bounds

To have performance baselines for the proposed PSC strategies for STAR-RIS-aided communication systems, we proposed lower and upper bounds.

For the performance lower bound, we assume that the STAR-RIS employs a random PSC strategy. For the performance upper bound, the STAR-RIS is assumed to be able to perform independent phase-shift adjustments for both the transmitted and reflected signals, as was done in [1, 24, 53]. The end-to-end channel gain and the achievable rate of

the primary user for the PS-PSC strategy achieve this performance upper bound. This is because for the primary user, the STAR-RIS phase-shift coefficients are chosen without considering the phase correlation constraint. Thus, by designating user R or user T as the primary user in (3.42) and (3.53), the diversity order and power scaling law of the proposed performance upper bound is obtained. Consequently, in the following, we focus on the analysis of the proposed performance lower bound.

3.8.5.1 Outage Probability

For the random PSC strategy, we assume that for all m, the phase-shifts of the reflection coefficients are randomly chosen, i.e., ϕ_m^R is uniformly distributed within $[0, 2\pi)$. The overall end-to-end channel between the BS and user χ is given by

$$H^{\chi} = |g|\beta^{\chi} \sum_{m=1}^{M} |h_m^{\chi}| \exp\{j(\angle g_m + \angle h_m^{\chi} + \phi_m^{\chi})\} + h_d^{\chi}. \tag{3.75}$$

Moreover, due to the randomness of the STAR-RIS phase shifts, ϕ_m^{χ}, the entire phase term in (3.75) can be regarded as a uniformly distributed random variable, which leads to the following theorem. For convenience, we denote the first term in (3.75) as h_s^{χ}, and thus the overall channel is given by $H^{\chi} = h_s^{\chi} + h_d^{\chi}$.

Theorem 6. *For the random PSC strategy, if the number of STAR-RIS elements is large, $|h_s^{\chi}|$ can be approximated by the following PDF:*

$$f_{|h_s^{\chi}|}(x) = \frac{2x}{\Omega_r^{\chi}} e^{-\frac{x^2}{\Omega_r^{\chi}}}, \tag{3.76}$$

where $\Omega_r^{\chi} = M|g|^2(\beta^{\chi})^2\Omega_h^{\chi}$.

Proof. We consider the real (inphase) and imaginary (quadratic) parts of h_s^{χ}:

$$T_c = |g|\beta^{\chi} \sum |h_m^{\chi}| \cos(\angle g_m + \angle h_m^{\chi} + \phi_m^{\chi}), \tag{3.77}$$

$$T_s = |g|\beta^{\chi} \sum |h_m^{\chi}| \sin(\angle g_m + \angle h_m^{\chi} + \phi_m^{\chi}). \tag{3.78}$$

According to the central limit theorem (CLT), for large M, the distributions of T_c and T_s can be approximated by Gaussian distributions with zero means and variances $\mathbb{E}[T_c^2] = \mathbb{E}[T_s^2] = M|g|^2(\beta^\chi)^2\Omega_h^\chi/2$. Thus, $|h_s^\chi| = \sqrt{T_c^2 + T_s^2}$ follows a Rayleigh distribution with the PDF given in (3.76). □

For the considered system, the outage probability of user χ can be analyzed as follows:

$$\begin{aligned} P_{out}^\chi(\gamma_0^\chi) &= \Pr\left\{\frac{(|h_s^\chi|^2 + |h_d^\chi|^2)c_\chi^2 P_{BS}}{\sigma_0^2} < \gamma_0^\chi\right\} \\ &\leq \Pr\left\{|h_s^\chi|^2 < \frac{\tau_\chi}{P_{BS}}\right\} \cdot \Pr\left\{|h_d^\chi|^2 < \frac{\tau_\chi}{P_{BS}}\right\} \\ &= \left(1 - e^{-\frac{\tau_\chi}{\Omega_r^\chi P_{BS}}}\right) \cdot \left(1 - Q(\sqrt{2K_d^\chi}, \sqrt{\frac{2\tau_\chi(K_d^\chi+1)}{\Omega_d^\chi P_{BS}}})\right), \end{aligned} \tag{3.79}$$

Next, we consider the diversity orders of users under random PSC strategy. Due to the presence of a direct link and a STAR-RIS cascaded link, the overall channel should have a diversity order of two. Indeed, if we perform the first order Taylor expansion of the outage probability derived in (3.79), each term in $\left(1 - e^{-\frac{\tau_\chi}{\Omega_r^\chi P_{BS}}}\right)$ and $\left(1 - Q(\sqrt{2K_d^\chi}, \sqrt{\frac{2\tau_\chi(K_d^\chi+1)}{\Omega_d^\chi P_{BS}}})\right)$ contributes to one P_{BS}^{-1} factor. Thus, after multiplication and using the definition given in (3.33), we have the following:

$$d_{\text{random}}^R = d_{\text{random}}^T = 2. \tag{3.80}$$

3.8.5.2 Power Scaling Law

Considering the PDF of h_s^χ given in (3.76), we have $\mathbb{E}[|h_s^\chi|] = \Omega_r^\chi = M|g|^2(\beta^\chi)^2\Omega_h^\chi$. Then, the power scaling law for the random PSC strategy is given by

$$P_r^\chi \propto \mathbb{E}[|h_s^\chi|^2] + \mathbb{E}[|h_d^\chi|^2] = M|g|^2(\beta^\chi)^2\Omega_h^\chi + \mathbb{E}[|h_d^\chi|^2]. \tag{3.81}$$

Note that the result in (3.81) scales linearly with M. Thus, compared to the three proposed PSC strategies, the average power received for the users increase significantly

STAR-RIS phase-shift strategy	PS-PSC	DP-PSC	TR-PSC	Random PSC
Diversity order of user R	$M+1$	$M+1$	M_R+1	2
Diversity order of user T	$(M+3)/2$	$M+1$	M_T+1	2
Power scaling law	$\propto M^2$	$\propto M^2$	$\propto M_\chi^2$	$\propto M$

Table 3-B: Comparing different PSC strategies.

slower with M for the random PSC strategy.

3.8.6 Summary and Discussion

The main results of this section are summarized in Table 3-B[6]. It can be observed that the PS-PSC strategy is suitable for creating asymmetric channel gains while the diversity preserving strategy is suitable for balancing the performances of both users. Moreover, Table 3-B reveals that the DP-PSC strategy provides the best performance in terms of diversity gain and power scaling.

3.9 Numerical Results

In this section, simulation results are provided to verify the performance of the proposed PSC strategies for STAR-RISs. We first present the radiation pattern for a STAR-RIS under independent phase-shift model and compare it to the conventional reflecting-only and transmitting-only RISs.

3.9.1 Radiation Pattern for Independent Phase-Shift STAR-RIS

The geographical setup is shown in Fig. 3.8(a), where the RIS is positioned at the origin in the $z=0$ plane. We simulate a 16×16 STAR-RIS, where the spacing of each element is chosen as $\lambda/2$, and a conventional RIS with $M_t = M_r = 128$. Tx sends information to *receiver* T and *receiver* R with equal power allocation, i.e., $\alpha^T = \alpha^R = 1/\sqrt{2}$. Note that in this simulation, we only consider narrowband communication so that the *beam split* effect is not strong [57].

In Fig. 3.8, we compare the coverage of the proposed STAR-RIS with conventional

[6] In this table, user R is assumed to be the primary user for the PS-PSC strategy.

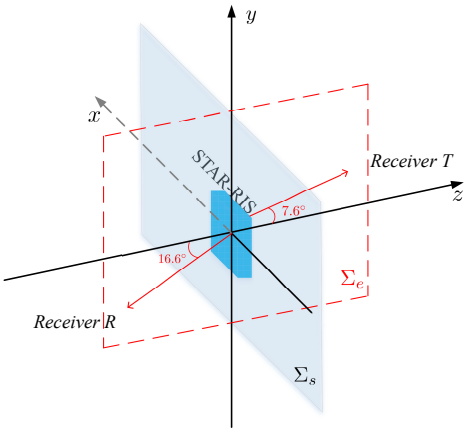

(a) Simulation setup

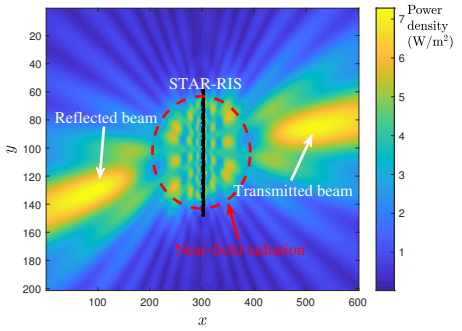

(b) STAR-RIS

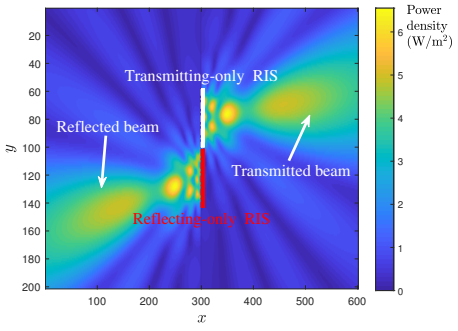

(c) Conventional RIS

Figure 3.8: Illustration of the simulation setup and simulated radiation coverage observed on plane Σ_e.

RIS by simulating their radiation patterns. The simulation is carried out as follows: Based on (3.6), we calculate the channel gain of each point on the plane Σ_e. For STAR-RIS, we set $\beta^T = \beta^R = 1/2$. The phase shift configurations of both the STAR-RIS and conventional RIS is chosen according to the cophase condition [39]. Specifically, the target angles of the transmitted signal and the reflected signal are set as 7.6° and 16.6°, respectively. As illustrated in Fig. 3.8(b), the power density of the STAR-RIS is significantly higher near the target angles, forming a beam-like radiation pattern. In contrast, in Fig. 3.8(c), the transmitted and reflected beams of the conventional RIS are less focused with weaker channel gains. Moreover, it can be observed that the angular distribution of power density has an irregular pattern which highly depends on the

distance in the near-field region, while in the far-field region, a fixed radiation pattern can be observed. These observations of the radiation patterns are consistent with the results of the two proposed channel models.

3.9.2 Beam Patterns of Different PSC Strategies

For our following simulations, we assume that the STAR-RIS is a uniform planar array consisting of $M = M_h \times M_v$ elements, where M_h and M_v denote the number of elements along the horizontal and vertical directions, respectively. The spacing between adjacent elements is half of the carrier wavelength. For the simulation in Fig. 3.9, we assume that two users are located at angular positions of 0° and 150° with equal distances of 10 m from the STAR-RIS, while the BS is located at an angular position of 270°, with a distance of 50 m from the STAR-RIS. For the PS-PSC and DP-PSC strategies, the amplitudes of the T&R coefficients of all elements are set to $\beta^T = \beta^R = 1/\sqrt{2}$. For the TR-PSC strategy, we assume that $M_R = M_T = M/2$. For the random PSC strategy, both the T&R phase shifts of each element are randomly generated within $[0, 2\pi)$.

In Fig. 3.9, we compare the angular patterns of the proposed PSC strategies and the baseline random PSC strategy. Here, we consider a STAR-RIS with 18×18 elements. As can be seen from Fig. 3.9(a), for the PS-PSC strategy, the reflected beam for the primary user (i.e., user R in the direction of 150°) has a larger power gain than the transmitted beam for the secondary user. Moreover, at the transmission side of the STAR-RIS (angular direction ranges of $(270^\circ, 360^\circ)$ and $[0^\circ, 90^\circ)$), considerable side lobes are caused by power leakage. This is expected since for the PS-PSC strategy, the phase shifts of the elements cannot be perfectly aligned for the secondary user, i.e., user T. In Fig. 3.9(b), for the DP-PSC strategy, the reflected and transmitted beams exhibit similar power levels. However, different from the reflected beam of the primary user for the PS-PSC strategy in Fig. 3.9(a), the two beams for the PS-PSC strategy have noisy edges. In Fig. 3.9(c), both the reflected and transmitted beams for the TR-PSC strategy exhibit only small side lobes. However, compared to the DP-PSC strategy, the

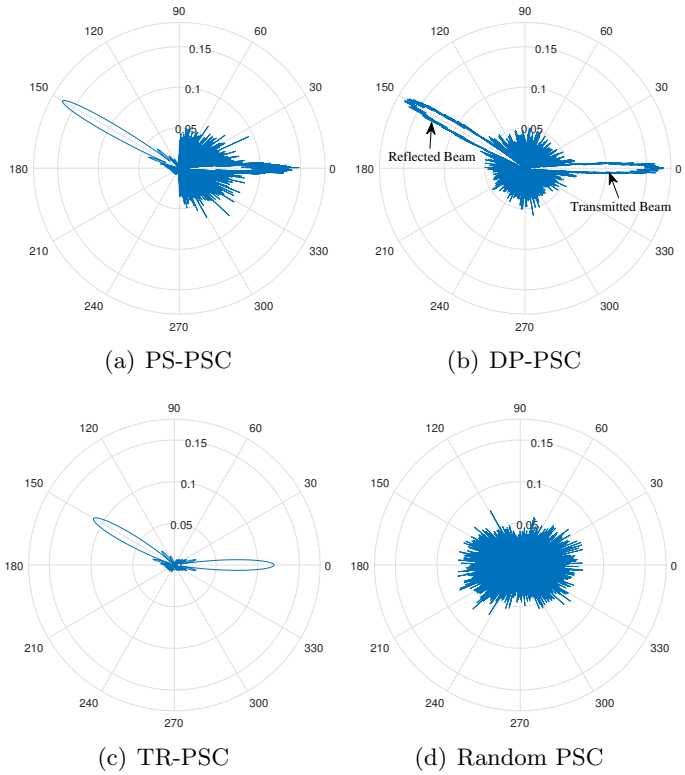

(a) PS-PSC (b) DP-PSC

(c) TR-PSC (d) Random PSC

Figure 3.9: Radiation patterns of STAR-RIS for different PSC strategies.

beam gain of the TR-PSC strategy is smaller since only part of elements are operated in the full reflection/transmission mode, which reduces the spatial diversity, see (3.73). For the baseline random PSC strategy, in Fig. 3.9(d), no dedicated target beams can be observed, and the signal power is distributed over the entire space. The above results confirm the importance of employing suitable PSC strategies for STAR-RISs.

Remark 6. *The results shown in Fig. 3.9(a)-(c) highlight an interesting trade-off between the power of the desired signal and the power of undesired interference. Specifically, although the beam gain for the DP-PSC strategy is larger than that for the TR-PSC strategy, DP-PSC also imposes more power leakage in non-intended directions leading to significant interference. For the TR-PSC strategy, the beam gain in the target direction is sacrificed but almost no interference in other directions is caused. It is worth noting that in practice, having cleaner main beams with fewer side lobes may be extremely beneficial especially for multi-user systems. Based on this observation, selecting the optimal*

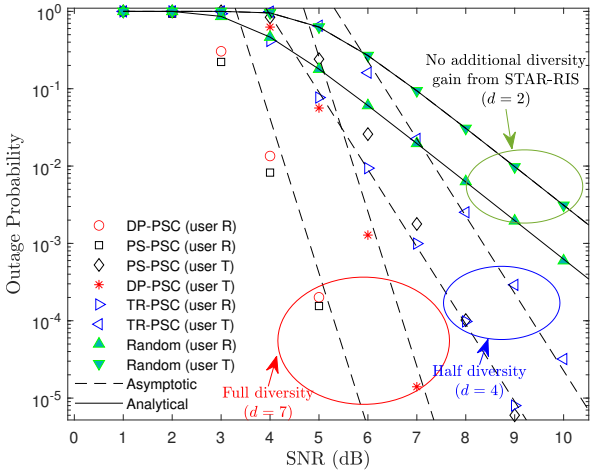

Figure 3.10: Outage probabilities for OMA users employing different PSC strategies.

PSC strategy for specific application scenarios constitutes an interesting topic for further investigation.

3.9.3 Outage Probability and Diversity Order

For the following simulation results, we assume all STAR-RIS-user channels are modeled as Rician fading channels with path loss exponent $\alpha = 2.2$ and Rician factor $K = 1.3$ dB. The noise power for both users is set to $\sigma_0^2 = -50$ dBm. We also assume that the scale factor for user R is twice as the scale factor of user T. Thus, the average received power of user R is larger. The transmit SNR (P_{BS}/σ_0^2) was varied between 0 dB and 12 dB. We consider an asymmetric channel by setting the expected power of the T&R channels as $\mathbb{E}[|h_m^R|^2] = 2\mathbb{E}[|h_m^T|^2]$. The target data rate for both users is set at $\tilde{R} = 1.5$ bit/s/Hz. In Fig. 3.10, we present simulation results for the outage probabilities of both users for the proposed PSC strategies and the baseline random PSC strategy. To verify our performance analysis, asymptotic results are presented for the proposed PSC strategies exploiting (3.41) and (3.72), while analytical results are presented for the random PSC strategy exploiting (3.79).

As can be observed, the primary user for the PS-PSC strategy achieves the lowest

outage probability and full diversity order, since the STAR-RIS can align the reflected channels with the direct channel for the primary user. However, due to the correlated T&R phase-shift model, the secondary user suffers a noticeable performance loss as the available choices for the transmission phase shifts are limited. Moreover, it can be observed that the primary user and the secondary user achieve full diversity order and reduced diversity order, respectively, which is consistent with (3.42) and (3.45). For the DP-PSC strategy, as can be seen from Fig. 3.10, the outage probabilities of both users exhibit similar slopes and can achieve full diversity order, which is consistent with (3.64). In addition, user R still has a lower outage probability than user T. This is be cause user R has a higher channel gain due to its shorter path-length. For the TR-PSC strategy, since only half of the STAR-RIS elements are used for transmission/reflection (i.e., reduced array gain), there is a considerable performance loss for both users and only half of the maximum diversity order can be achieved, as is expected from (3.73). Furthermore, the random PSC strategy yields the worst performance and achieves no additional diversity gain, which is in accordance with (3.80).

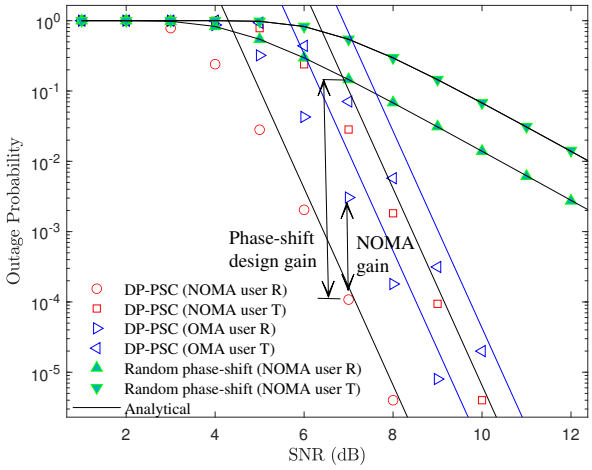

Figure 3.11: Outage probabilities for NOMA and OMA users for the DP-PSC strategy.

In Fig. 3.11, we compare the outage probabilities of the users for NOMA and OMA. The STAR-RIS is assumed to employ the DP-PSC strategy. The power allocation factors

for the two users are set to $c_R^2 = 0.4$ and $c_T^2 = 0.6$. As can be observed, for both users, NOMA yields a better outage performance than OMA. Moreover, comparing the DP-PSC strategy with the random PSC strategy, it can be observed that the performance gap between the two PSC strategies (illustrated with the vertical double arrow) increases with the transmit SNR. In contrast, the performance gain of NOMA over OMA in terms of outage probability stays constant in the high SNR regime, which is consistent with (3.59).

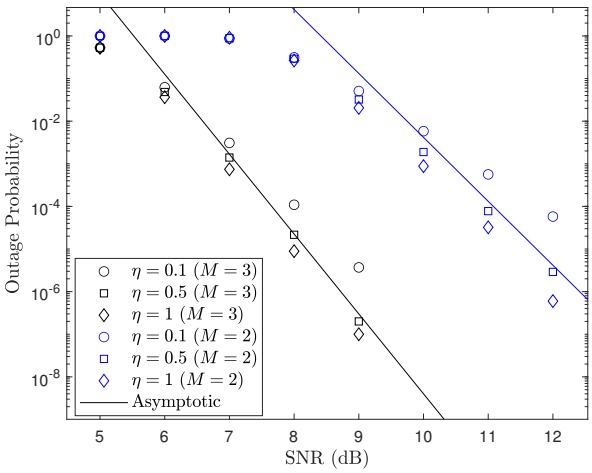

Figure 3.12: Outage probabilities for diversity preserving strategy with different strengths of direct links.

3.9.4 Effect of Direct Links with Different Strengths

In (3.64), we have shown that with the presence of the direct BS-user links, the diversity orders of both the users for the DP-PSC strategy are $M + 1$. In this simulation, we investigate the effects of the direct link strength on the outage probabilities and diversity orders of the users. Fig. 3.12 shows the outage probability for the DP-PSC strategy with different direct link strengths. In the legend, $\eta = \mathbb{E}[|h_d|/|h_m^X|]$ denote the power ratio between the expected strength of the direct link and the links through STAR-RIS elements. When $\eta = 0.1$, the direct link is almost negligible. As shown in the figure, the corresponding simulated outage probabilities (plotted with circles) exceed the asymptotic line, meaning that full diversity order is not achieved within the chosen

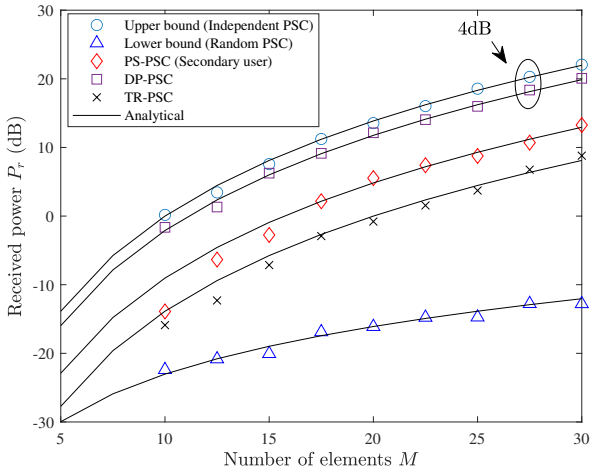

Figure 3.13: Power scaling laws of users for different PSC strategies.

SNR range. However, for $\eta = 0.5$ and $\eta = 1$, it can be observed that full diversity can be achieved despite the change in the strength of the direct link. This observation is consistent with the analytical result derived in (3.64).

3.9.5 Power Scaling Laws

In Fig. 3.13, we investigate the power scaling laws of the proposed PSC strategies. The figure shows the received power in dB (for a reference value of 50 dBm) versus the number of STAR-RIS elements. For comparison, we also show results for STAR-RIS with the independent phase-shift model and the random PSC strategy, which provide performance upper and lower bounds, respectively. As can be observed, by doubling M from 15 to 30, the received powers for the DP-PSC and PS-PSC strategies increase by about 10 dB, while the power for the random PSC strategy increases only by about 5 dB. This is due to their different power scaling laws (M^2 versus M), see (3.56), (3.67), and (3.81). Moreover, the received power for the DP-PSC strategy is only 4 dB below the upper bound for large numbers of elements. This result can be deduced by comparing (3.53) and (3.67) since $10\log_{10}(4/\pi^2) \approx -3.9$ dB.

3.10 Summary

In this chapter, independent and correlated T&R phase-shift models for STAR-RISs was proposed. Furthermore, considering a STAR-RIS-aided two-user communication system employing OMA and NOMA, three practical PSC strategies were introduced. To evaluate and compare the performance achieved with different STAR-RIS PSC strategies, the asymptotic behavior of the outage probabilities for both OMA and NOMA were derived. Moreover, the diversity orders and the power scaling laws for the considered PSC strategies were investigated.

However, our primary focus of this chapter has been on passive STAR-RISs for downlink transmission, and the scenario where wireless signals incident on both sides of the surface simultaneously is not studied. This is particularly relevant for the uplink communication, where multiple users surrounding the STAR-RIS need to upload their information to the base station (BS). Additionally, both RISs and STAR-RISs suffer from the "double-fading" effect, where the small-scale fading of the BS-RIS link and the RIS-receiver link are multiplied, leading to significant signal degradation. In the next chapter, we address these two key challenges by studying dual-sided STAR-RISs and active STAR-RISs.

Chapter 4

Dual-Sided STAR-RISs and Active STAR-RISs

In this chapter we study two STAR-RIS variants: the dual-sided STAR-RIS and the active STAR-RIS. We separately study these two types of STAR-RISs because they have distinct characteristics and the basic models proposed for STAR-RIS in Chapter 3 do not apply for them. The rest of this chapter is organized as follows. In Section 4.1, the modeling and analysis for dual-sided STAR-RISs are presented. In Section 4.2, a hardware model for active STAR-RISs is proposed, which is followed by the conclusions in Section 4.3.

4.1 Dual-Sided STAR-RISs

4.1.1 EM-Based Modeling for Dual-Sided STAR-RISs

In the model proposed in Chapter 3, two complex coefficients, namely, the transmission and reflection (T&R) coefficients, are introduced to characterize the *STAR* feature of each element [24]. However, these two coefficients are derived by assuming that the signals only incident from one side of the surface and there is no signal incident from

the other side. The signal model is generally unknown for the case where there are wireless signals simultaneously incident on both sides of the STAR-RIS, namely *dual-sided incidence*. To fill this knowledge gap, in this section, we provide a signal model for *dual-sided* STAR-RISs. Since the 'STAR' process occurs on each side, we introduce two pairs of coefficients in the following general signal model.

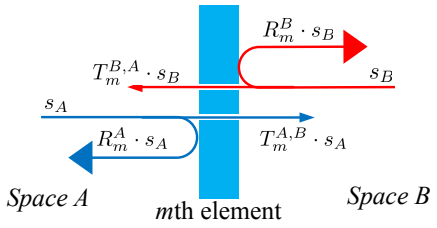

Figure 4.1: A general signal model for dual-sided STAR-RISs

Theorem 7. *As illustrated in Fig. 4.1, for vertically polarized wireless signals, the signals radiating from the mth element towards Space A (s'_A) and towards Space B (s'_B) are linear superposition of the incident signals ($s_{A/B}$):*

$$s'_A = \sum_{\theta \in \Theta_A} R_m^A(\theta) \cdot s_A(\theta) + \sum_{\theta \in \Theta_B} T_m^{B,A}(\theta) \cdot s_B(\theta), \tag{4.1}$$

$$s'_B = \sum_{\theta \in \Theta_A} T_m^{A,B}(\theta) \cdot s_A(\theta) + \sum_{\theta \in \Theta_B} R_m^B(\theta) \cdot s_B(\theta), \tag{4.2}$$

where $T_m^{A,B}(\theta)$ and $T_m^{B,A}(\theta)$ are the transmission coefficients from Space A/B to Space B/A, $R_m^{A/B}(\theta)$ is the reflection coefficient for Space A/B, subscript m denote the mth STAR element, θ is the incidence angle of the signal, and Θ_A and Θ_B are the set of angles of the incident signals from Space A and Space B, respectively.

Proof. The key for this proof is to demonstrate that the received signals are the linear superposition of the incident signals from different directions. According to [47], for STAR-RIS that is electrically thin[1], the EM response can be equivalently described

[1]Please note that although we assume that STAR-RIS elements are electrically thin, they need to have a certain width to accommodate magnetic currents (refer to Section 3.3.1 for details). Consequently, this theorem is only applicable to STAR-RIS elements that are not excessively thin but still thinner than the carrier wavelength to qualify as electrically thin. In the general case where elements are electrically large, they should be modeled using the Green's function method discussed in Chapter 5.

using surface electric and magnetic currents $\mathbf{J}_s$ and $\mathbf{K}_s$. Note that the direction of $\mathbf{K}_s$ is determined through the curl right-hand rule, which is illustrated in Fig. 4.2. Considering passive STAR-RIS elements, these currents are excited by the total EM field $\mathbf{E}_{tot}, \mathbf{H}_{tot}$, and scaled by the electric admittance ($\overline{\overline{\mathbf{Z}}}_{\mathrm{e}}$) and magnetic impedance ($\overline{\overline{\mathbf{Z}}}_{\mathrm{m}}$) tensors at each element, i.e., $\mathbf{J}_s = \overline{\overline{\mathbf{Z}}}_{\mathrm{e}} \cdot \mathbf{E}_{tot}$ and $\mathbf{K}_s = \overline{\overline{\mathbf{Z}}}_{\mathrm{m}} \cdot \mathbf{H}_{tot}$. As illustrated in Fig. 4.2, the electric current density $\mathbf{J}_s$ generates fields $\mathbf{E}^J$, $\mathbf{H}_1^J$, and $\mathbf{H}_2^J$ while the magnetic current density $\mathbf{K}_s$ generates fields $\mathbf{E}_1^K$, $\mathbf{E}_2^K$, and $\mathbf{H}^K$. The magnitude of the radiating field, $\mathbf{E}^J$ and $\mathbf{E}^K$, are proportional to the strength of $\mathbf{J}_s$ and $\mathbf{K}_s$. Thus, for signals with the same polarization, the received field can be expressed as the linear combination of the incident fields $\mathbf{E}_1^{inc}$ and $\mathbf{E}_2^{inc}$. Finally, by using the fact that the signal $s_{A/B}$ is the proportional to the magnitude of the corresponding electric field, i.e., $s_{A/B} = ||\mathbf{E}_{A/B}^{inc}||_2$, the theorem is derived. □

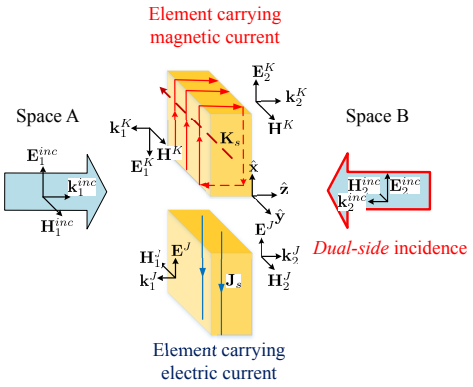

Figure 4.2: Schematic of the STAR-RIS element under EM wave incidence.

4.1.1.1 A Hardware Model for Symmetrical Dual-Sided STAR-RISs

For a general scenario, the T&R coefficients for the two sides can be different, i.e., $T_m^{A,B} \neq T_m^{B,A}$ and $R_m^A \neq R_m^B$. However, for the case where the surface impedances can be characterized with scalars [47], the elements have symmetrical EM response for the two directions, i.e., $T_m^{A,B} = T_m^{B,A}$ and $R_m^A = R_m^B$. Following the method adopted in Chapter 3, we separately study the radiation of electric and magnetic currents[2]. The

[2]Here, the magnetic current refers to the equivalent magnetic current generated by the vortex currents [11].

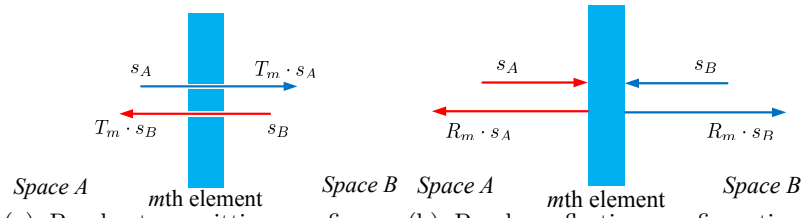

(a) Purely transmitting configuration (connecting *Space A/B*)

(b) Purely reflecting configuration (separating *Space A/B*)

Figure 4.3: Signal model for purely transmitting and purely reflecting.

schematic illustration of the STAR-RIS under EM incidence on both sides is presented in Fig. 4.2. In *Space A/B*, the total electrical radiation comes from the contributions of these induced electric fields and the overall incident fields $\mathbf{E}_1^{inc}$ and $\mathbf{E}_2^{inc}$. The strengths of the surface electric and magnetic currents are proportional to the sum of the incident and radiated fields at the STAR-RIS [50]. Thus, the density of the electric and magnetic currents are respectively given by:

$$\mathbf{J}_s = (\mathbf{E}_1^{inc} + \mathbf{E}_2^{inc} + \mathbf{E}^J)/(Z_\mathrm{e})_m, \tag{4.3}$$

$$\mathbf{K}_s = (\mathbf{H}_1^{inc} - \mathbf{H}_2^{inc} + \mathbf{H}^K)(Z_\mathrm{m})_m, \tag{4.4}$$

where $(Z_\mathrm{e})_m$ and $(Z_\mathrm{m})_m$ are the scalar electric and magnetic impedance of the mth element, respectively. To solve the generated electric fields $\mathbf{E}^J$ and $\mathbf{E}^K$, we consider the following boundary conditions. The boundary conditions [10] of EM field at the surface can be expressed as $\hat{z} \times (\mathbf{H}_2^J - \mathbf{H}_1^J)\hat{y} = \mathbf{J}_s\hat{x}$ and $\hat{z} \times (\mathbf{E}_1^K - \mathbf{E}_2^K)\hat{x} = \mathbf{K}_s\hat{y}$. Thus, we can obtain the following:

$$\mathbf{E}^J = -\frac{\eta(\mathbf{E}_1^{inc} + \mathbf{E}_2^{inc})}{2(Z_\mathrm{e})_m + \eta}, \tag{4.5}$$

$$\mathbf{E}_1^K = -\mathbf{E}_2^K = \frac{(Z_\mathrm{m})_m(\mathbf{E}_1^{inc} - \mathbf{E}_2^{inc})}{(Z_\mathrm{m})_m + 2\eta}, \tag{4.6}$$

where η is the free space wave impedance.

For a receiver located in *Space A/B*, the received signal strength is proportional to the square of the overall received electric field. As illustrated in Fig. 4.2, for *Space A*,

we collect all the wave vectors going towards the left, i.e., $\mathbf{k}_2^{inc}$, $\mathbf{k}_1^J$, and $\mathbf{k}_1^K$. Thus, the overall electric field propagating towards *Space A/B* through the mth STAR element can be calculated as follows:

$$\begin{aligned}\mathbf{E}_A^{rec} = \mathbf{E}^J + \mathbf{E}_1^K + \mathbf{E}_2^{inc} = &\underbrace{\left(\frac{(Z_{\mathrm{m}})_m}{(Z_{\mathrm{m}})_m + 2\eta} - \frac{\eta}{2(Z_{\mathrm{e}})_m + \eta}\right)}_{R_m} \mathbf{E}_1^{inc} \\ &+ \underbrace{\left(\frac{2(Z_{\mathrm{e}})_m}{2(Z_{\mathrm{e}})_m + \eta} - \frac{(Z_{\mathrm{m}})_m}{(Z_{\mathrm{m}})_m + 2\eta}\right)}_{T_m} \mathbf{E}_2^{inc}.\end{aligned} \tag{4.7}$$

Similarly, the overall electric field propagating towards *Space B* is as follows:

$$\begin{aligned}\mathbf{E}_B^{rec} = \mathbf{E}^J + \mathbf{E}_2^K + \mathbf{E}_1^{inc} = &\underbrace{\left(\frac{2(Z_{\mathrm{e}})_m}{2(Z_{\mathrm{e}})_m + \eta} - \frac{(Z_{\mathrm{m}})_m}{(Z_{\mathrm{m}})_m + 2\eta}\right)}_{T_m} \mathbf{E}_1^{inc} \\ &+ \underbrace{\left(\frac{(Z_{\mathrm{m}})_m}{(Z_{\mathrm{m}})_m + 2\eta} - \frac{\eta}{2(Z_{\mathrm{e}})_m + \eta}\right)}_{R_m} \mathbf{E}_2^{inc}.\end{aligned} \tag{4.8}$$

Next, exploiting (4.7) and (4.8), the signal model for dual-sided STAR-RIS can be established.

4.1.1.2 Signal Modeling for Symmetrical Dual-Sided STAR-RIS Elements

According to (4.7) and (4.8), we have the following theorem.

Theorem 8. *For symmetrical dual-sided STAR-RISs, the signals radiating from the mth element towards Space A (s'_A) and towards Space B (s'_B) are as follows:*

$$s'_A = R_m \cdot s_A + T_m \cdot s_B, \tag{4.9}$$

$$s'_B = T_m \cdot s_A + R_m \cdot s_B, \tag{4.10}$$

where

$$T_m = \frac{2(Z_{\mathrm{e}})_m}{2(Z_{\mathrm{e}})_m + \eta} - \frac{(Z_{\mathrm{m}})_m}{(Z_{\mathrm{m}})_m + 2\eta}, \tag{4.11}$$

$$R_m = \frac{(Z_{\mathrm{m}})_m}{(Z_{\mathrm{m}})_m + 2\eta} - \frac{\eta}{2(Z_{\mathrm{e}})_m + \eta} \tag{4.12}$$

are the T&R coefficients for each STAR-RIS element.

Proof. The proof of this theorem is based on the boundary conditions and the density of the electric and magnetic currents given in (4.3) and (4.4). Exploiting these characteristics, the field in both *Space A* and *Space B* were given in (4.7) and (4.8). Then, by using the fact that the received signal $s'_{A/B}$ is the proportional to the magnitude of the received electric field, i.e., $s'_{A/B} = ||\mathbf{E}^{rec}_{A/B}||_2$, (4.7) and (4.8) can be rewritten into the forms as in (4.9) and (4.10), respectively. □

4.1.2 Performance Evaluation for A Dual-Sided STAR-RIS Uplink System

Based on the above signal model, we evaluate the performance of a dual-sided STAR-RIS-aided uplink communication system. We consider the two-user case and the use of two fundamental multiple access schemes, i.e., OMA and NOMA.

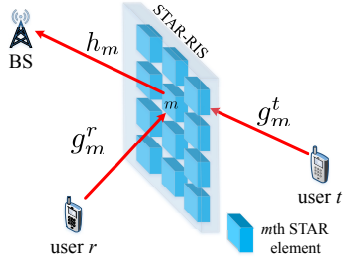

Figure 4.4: System model for the dual-sided STAR-RIS-aided uplink communication system.

4.1.2.1 System Model

We study the application scenario where a symmetrical *dual-sided* STAR-RIS is deployed to assist the uplink communication. To reveal the fundamental performance limit and to obtain closed-form results, we consider a two-user setup. We term the user which uploads the information via the reflection link as user r and the user which uploads the information via the transmission link as user t. The direct link between the users and BS are assumed to be blocked. The STAR-RIS has M elements whose complex-valued T&R coefficients are given according to (4.11) and (4.12). For convenience, in the following, we rewrite these coefficients in terms of their amplitudes and phase-shift arguments, i.e., $T_m = \beta_m^T e^{j\phi_m^T}$ and $R_m = \beta_m^R e^{j\phi_m^R}$, $m \in \{1, 2, \cdots, M\}$. The links between the mth STAR-RIS element and the BS, h_m, is assumed to follow a Rician distribution, i.e., $|h_m| \sim \mathcal{R}(K_h, \Omega_h)$, where K_h and Ω_h are the shape and scale parameters of the Rician distribution. The links between the mth STAR-RIS element and the users[3], g_m^t and g_m^r, also follow Rician distributions, i.e., $|g_m^\chi| \sim \mathcal{R}(K_g^\chi, \Omega_g^\chi)$, where the notation $\chi \in \{t, r\}$ is an indicator representing the corresponding values for user t or user r. For the multiple access schemes, we first consider NOMA and then conventional OMA as a baseline.

4.1.2.2 NOMA

In NOMA, the two users upload their information to the BS via the same time/frequency resource blocks. The channel conditions of users depend on the choice of T_m and R_m. According to the proposed signal model, the signal received at BS can be expressed as follows:

$$y = \sum_{m=1}^{M} g_m^r h_m \beta_m^R e^{j\phi_m^R} \sqrt{p} s_r + \sum_{m=1}^{M} g_m^t h_m \beta_m^T e^{j\phi_m^T} \sqrt{p} s_t + n_0, \tag{4.13}$$

where s_r and s_t are the message of user r and user t, respectively, p is the transmit power of the uplink users, and n_0 is the additive white Gaussian noise at the BS with variance σ_0^2. Without loss of generality, we assume user r is closer to the STAR-RIS and has a higher channel gain than user t. At the BS, the signal of user r is decoded

[3]Note that g_m^r and g_m^t are two independent channels.

first by treating the other signal as interfering noise, and the corresponding signal-to-interference-plus-noise ratio (SINR) is given by:

$$\mathrm{SINR}_r = \frac{p\left|\sum_{m=1}^{M} g_m^r h_m \beta_m^R e^{j\phi_m^R}\right|^2}{p\left|\sum_{m=1}^{M} g_m^t h_m \beta_m^T e^{j\phi_m^T}\right|^2 + \sigma_0^2}. \tag{4.14}$$

Then, the signal of user t can be decoded after carrying out successive interference cancellation (SIC). Consider imperfect SIC, only a portion of the signal from user r can be successfully cancelled. Thus, the signal of user t has the following SINR:

$$\mathrm{SINR}_t = \frac{p\left|\sum_{m=1}^{M} g_m^t h_m \beta_m^T e^{j\phi_m^T}\right|^2}{\alpha_0 \cdot p\left|\sum_{m=1}^{M} g_m^t h_m \beta_m^T e^{j\phi_m^T}\right|^2 + \sigma_0^2}, \tag{4.15}$$

where $\alpha_0 \in [0, 1]$ is the error propagation factor which characterizes the quality of the SIC, i.e., $\alpha_0 = 0$ corresponds to perfect SIC and $\alpha_0 = 1$ corresponds to the case where no cancellation is performed.

4.1.2.3 New Channel Statistics

New channel statistics can be obtained for the considered STAR-RIS-aided uplink system. Since the overall channel distribution is highly sensitive to the choice of T_m and R_m, we consider the performance achieved by configuring ϕ_m^T and ϕ_m^R according to the cophase condition [6]. Moreover, we assume that the amplitudes, β_m^T and β_m^R, are uniform across the entire STAR-RIS, i.e., $\beta_m^{T/R} = \beta^{T/R},\ \forall m \in \{1, 2, \cdots, M\}$. According to (4.14) and (4.15), under a cophasing phase shift, the overall uplink channel for the two users can be expressed as follows:

$$H_{r/t} = \sum_{m=1}^{M} \beta^{R/T} |h_m| \cdot |g_m^{r/t}|. \tag{4.16}$$

Note that $\phi_m^{R/T}$ are chosen to align the phases of each terms in the sum of (4.16). Next, we study the distribution of $|H_r|$, $|H_t|$, SINR_r, and SNR_t.

Lemma 2. *Each term in the summation of* (4.16) *is the product of two Rician variables. Let* $X_m^r = |h_m||g_m^r|$ *and* $X_m^t = |h_m||g_m^t|$*, their probability density functions (PDFs) are given as follows:*

$$\begin{aligned} f_{|X_m^\chi|}(x) &= \frac{x}{\beta_h \beta_g^\chi} e^{-(K_h + K_g^\chi)} \\ &\cdot \sum_{i=0}^{\infty} \sum_{l=0}^{\infty} \frac{\left(\frac{\alpha_h \sqrt{x}}{2\beta_h}\right)^{2i} \left(\frac{\alpha_g^\chi \sqrt{x}}{2\beta_g^\chi}\right)^{2l}}{i! l! \Gamma(i+1)\Gamma(l+1)} \left(\frac{\beta_h}{\beta_g^\chi}\right)^{\frac{i-l}{2}} K_{i-l}\left(\frac{x}{\sqrt{\beta_h \beta_g^\chi}}\right), \end{aligned} \tag{4.17}$$

where $\alpha_h^2 = \frac{K_h \Omega_h}{K_h+1}$,$(\alpha_g^\chi)^2 = \frac{K_g^\chi \Omega_g^\chi}{K_g^\chi+1}$, $\beta_h = \frac{\Omega_h}{2(K_h+1)}$, $\beta_g^\chi = \frac{\Omega_g^\chi}{2(K_g^\chi+1)}$, $\Gamma(x)$ *denotes the Gamma function, and* K_n *is the modified Bessel function of the second kind.*

Proof. The detailed proof for the PDF of the product of two Rician variables can be found in [56]. □

4.1.2.4 Outage Probability

In the considered system, the achievable rate of user r is given by $\tilde{R}_r = \log_2(1 + \mathrm{SINR_r})$ bit/s/Hz. Consider a fixed-rate transmission, the outage probability of user r is given by:

$$P_{out}^r = \Pr\{\mathrm{SINR}_r < 2^{\tilde{R}_r} - 1\}. \tag{4.18}$$

For user t, the BS needs to subtract the decoded message from user r first, then decode the remaining message, thus, the outage probability is given by:

$$P_{out}^t = 1 - \Pr\{\mathrm{SINR}_r > 2^{\tilde{R}_r} - 1, \mathrm{SNR}_t > 2^{\tilde{R}_t} - 1\}, \tag{4.19}$$

where $\tilde{R}_r$ and $\tilde{R}_t$ are the target data rate for user r and t, respectively. However, the PDF of the SINR in (4.14) is difficult to evaluate in closed-form. To reveal more practical

insights, we study the outage probabilities in the high transmit SNR regime[4].

For the high transmit SNR scenario, we assume that $p/\sigma_0^2 \gg 1$. Thus, the outage probabilities of user r can be reduced to:

$$P_{out}^{r} = \Pr\left\{ \frac{\left| \sum_{m=1}^{M} g_m^r h_m \beta_m^R e^{j\phi_m^R} \right|^2}{\left| \sum_{m=1}^{M} g_m^t h_m \beta_m^T e^{j\phi_m^T} \right|^2} < \gamma_r \right\}, \tag{4.20}$$

where $\gamma_r = 2^{\tilde{R}_r} - 1$. Considering the impact of imperfect SIC, the outage probability of user t is given as follows:

$$P_{out}^{t} = \begin{cases} \Pr\left\{ \dfrac{\left| \sum_{m=1}^{M} g_m^r h_m \beta_m^R e^{j\phi_m^R} \right|^2}{\left| \sum_{m=1}^{M} g_m^t h_m \beta_m^T e^{j\phi_m^T} \right|^2} < \gamma_r \right\}, & \text{if } \alpha_0^{-1} > 2^{\tilde{R}_t} - 1 \\ 1, & \text{otherwise.} \end{cases} \tag{4.21}$$

In the following theorem, we give the closed-form analytical result for the outage probabilities.

Theorem 9. *In the high transmit SNR regime, the outage probability is given by:*

$$P_{out} = \Phi\left(\frac{\mu^t x_0 - \mu^r}{\sigma^t \sigma^r \xi(x_0)} \right), \tag{4.22}$$

where $\Phi(y) = \int_{u=-\infty}^{y} \frac{1}{\sqrt{2\pi}} e^{-u^2/2} du$ *is the error function,* $\xi(x) = \sqrt{\frac{x^2}{(\sigma^r)^2} - \frac{2\rho x}{\sigma^r \sigma^t} + \frac{1}{(\sigma^t)^2}}$, $\rho = \mathrm{Cov}(|H_r|, |H_t|)/(\sigma^r \sigma^t)$ *is the correlation coefficient between* $|H_r|$ *and* $|H_t|$, $x_0 = \sqrt{\gamma_r}\beta^T/\beta^R$ *is the threshold for the outage probability,* $\mu^{\chi} = \frac{1}{4}\sqrt{\frac{\pi\Omega_h}{(K_h+1)}} L_{1/2}(-K_h) \sqrt{\frac{\pi\Omega_g^{\chi}}{(K_g^{\chi}+1)}} \cdot L_{1/2}(-K_g^{\chi})$ *is the expectation value of* $|h_m||g_m^{\chi}|$, *and* $(\sigma^{\chi})^2 = \Omega_h \Omega_g^{\chi} - (\mu^{\chi})^2$ *is its variance.*

Proof. According to the central limit theorem, both H_r and H_t follow the normal distribution when M is sufficiently large. In the high transmit SNR regime, the outage

[4]Here, the transmit SNR is $\gamma_{transmit} = p/\sigma_0^2$

probabilities in both (4.20) and the successful case of (4.21) are reduced to $P_{out} = \Pr\{|H_r|/|H_t| < \sqrt{\gamma_r}\}$. According to (4.16), $|H_r|$ and $|H_t|$ have common terms and we denote their correlation coefficient as ρ. According to [58], the cumulative distribution function (CDF) of the ratio between two correlated normal distributions can be expressed in terms of the error function. □

Remark 7. *An interesting observation is that uplink NOMA users have error floors for outage probability, while downlink NOMA user does not. As shown in* (4.22)*, the analytical outage probabilities do not further decrease with the increase of the uploading transmit power p, this indicates that the outage probabilities of both users approach the same error floor. This is because in uplink NOMA, where multiple users transmit simultaneously to a common receiver, power allocation schemes prioritize weaker users by assigning them higher power levels. However, this power imbalance can introduce strong interference to users with better channel conditions, leading to an error floor in the outage probability. In downlink NOMA, the use of successive interference cancellation techniques allows the receiver to decode and subtract the signals of users with stronger channels, effectively suppressing interference and avoiding an error floor.*

It's worth noting that the presence of an error floor in uplink NOMA depends on various factors such as the power allocation scheme, channel conditions, and the number of users. Advanced interference management techniques, adaptive power allocation, and improved receiver algorithms can help mitigate the error floor in uplink NOMA systems.

Remark 8. *In Theorem 9, we use a normal distribution ($f_{Gaus}(x)$) to approximate the PDF of $|H_r|$ which the exact distribution ($f_{exact}(x)$) is the sum of M cascaded Rician channels. The approximation error decreases with the increase of M. In the following table, we calculated the Kullback–Leibler divergence (relative entropy) from $f_{exact}(x)$ to $f_{Gaus}(x)$, i.e., $D_{KL} = \int_{x=-\infty}^{\infty} f_{Gaus}(x) \cdot \log\left(\frac{f_{Gaus}(x)}{f_{exact}(x)}\right)$. It can be observed that D_{KL} quickly diminishes after $M \geq 20$.*

M	5	10	15	20	25
D_{KL}	4.0877	1.4109	1.4043	7.2×10^{-3}	5.9×10^{-3}

Table 4-A: Kullback–Leibler divergence from the exact distribution to the approximated normal distribution.

4.1.2.5 OMA Baseline

In OMA, user t and r upload their messages via orthogonal time/frequency resource blocks. In terms of user outage probabilities, the outage probabilities for user r and t in OMA are given as follows:

$$P_{out}^{r/t,\mathrm{O}} = \Pr\{\mathrm{SNR}_{r/t}^{\mathrm{O}} < 2^{2\tilde{R}_{r/t}} - 1\} \tag{4.23}$$

where $\mathrm{SNR}_{r/t}^{\mathrm{O}} = p\left|\sum_{m=1}^{M} g_m^{r/t} h_m e^{j\phi_m^{R/T}}\right|^2 / \sigma_0^2$ is the SNR for OMA. The closed-form analytical outage probabilities for OMA scenario can be obtained in a similar way to those of NOMA scenario. For the clarity of presentation, we provide the results for OMA in Appendix B.

4.1.3 Numerical Results

In this section, simulation results are provided to investigate the performance of the STAR-RIS-aided uplink communication. For our simulations, we assume that the STAR-RIS is a uniform planar array consisting of M elements. The spacing between adjacent

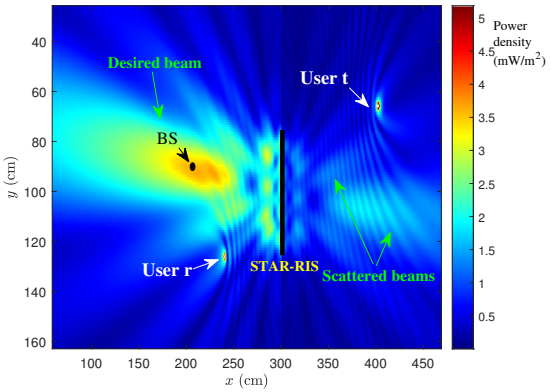

Figure 4.5: Radiation density of the STAR-RIS-aided uplink transmission.

elements is half of the carrier wavelength. All STAR-RIS-user channels are modeled as Rician fading channels with path loss exponents of $\alpha = 2.2$ and the Rician factor of $K = 1.3$ dB.

In Fig. 4.5, the power density is plotted for the considered uplink transmission where two users are located on different sides of the STAR-RIS where $M = 8 \times 8$. The transmission power of the users are set to $p = 10$ dBm. The T&R phase-shift coefficients are configured according to the cophase condition and the amplitudes are equal, i.e., $\beta^R = \beta^T = 1/\sqrt{2}$. It can be observed that the STAR-RIS significantly improves the signal strength at the location of the BS. However, there are still scattered beams on the other side of the STAR-RIS. These beams consist the signal of user r that is transmitted (leaked) through the STAR-RIS and the signal of user t that is reflected back.

In Fig. 4.6, the outage probabilities for NOMA and OMA are plotted where the target data rate for both users is set at $\tilde{R}_t = \tilde{R}_r = 1.5$ bit/s/Hz. The noise power for both users is set to $\sigma_0^2 = -50$ dBm and the transmit SNR is varied from 0 to 10 dB. Moreover, the amplitudes of the transmission coefficients of the elements are set to $\beta^T = 0.2$. By comparing the user outage probability of NOMA and OMA, it can be observed that the dual-sided STAR-RIS-aided uplink NOMA performs mostly better than STAR-RIS-aided OMA for both users. Thus, NOMA is a good candidate to exploit the STAR

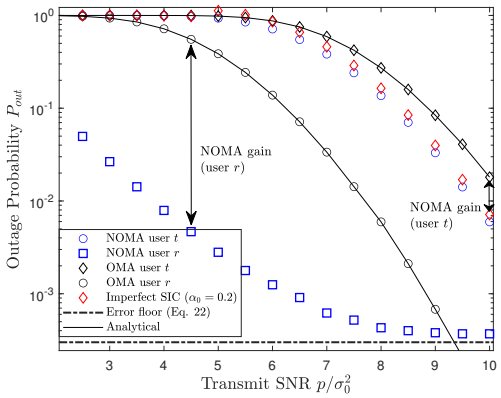

Figure 4.6: Comparing outage probabilities of OMA and NOMA with perfect/imperfect SIC.

capability of dual-sided STAR-RISs. In addition, for NOMA with imperfect SIC, the outage probability of user r is unaffected while the outage probability of user t is slightly higher than NOMA with perfect SIC. However, due to the presence of the error floor of uplink NOMA, the performance of NOMA starts to saturate when the transmit SNR is high. The dual-sided STAR-RIS is able to further lower this error floor as we will see in the next figure.

In Fig. 4.7, the outage probability error floor is plotted with the simulated outage probabilities for user t and user r employing NOMA. In this simulation, we plot the outage probability for the uniform amplitude configuration and for the mode switching (MS) configuration. For the uniform amplitude configuration, the amplitude of the transmission coefficient are set as 0.25, 0.2, and 0.15. For the MS configuration, 25% of the elements are transmitting-only and the remaining elements are reflecting-only. As can be observed, the MS configuration has the same error floor as the uniform amplitude configuration with $\beta^T = 0.25$. However, the error floor can only be achieved with higher transmit SNR for the MS configuration.

Furthermore, the error floors experienced by both users can be mitigated by adjusting the power ratio between the reflection and transmission coefficients in the uniform amplitude configuration. As depicted in Fig. 4.7, reducing β^T and increasing β^R contribute to lowering the error floor. This is because we assumed that the base station prioritizes

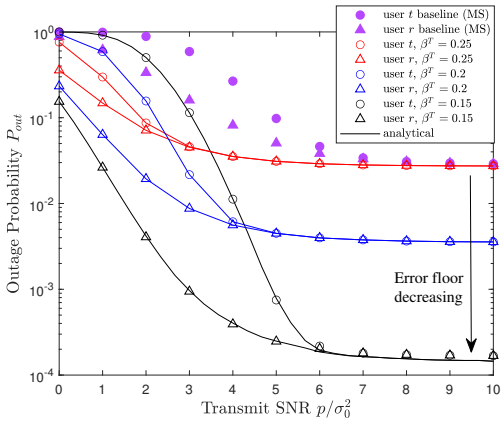

Figure 4.7: Outage probabilities of NOMA in the high transmit SNR regime.

decoding the message of user r first, and a smaller β^T results in decreased interference terms in both (4.21) and (4.22). However, it is important to note that although decreasing β^T leads to lower errors, achieving this lower error floor requires higher transmit SNR. In practical scenarios, the error floor cannot be arbitrarily reduced due to transmit power constraints.

4.2 Active STAR-RISs

As discussed in the previous section, under dual-sided incidence, each STAR element has four T&R coefficients, i.e., $\tilde{R}_m^A$, $\tilde{R}_m^B$, $\tilde{T}_m^{AB}$, and $\tilde{R}_m^{BA}$. These four coefficients transform the incident signals to the output signals of each STAR element. The relation between the incident and output signals is given by:

$$\begin{pmatrix} y_m^A \\ y_m^B \end{pmatrix} = \begin{pmatrix} \tilde{R}_m^A & \tilde{T}_m^{AB} \\ \tilde{T}_m^{BA} & \tilde{R}_m^B \end{pmatrix} \begin{pmatrix} s_m^A \\ s_m^B \end{pmatrix}, \tag{4.24}$$

or equivalently, $\mathbf{y}_m = \mathbf{\Xi}_m \cdot \mathbf{s}_m$, where $\mathbf{\Xi}_m$ is the T&R matrix of the mth STAR element. According to microwave network analysis, a STAR element is passive lossless if $\mathbf{\Xi}_m$ is unitary, i.e., $\mathbf{\Xi}_m^H \mathbf{\Xi}_m = \mathbf{I}_2$, where $\mathbf{I}_2$ denotes the two-by-two identity matrix. For passive lossy STAR element, $\mathbf{\Xi}_m^H \mathbf{\Xi}_m \prec \mathbf{I}_2$, and for active STAR element, $\mathbf{\Xi}_m^H \mathbf{\Xi}_m \succ \mathbf{I}_2$. In terms of reciprocity, a STAR-RIS can be either reciprocal or nonreciprocal. A STAR element is reciprocal if the T&R matrix $\mathbf{\Xi}_m$ is symmetrical, i.e., $\tilde{T}_m^{AB} = \tilde{T}_m^{BA}$. For nonreciprocal STAR matrix, we have $\tilde{T}_m^{AB} \neq \tilde{T}_m^{BA}$.

As illustrated in Fig. 4.8, the proposed active STAR-RIS element consists of three major components: a quadrature hybrid, positive-intrinsic–negative (PIN) diode phase-shifters, and reflection-type amplifiers [59]. Upon receiving the wireless signal, a 3-dB, 90° hybrid coupler with all four ports matched is employed to couple signals incident from both sides and minimize power loss. Then, PIN diode switches and phase-shifters are connected to port 2 and port 3 of the hybrid coupler to impose adjustable phase delay to the signal. Finally, the delayed signals are fed to reflection-type amplifiers. Depending

on the configurations of the phase-shifters and the gains of the amplifiers, the active STAR element structure has different overall transmission and reflection behavior. In the following, we formulate the T&R coefficient of the active STAR element in terms of the phase-shift values of the PIN diode phase-shifters and the gains of the reflective amplifiers.

4.2.1 Hardware Model for Active STAR-RISs

4.2.1.1 Active STAR Element with Coupled T&R Phase-Shift

If only one delay line and one reflection-type amplifier are available for each STAR element, the resultant element will exhibit coupled transmission and reflection coefficients. As illustrated in Fig. 4.8, the delay line and amplifier can be connected to either port 2 or port 3 of the hybrid coupler. Without loss of generality, suppose that port 2 is connected to the reflection-type amplifier with gain G_2 and port 3 is grounded i.e., $V_2^+ = \tilde{G}_2 V_2^-$ and $V_3^+ = 0$. Exploiting the scattering matrix of the quadrature hybrid, the output and input signal voltages have the following relation:

$$\begin{pmatrix} V_1^- \\ V_2^- \\ V_3^- \\ V_4^- \end{pmatrix} = -\frac{1}{\sqrt{2}} \begin{pmatrix} 0 & j & 1 & 0 \\ j & 0 & 0 & 1 \\ 1 & 0 & 0 & j \\ 0 & 1 & j & 0 \end{pmatrix} \begin{pmatrix} V_1^+ \\ V_2^+ \\ V_3^+ \\ V_4^+, \end{pmatrix} \tag{4.25}$$

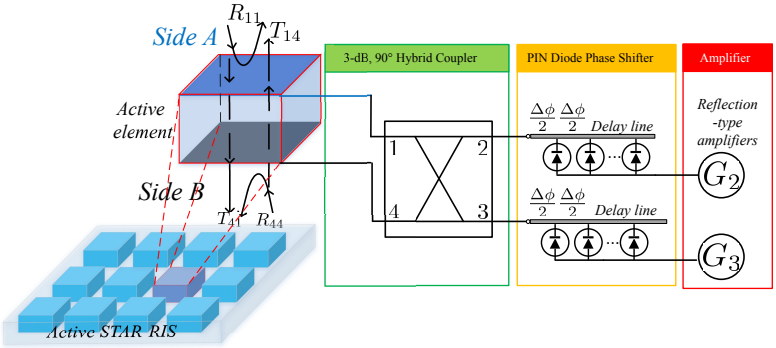

Figure 4.8: Hardware structure of an active STAR element.

where $V_2^+ = \tilde{G}V_2^-$, $V_3^+ = 0$, and $\tilde{G} = G_2 \cdot e^{j\phi_2}$ is the complex amplitude response of the delay line and amplifier combined. Using the relation given in (4.25), the output signals through port 1 and port 4, i.e., the wireless signals exit from *side A* and *side B* of the STAR element can be derived as follows:

$$V_1^- = -\frac{\tilde{G}}{2} \cdot V_1^+ + \frac{j\tilde{G}}{2} \cdot V_4^+ \tag{4.26}$$

$$V_4^- = \frac{j\tilde{G}}{2} \cdot V_1^+ + \frac{\tilde{G}}{2} \cdot V_4^+. \tag{4.27}$$

Theorem 10. *For STAR elements with coupled T&R phase-shift, the four T&R coefficients of the STAR elements which are connected to an amplifier with gain $\tilde{G}$ can be expressed as follows:*

$$R_m^A = \left.\frac{V_1^-}{V_1^+}\right|_{V_4^+=0} = -\tilde{G}/2, \quad R_m^B = \left.\frac{V_4^-}{V_4^+}\right|_{V_1^+=0} = \tilde{G}/2 \tag{4.28}$$

$$T_m^{AB} = \left.\frac{V_1^-}{V_4^+}\right|_{V_1^+=0} = j\tilde{G}/2, \quad T_m^{BA} = \left.\frac{V_4^-}{V_1^+}\right|_{V_4^+=0} = j\tilde{G}/2. \tag{4.29}$$

Proof. The proof is straightforward by exploiting the definitions of the T&R coefficients and the results obtained in (4.26) and (4.27). □

Remark 9. *It can be observed that for the case where one amplifier is employed per element, the T&R coefficients are highly coupled. Firstly, since the overall hardware structure is reciprocal, we have $T_m^{AB} = T_m^{BA}$. Next, consider the T&R coefficients which are involved in the single-side incidence from side A, i.e., R_m^A and T_m^{BA}, we have $(\phi_m^R - \phi_m^T)_A = \angle R_m^A - \angle T_m^{BA} = \pi/2$. Similarly, for side B, we have $(\phi_m^R - \phi_m^T)_B = \angle R_m^B - \angle T_m^{AB} = -\pi/2$. Note that the phase difference between the T&R coefficients for the two sides will be exchanged if the amplifier is connected to port 3. This indicates that the active coupled phase-shift STAR-RIS follows the same T&R phase-shift correlation as the passive-lossless STAR-RISs, i.e., $\phi_m^R - \phi_m^T = \pm\pi/2$ [60]. Finally, the amplitude of all*

four T&R coefficient are identical and they are determined by the gain of the amplifier G_2.

4.2.1.2 Active STAR Element with Independent T&R Phase-Shift

If two amplifiers are available for each STAR element, the resultant active STAR element has the ability to independently adjust the amplitude and phase-shift of the T&R coefficients. As illustrated in Fig. 4.8, the gains of the the two amplifiers are G_2 and G_3. We further denote $\tilde{G}_2 = G_2 e^{j\phi_2}$ and $\tilde{G}_3 = G_3 e^{j\phi_3}$ as the combined gain and phase-shift delay of port 2 and port 3, respectively. By substituting $V_2^+ = \tilde{G}_2 V_2^-$ and $V_3^+ = \tilde{G}_3 V_3^-$ into (4.25), the output signals at port 1 and port 4 are given by:

$$V_1^- = \frac{\tilde{G}_3 - \tilde{G}_2}{2} \cdot V_1^+ + \frac{j(\tilde{G}_2 + \tilde{G}_3)}{2} \cdot V_4^+ \tag{4.30}$$

$$V_4^- = \frac{j(\tilde{G}_2 + \tilde{G}_3)}{2} \cdot V_1^+ + \frac{\tilde{G}_2 - \tilde{G}_3}{2} \cdot V_4^+. \tag{4.31}$$

Theorem 11. *For STAR elements with independent active T&R phase-shift, the four T&R coefficients of the STAR elements which are connected to amplifiers with gain* $\tilde{G}_2$ *and* $\tilde{G}_3$ *can be expressed as follows:*

$$R_m^A = -R_m^B = (\tilde{G}_3 - \tilde{G}_2)/2 \tag{4.32}$$

$$T_m^{AB} = T_m^{BA} = j(\tilde{G}_2 + \tilde{G}_3)/2. \tag{4.33}$$

Proof. The proof is straightforward by exploiting the results obtained in (4.30) and (4.31). □

Remark 10. *It can be observed that since the amplitudes and phases of both* G_2 *and* G_3 *can be adjusted by tuning the phase-shift delay lines and amplifiers, the amplitudes and phases the T&R coefficients can be independently configured. Moreover, the transmitting-only and reflecting-only modes can be achieved by letting* $\tilde{G}_2 = \tilde{G}_3$ *and* $\tilde{G}_2 = -\tilde{G}_3$*, respectively. However, due to the reciprocal design, the phase-shift and amplitudes of the*

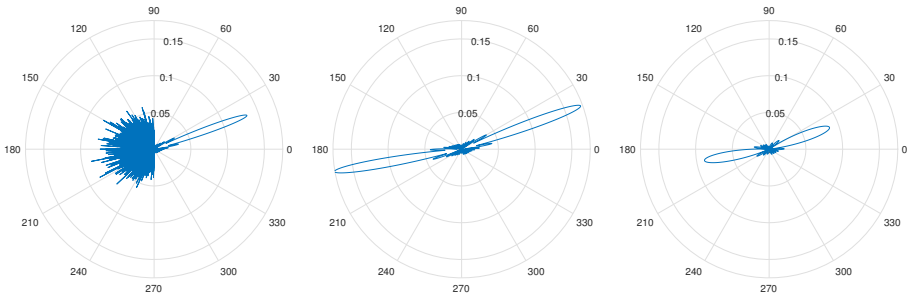

(a) Coupled phase-shift, active (b) Independent phase-shift, active (c) Passive-lossless STAR-RIS

Figure 4.9: Simulated radiation pattern of active and passive STAR-RISs.

transmission coefficients in the two directions remain identical, i.e., $T_m^{AB} = T_m^{BA}$.

4.2.2 System Model and Radiation Pattern

We investigate a two-user downlink communication system where single-antenna base station (BS) is located on *side A* and the two users are locate on different sides of the STAR-RIS. The direct link from BS to both users are assumed to be severely blocked. As a result, an active STAR-RIS is deployed to recover the service for the two users. Let g_m denote the channel between the BS and the mth active STAR element, h_m^χ denote the channel between the mth active STAR element and the user χ where $\chi \in \{A, B\}$ denotes the user on *side A* or *side B*. All channel are assumed to exhibit Rician fading, i.e., $|h_m^\chi| \sim \mathcal{R}(K_h^\chi, \Omega_h^\chi)$ and $|g_m| \sim \mathcal{R}(K_g, \Omega_g)$, where K_h^χ and K_g are the shape parameters, Ω_h^χ and Ω_g are the scale parameters of the corresponding Rician channels. Considering the noise at the active STAR element and at each users, the received signal for user χ in the downlink scenario is given by:

$$y^\chi = \sum_{m=1}^{M} h_m^\chi G_m^\chi e^{j\phi_m^\chi}(g_m s_m + v_m) + n^\chi \tag{4.34}$$

where G_m^χ and ϕ_m^χ are the amplitude and phase-shift of the T&R coefficient of the mth element corresponding to user χ, respectively. v_m is the noise caused by the mth active STAR element, n^χ is the noise caused by user χ. We further assume that the channel state information is known at the active STAR-RIS. As a result, the cophase condition can be adopted to align the phase-shift of each active STAR signals at both users.

In Fig. 4.9, we illustrate the angular patterns of the active STAR-RIS with coupled and independent T&R phase-shift and the passive-lossless STAR-RIS as a baseline. In all scenarios, we consider a STAR-RIS with 18×18 elements. We assume that user A and user B are located at angular positions of 20° and 190° with equal distances of 10 m from the STAR-RIS, respectively. As can be seen from Fig. 4.9(a), the coupled phase-shift active STAR-RIS forms a narrow beam towards user A. However, for the transmission space (the second and third quadrants), there are no observable beams. This is because due to the phase-shift coupling, only the reflection phase-shift follows the cophase condition for user A. The radiation pattern for independent active STAR-RIS is shown in Fig. 4.9(b). Compared with the coupled phase-shift scenario, the signal strength is focused for both user A and B. Moreover, based on the proposed hardware models, the each independent active STAR element employs one more amplifier compared to the coupled phase-shift STAR element. As a result, the independent phase-shift STAR-RIS achieve larger amplitudes for both reflected and transmitted beams. In comparison, the passive-lossless STAR-RIS shown in Fig. 4.9(c) has the smallest reflection and transmission beam amplitudes.

4.2.3 Performance Analysis

To evaluate the performance of the proposed active STAR-RIS, in this section, we study a active STAR-RIS-aided wireless communication system serving two users. Based on the proposed active STAR-RIS hardware model, the outage probabilities and their asymptotic behaviours are analyzed. For both coupled and independent phase-shift scenario, the received SNR of user χ is given as follows:

$$\gamma^{\chi} = \frac{p|\sum_{m=1}^{M} h_m^{\chi} G_m^{\chi} e^{j\phi_m^{\chi}} g_m|^2}{|\sum_{m=1}^{M} h_m^{\chi} G_m^{\chi} e^{j\phi_m^{\chi}}|^2 \sigma_v^2 + \sigma_{\chi}^2} \tag{4.35}$$

where P is the transmit power of the BS, σ_v^2 is the variance of v_m, σ_{χ}^2 is the variance of n^{χ}.

4.2.3.1 Scaling Laws

The following theorems give the scaling laws for the SNRs of both users. We investigate the received SNR of both users in the high transmit SNR limit, i.e., $p/\sigma_\chi^2 \to \infty$. For active STAR-RISs with coupled T&R phase-shift, assume that the phase-shift reflection coefficients of the active element are configured to align the signals for user A. Due to the coupling between R_m^A and T_m^{BA}, the phase-shift of the transmission coefficients are not optimized for user B.

Theorem 12. *For active STAR-RISs with coupled T&R phase-shift, the scaling laws for the received SNRs are given as follows:*

$$\overline{\gamma^A} = \frac{p|MG_m\overline{h_m^A}\overline{g}_m|^2}{M\pi G_m^2\overline{(h_m^A)^2}\sigma_v^2/4+\sigma_A^2} \to \frac{p}{\sigma_v^2}\frac{4\overline{h_m^A}\overline{g}_m}{\pi\overline{(h_m^A)^2}}\cdot M \tag{4.36}$$

$$\overline{\gamma^B} = \frac{pMG_m^2\pi\overline{(h_m^Bg_m)^2}/4}{M\pi G_m^2\overline{(h_m^B)^2}\sigma_v^2/4+\sigma_B^2} \to \frac{p}{\sigma_v^2}\frac{\overline{(h_m^Bg_m)^2}}{\overline{(h_m^B)^2}}, \tag{4.37}$$

where $\overline{x}$ denotes the expected value of a random variable x, G_m denotes the maximum gain of an active STAR element.

Proof. For user A, the reflection coefficients are configured to align the phase-shifts of the cascaded channels $h_m^A g_m$. Thus, we have $\sum h_m^A g_m R_m^A = \sum |h_m^A||g_m||R_m^A|$. Next, since h_m^A and g_m are independent Rician variables, the phases of each terms of $h_m^A R_m^A$ can be regarded as randomly distributed. According to the law of large numbers, the expectation value of the sum in the denominator can be calculated as $\mathbb{E}[|\sum h_m^A R_m^A|] = \frac{1}{2}\sqrt{M\pi\overline{(h_m^A)^2}|R_m^A|^2}$. For user B, its channel experience random phase alignment due to the T&R phase-shift coupling. Both summations in (4.35) for $\chi = B$ (user B) have randomly distributed phase-shifts and their expected values can be obtained in similar fashion using the law of large numbers. □

Remark 11. *For the coupled T&R phase-shift scenario, the SNRs for user A scales with M and the SNR of user B is upper bounded by a constant value. Recall that for*

passive STAR-RISs, the SNRs for users scales with M^2. Although passive STAR-RISs have better performance asymptotically, active STAR-RISs are able to outperform passive ones before reaching the large M limit, i.e., with a practical number of elements. More importantly, the gain G_m introduced by the active elements can significantly increase users SNRs for the cases where M is small, as can be observed in (4.36).

Theorem 13. *For active STAR-RISs with independent T&R phase-shift, the scaling laws for the two users can be calculated as follows:*

$$\overline{\gamma^{\chi}} = \frac{p|MG_m^{\chi}\overline{h_m^{\chi}}\overline{g}_m|^2}{M\pi(G_m^{\chi})^2\overline{(h_m^{\chi})^2}\sigma_v^2/4+\sigma_{\chi}^2} \rightarrow \frac{p}{\sigma_v^2}\frac{4\overline{h_m^{\chi}}\overline{g}_m}{\pi\overline{(h_m^{\chi})^2}} \cdot M \tag{4.38}$$

where $G_m^A = |(\tilde{G}_3 - \tilde{G}_2)/2|$ is the magnitude of the reflection coefficient of the independent phase-shift active STAR element and $G_m^B = |(\tilde{G}_3 + \tilde{G}_2)/2|$ is the magnitude of the transmission coefficient.

Proof. The proof of this theorem follows a similar process as in Theorem 12. □

4.2.3.2 Outage Probability and Diversity Orders

The outage probability of user χ is calculated as follows:

$$P_{out}^{\chi} = Pr\left\{\gamma^{\chi} < \gamma_{target}^{\chi}\right\}, \tag{4.39}$$

where γ^{χ} is the received SNR of user χ, which is given in (4.35). For simplicity, we further assume that the gains of the STAR elements are the same, i.e., $G_m^{\chi} = G^{\chi}$, $\forall m \in \{1, \cdots, M\}$. In the following, we investigate the outage probabilities of both users for both coupled and independent T&R phase-shift scenarios in two theorems.

Theorem 14. *For user A under coupled phase-shift STAR-RIS or both users under independent phase-shift scenario, their asymptotic outage probabilities can be expressed*

as follows:

$$P_{out}^{R}(\gamma_{target}^{\chi}) = \left[\frac{4(K_h^{\chi}+1)(K_g+1)\sigma_{\Sigma}^2\gamma_{target}^{\chi}}{\Omega_h^{\chi}\Omega_g e^{K_h^{\chi}+K_g}G^{\chi}}\right]^M \frac{p^{-M}}{(2M)!}, \tag{4.40}$$

where $\sigma_{\Sigma}^2 = M\Omega_h^{\chi}G^{\chi}\sigma_v^2 + \sigma_{\chi}^2$ *is the variance of the combined noise at the active STAR elements and at the receiver.*

Proof. In the high transmit SNR limit, we approximate the overall received noise, i.e., the denominator of (4.35) with its variance σ_{Σ}^2. Since the phase of each term in the summation $\sum_m^M h_m^{\chi}G_m^{\chi}e^{j\phi_m^{\chi}}$ is randomly aligned, we have $\sigma_{\Sigma}^2 = M\Omega_h^{\chi}G^{\chi}\sigma_v^2 + \sigma_{\chi}^2$. Next, we consider the nominator of (4.35), according to the system model, both $|g_m|$ and $|h_m^{\chi}|$ follow Rician distributions. After the phase alignment of active STAR element, we only need to consider the distribution of $H^{\chi} = \sum_m^M |g_m||h_m^{\chi}|$. Each term in the summation is the product of two independent Rician random variables whose probability distribution function (PDF) is given in [56]. We approximate the PDF of $|g_m||h_m^{\chi}|$ near the origin using a Taylor series expansion:

$$f_{|h_m^{\chi}||g_m|}(x) = \frac{4(K_h^{\chi}+1)(K_g+1)}{\Omega_h^{\chi}\Omega_g e^{(K_h^{\chi}+K_g)}} \cdot x + o(x), \tag{4.41}$$

where $o(\cdot)$ is the little-o notation and $o(f(x))$ denotes a function which is asymptotically smaller than $f(x)$. Then Laplace transform of $|H^{\chi}|$ can be calculated as follows:

$$\begin{aligned}\mathcal{L}\{f_{|H^{\chi}|}(x)\}(t) &= \left(\mathcal{L}\{f_{|h_m^{\chi}||g_m|}(x)\}(t)\right)^M \\ &= \left[\frac{4(K_h^{\chi}+1)(K_g+1)}{\Omega_h^{\chi}\Omega_g e^{(K_h^{\chi}+K_g)}}\right]^M t^{-2M} + o(t^{-2M}).\end{aligned} \tag{4.42}$$

Finally, the PDF of $|H^{\chi}|$ can be obtained by performing the inverse Laplace transform of (4.42). The outage probability can therefore be derived using the obtained PDF. □

Based on the derived asymptotic outage probability, we investigate the diversity order of user χ, which is defined as follows:

$$d^{\chi} = -\lim_{p\to\infty} \frac{\log P_{out}^{\chi}(\gamma_{\text{target}}^{\chi})}{\log p}. \tag{4.43}$$

Corollary 5. *The diversity order of user A under coupled phase-shift STAR-RIS or both users under independent phase-shift scenario are given by:*

$$d_{independent}^{\chi} = d_{coupled}^{A} = M. \tag{4.44}$$

Proof. Combining (4.40) with (4.43), it is straightforward to obtain (4.44). □

Theorem 15. *For user B under coupled phase-shift scenario, the outage probabilities can be expressed as follows:*

$$P_{out}^{B}(\gamma_{target}^{B}) = 1 - \exp\left\{-\frac{\gamma_{target}^{B}\sigma_{\Sigma}^{2}}{M\Omega_{h}^{B}\Omega_{g}(G^{\chi})^{2}p}\right\}, \tag{4.45}$$

where $\sigma_{\Sigma}^{2} = M\Omega_{h}^{B}G^{B}\sigma_{v}^{2} + \sigma_{B}^{2}$ is the variance of the combined noise at the active STAR elements and at receiver B.

Proof. For user B under the coupled phase-shift scenario, the numerator of (4.35) undergoes a random phase-shift alignment. Thus, the overall channel of $|H^{B}| = |\sum_{m}^{M} h_{m}^{\chi} g_{m} e^{j\phi_{m}^{\chi}}|$ follows a Rayleigh distribution, i.e., $f_{|H^{B}|}(x) = \frac{2x}{\Omega^{B}} e^{-x^{2}/\Omega^{B}}$, where $\Omega^{B} = M\Omega_{h}^{B}\Omega_{g}$ [60]. Then, the outage probability of user B can be derived by exploiting its definition given in (4.39). □

Corollary 6. *The diversity order of user B under coupled phase-shift STAR-RIS is given by:*

$$d_{coupled}^{B} = 1. \tag{4.46}$$

Proof. Combining (4.45) with (4.43) and exploiting the fact that the Taylor expansion

of $e^x = 1 + x + o(x^2)$ near the origin, it is straightforward to obtain (4.44). □

4.2.4 Summary

In Table 4-B, we summarize the analytical insights obtained from this section. As shown in the table, the sum diversity order of the two users and the received SNR scaling laws are compared for active and passive STAR-RISs. In general, the active STAR-RISs with independent T&R phase-shift achieve the same full-diversity order as their passive lossless counterparts. However, the power scaling law of active STAR-RIS are slower than passive lossless ones. For active STAR-RIS, the quadratic power scaling is traded for a higher channel gain. As a result, the performance gain of active STAR-RISs is only significant when the number of STAR element is small and the transmit SNR is low.

STAR-RISs	Diversity Order	Scaling Law
Active, Coupled	$M+1$	$\propto M$ or bounded
Active, Independent	$2M$	$\propto M$
Passive Lossless	$2M$	$\propto M^2$

Table 4-B: Summary of diversity order and scaling law for active and passive STAR-RISs

4.2.5 Numerical Results

In this section, simulation results are provided to investigate the performance of the active STAR-RIS-aided communication. For our simulations, we assume that the active STAR-RIS is a uniform planar array consisting of M elements. The spacing between adjacent elements is half of the carrier wavelength. The noise power for both users is set to $\sigma_A^2 = \sigma_B^2 = -10$ dBm and the noise power of the active element is set to $\sigma_v^2 = -20$ dBm. Moreover, the gain of the reflection-type amplifiers are set to $G_2 = G_3 \approx 1.5$ dB. All STAR-RIS-user channels are modeled as Rician fading channels with path loss exponents of $\alpha = 2.2$ and the Rician factor of $K = 1.5$ dB.

In Fig. 4.10, the received SNR is plotted against the number of STAR elements. As can be observed in the figure, the independent active STAR-RIS has the highest SNRs and outperforms both active STAR-RIS with coupled phase-shift and passive STAR-

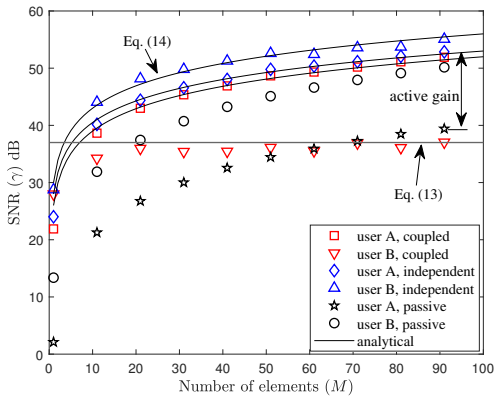

Figure 4.10: Simulated and analytical results for SNR scaling laws of user A and user B.

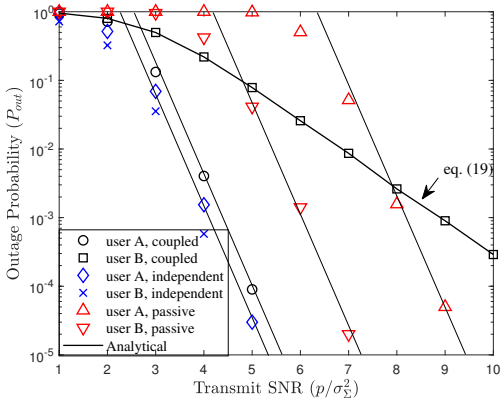

Figure 4.11: Simulated and analytical asymptotic results for outage probabilities of user A and user B.

RIS. For the coupled phase-shift active STAR-RIS, the received SNR for user A always outperforms the passive STAR-RIS. However, in terms of the received SNR for user B, the passive STAR-RIS outperforms coupled phase-shift active STAR-RIS after $M > 70$. This is due to the fact that the received SNR of user B is upper bounded as derived in (4.37). Based on these observations, we can conclude that the perform gain of active STAR-RIS over passive ones is more significant when there is size restriction or the number of elements is small.

In Fig. 4.11, we investigate the outage probabilities for both users for the case of coupled phase-shift active STAR-RIS, independent phase-shift active STAR-RIS, and passive-lossless STAR-RIS. As can be observed, the independent phase-shift active STAR-

RIS achieves the lowest outage probabilities for both users. For the case of coupled phase-shift STAR-RIS, user A has a lower outage compared to the passive baseline. However, user B has a smaller diversity order as derived in (4.46). As a result, the passive STAR-RIS outperform the coupled phase-shift STAR-RIS when transmit SNR is high. Based on these observations, we can conclude that the perform gain of active STAR-RIS over passive ones is more significant when the transmit SNR is lower.

4.3 Summary

In this chapter, we provided the hardware model and signal model for the dual-sided STAR-RISs and active STAR-RISs. For the case where the STAR-RIS have surface electric and magnetic impedance, the elements have symmetrical T&R coefficients. We derived expressions for the outage probability of a STAR-RIS assisted two-user uplink communication system in high transmit SNR regime. The analytical and numerical results demonstrated the performance gain of NOMA over OMA. It is also revealed that the error floor for the uplink NOMA transmission can be lowered by adjusting the power ratios of STAR elements. We also studied the performance of an active STAR-RIS-aided two user wireless communication system. We derived expressions for the asymptotic received SNRs and outage probabilities of both users for the case of coupled phase-shift and independent phase-shift. It was proved that both user can achieve full diversity order under independent phase-shift active STAR-RIS. Finally, numerical results demonstrated the performance gain of active STAR-RIS over passive ones. It was also revealed that the performance gain is more significant when the number of STAR element is small and the transmit SNR is low.

It is important to note that the results presented in this chapter are applicable specifically to the far-field region of STAR-RIS. Additionally, the signal models provided in Theorem 8 and 10 are only valid for patch-array-based STAR-RISs. However, with the recent advancements in metasurface technology, metasurface-based RISs/STAR-RISs have emerged as a promising area of research due to their continuous aperture

and spatially-continuous phase-shift capabilities. In the upcoming chapter, we delve into electromagnetic theory and employ the Green's function method to investigate the fundamental performance limits of metasurface-based RISs.

Chapter 5

A Green's Function Method-Based Channel Model for STAR-RISs

This chapter is organized as follows. The main contributions of this work is first introduced in 5.1. Section 5.2 introduces the Green's function method, based on which the channel model for metasurface-based RISs and STAR-RISs is proposed. Section 5.3 analyze the fundamental performance limits in the transmitting/reflecting-only RIS-aided single-user scenario. The upper bound of the end-to-end channel gain, DoF, and the power scaling law are given. In Section 5.4, the three proposed configuration strategies for STAR-RIS-aided multi-user communication scenario are given. The performance analysis is carried out in both pure near-field regime and hybrid near- and far-field regime. Finally, Section 5.5 provides numerical results to verify our theoretical analysis, which is followed by the conclusions in Section 5.6.

5.1 Introduction

In contrast to the well-studied patch-array-based RISs, this chapter focuses on the metasurface-based RISs and STAR-RISs where the elements have millimeter or even molecular sizes. For these small metasurface structures, near-field effects are dominant and a continuous electric current distribution should be adopted for capturing their electromagnetic response instead of discrete phase-shift matrices. Exploiting the electric current distribution, a Green's function method based channel model is proposed. Based on the proposed model, performance analysis is carried out for both transmitting/reflecting-only RISs and STAR-RISs. 1) For the transmitting/reflecting-only RIS-aided single-user scenario, closed-formed expressions for the near-field/far-field boundary and the end-to-end channel gain are derived. Then, degrees-of-freedom (DoFs) and the power scaling laws are obtained. It is proved that the near-field channel exhibits higher DoFs than the far-field channel. It is also confirmed that when communication distance increases beyond the field boundary, the near-field power scaling law simplifies to the well-known far-field result. 2) For the STAR-RIS-aided multi-user scenario, three practical STAR-RIS configuration strategies are proposed, namely power splitting (PS), selective element grouping (SEG), and random element grouping (REG) strategies. The channel gains for users are derived within both the pure near-field regime and the hybrid near-field and far-field regime. Finally, numerical results confirm that: 1) for metasurface-based RISs, the field boundary depends on the sizes of both the RIS and the receiver, 2) the received power scales quadratically with the number of elements within the far-field regime and scales linearly within the near-field regime, and 3) for STAR-RISs, SEG has the highest near-field channel gain among the three proposed strategies and PS yields the highest DoFs for the near-field channel.

The main contributions can be summarized as follows:

- We propose a novel channel model for metasurface-based RISs and STAR-RISs, where we exploit the Green's function method and the current-based characterization for the elements. We illustrate how transmitting-only RISs, reflecting-

only RISs, and STAR-RISs can be achieved by configuring the current distributions. We then analyze the near-field and far-field performance in both the transmitting/reflecting-only RISs-aided single-user scenario and the STAR-RIS-aided multi-user scenarios.

- For transmitting/reflecting-only RIS-aided single-user scenario, we derive the position of the field boundary by taking into account the size of both the RIS and the receiver. We also derive the fundamental performance limits of RIS-aided communication in terms of the maximum end-to-end channel gain, DoF, and the power scaling law. These obtained near-field metrics are then compared with those in the far-field regime. Specifically, we show that the received power scales linearly with the number of elements within the near-field regime and scales quadratically within the far-field regime.

- For STAR-RIS-aided multi-user scenario, we propose three practical configuration strategies for employing STAR-RISs, namely power splitting (PS), selective element grouping (SEG), and random selective element grouping (REG) strategies. We derive closed-form expressions for the channel gain of each proposed strategies within the pure near-field regime. We also evaluate the performance of STAR-RIS in the hybrid near-field and far-field regime, where the STAR-RIS is deployed to assist one near-field user on the transmission side and one far-field user on the reflection side. The channel gains for both users are derived for the case without STAR-RIS and for the case with STAR-RIS under three proposed configuration strategies.

- Our simulation results verify that 1) for metasurface-based RISs with larger sizes and receivers with larger aperture areas, the near-field regime expands and the field boundary is further away from the RIS, 2) for the STAR-RIS-aided multi-user pure near-field communication scenario, the SEG strategy has the best sum rate performance of all three strategies but yields lower DoFs for the end-to-end channel, and 3) for the STAR-RIS-aided multi-user hybrid near- and far-field communication

scenario, STAR-RIS can significantly increase the channel gains of users and thus can improve the signal coverage especially in the indoor "blind zone".

5.2 A Green's Function Method Based Channel Model for Metasurface-Based RISs and STAR-RISs

In this section, we give the general formulation of the Green's function method based channel modeling method for metasurface-based STAR-RISs, where transmitting-only and reflecting-only RISs can be regarded as special cases. Then, we present the current-based characterization of STAR elements and the channel model for both near-field and far-field regimes. We then show the differences and connections between the proposed model and the transmission and reflection (T&R) coefficients based channel model for patch-array-based STAR-RISs, which was previously given in [24]. Finally, we give an example on how reflecting-only RISs, transmitting-only RISs, and STAR-RISs can be modeled with different equivalent current distributions.

5.2.1 The Green's Function Method

We denote the volume (space) occupied by the STAR-RIS (or RIS) as V_T and the volume of the receiver as V_R. The EM response of STAR-RIS can be characterized using equivalent current distribution within V_T. According to electromagnetic (EM) theory, the reflected/transmitted EM field in the region outside of V_T can be calculated using the electric current $\mathbf{J}(\mathbf{r}')$, where $\mathbf{r}'$ is the position of the source point within V_T. Particularly, exploiting the Green's function approach, the electric field vector at field point $\mathbf{r}$ (position of the receiver) is given by [21, Eq. (9)]:

$$\mathbf{E}(\mathbf{r}) = \int_{V_T} \overline{\overline{\mathbf{G}}}(\mathbf{r}, \mathbf{r}')\mathbf{J}(\mathbf{r}')\mathrm{d}V_T, \tag{5.1}$$

where $\overline{\overline{\mathbf{G}}}(\mathbf{r}, \mathbf{r}')$ is the tensor Green's function. The exact form of $\overline{\overline{\mathbf{G}}}(\mathbf{r}, \mathbf{r}')$ depends on the boundary conditions and the position of the user [21]. If multiple users are involved,

each of them corresponds with a different Green's function.

5.2.2 Current-Based Characterization of STAR-RIS Elements

In this work, the STAR-RIS is characterized using the strength and phases of the equivalent current, i.e., $\mathbf{J}(\mathbf{r}')$. Its distribution depends on the incident field and the surface impedance configuration of the STAR-RIS elements. In prior works, the patch-array-based STAR-RIS is modeled using the transmission and reflection (T&R) coefficients of each element [24, 60]. Note that the T&R coefficient of each patch is the macroscopic effect of the microscopic electric currents induced within each STAR-RIS element. For the purpose of obtaining fundamental performance limit for metasurface-based STAR-RIS, in this work, we use the equivalent current-based characterization. However, the T&R coefficients characterization for the mth element can be related to the equivalent current-based characterization through the following integration:

$$T_m = \frac{|\mathbf{E}(\mathbf{r}_T)|}{|\mathbf{E}_{inc}|} = \left| \int_{V_m} \overline{\overline{\mathbf{G}}}(\mathbf{r}_T, \mathbf{r}') \mathbf{J}(\mathbf{r}') \mathrm{d}V_m \right|, \tag{5.2}$$

$$R_m = \frac{|\mathbf{E}(\mathbf{r}_R)|}{|\mathbf{E}_{inc}|} = \left| \int_{V_m} \overline{\overline{\mathbf{G}}}(\mathbf{r}_R, \mathbf{r}') \mathbf{J}(\mathbf{r}') \mathrm{d}V_m \right|, \tag{5.3}$$

where $|\mathbf{E}|$ denotes the complex amplitudes of a field, $\mathbf{r}_T$ and $\mathbf{r}_R$ are the reference point on the transmission/reflection side of the STAR-RIS, $\mathbf{J}(\mathbf{r}')$ is the electric current induced by a normalized incident field, and V_m is the volume of the mth element. In practice, the induced current $\mathbf{J}(\mathbf{r}')$ can be configured by adjusting the electric impedance of the STAR-RIS elements [50]. Thus, using the equivalent current instead of the T&R coefficients, we can obtain more fundamental performance limits of STAR-RISs[1].

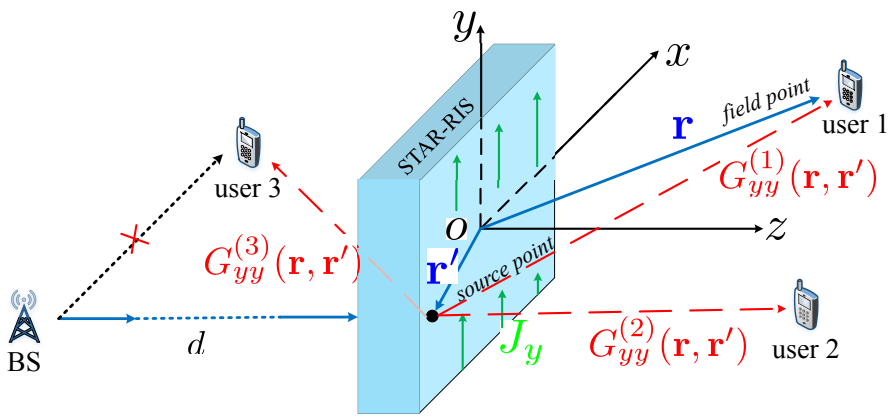

Figure 5.1: A Green's function-based channel model for metasurface-based STAR-RISs.

5.2.3 Channel Model

As illustrated in Fig. 5.1, we consider a STAR-RIS centered at the origin of the coordinate system. With the assistance of a STAR-RIS, a single antenna base station (BS) communicates with receivers which are located on the $x-z$ plane. We assume that the BS is located in the far-field of the STAR-RIS and the receivers are within the near-field of STAR-RIS. Consider the case of a vertically polarized wireless signal, the equivalent electric currents induced within V_T are in the y-direction, i.e., $\mathbf{J}(\mathbf{r}') = \hat{\mathbf{y}} J_y(\mathbf{r}')$, and the electric field they generate at receiver i is $\mathbf{E}^{(i)}(\mathbf{r}) = \hat{\mathbf{y}} E_y^{(i)}(\mathbf{r})$. According to (5.1), these received fields are given by:

$$E_y^{(i)}(\mathbf{r}) = \int_{V_T} G_{yy}^{(i)}(\mathbf{r},\mathbf{r}') J_y(\mathbf{r}') \mathrm{d}^3\mathbf{r}', \tag{5.4}$$

where $G_{yy}^{(i)}$ is the (y,y)-element of the Green's tensor for receiver i. For free space transmission, we have [10]:

$$G_{yy}^{(i)}(\mathbf{r},\mathbf{r}') = -(j\omega\mu_0 + \frac{k^2}{j\omega\epsilon_0}) \frac{\exp\left(-jk|\mathbf{r}-\mathbf{r}'|\right)}{4\pi|\mathbf{r}-\mathbf{r}'|}, \tag{5.5}$$

[1]The current distribution provides a more detailed EM-response than the element-wise T&R phase-shift coefficients. The phase-shift model uses only a single phase-shift value for the entire element, thus ignoring the phase difference of the electric fields within each element. Also, in existing models, the phase-shift coefficients are assumed to be the same for receivers in different directions, although this is not the case in practice.

where μ_0 and ϵ_0 are the free space permeability and permittivity, respectively, ω and k are the signal frequency and wave number, respectively.

Next, we formulate the received power at the receiving volume V_R. To obtain the largest received power possible, $J_y(\mathbf{r}')$ must be configured such that the electric field it generate, according to (5.4), yield the largest integrated E-field magnitude within V_R, i.e.,

$$|h_{\text{T-to-R}}|^2 = \int_{V_R} E_y^*(\mathbf{r}) E_y(\mathbf{r}) \mathrm{d}^3\mathbf{r}. \tag{5.6}$$

For brevity, we omit the index (i) for the ith user and give the end-to-end channel gain between the BS and V_R in the following lemma:

Lemma 3. *The maximum magnitude of the end-to-end channel gain between the BS and the receiving volume (V_R) is given as follows:*

$$|h_{end\text{-}to\text{-}end}|^2 = \frac{DA_T}{4\pi d^2} \int_{V_T} J_y^*(\mathbf{r}_1') \int_{V_T} K(\mathbf{r}_1', \mathbf{r}_2') J_y(\mathbf{r}_2') \mathrm{d}^3\mathbf{r}_1' \mathrm{d}^3\mathbf{r}_2', \tag{5.7}$$

where D is the directivity of the BS antenna, A_T is the aperture size of STAR-RIS facing the base station, d is the distance between BS and STAR-RIS, $J_y(\mathbf{r})$ is the normalized current distribution within V_T, i.e., $< \mathbf{j}_1, \mathbf{j}_2 >= \int_{V_t} \mathbf{j}_1^T \mathbf{j}_2^* \, dV_T = 1$, $\mathbf{A}^T$ is the transpose of vector $\mathbf{A}$, * denotes the complex conjugate, and

$$K(\mathbf{r}_1', \mathbf{r}_2') = \int_{V_R} G_{yy}^*(\mathbf{r}, \mathbf{r}_1') G_{yy}(\mathbf{r}, \mathbf{r}_2') \mathrm{d}^3\mathbf{r} \tag{5.8}$$

is a kernel function in the space within V_T.

Proof. The channel gain can be expressed as the product of two parts, $D\frac{A_T}{4\pi d^2}$ is the maximum channel gain between BS and the STAR-RIS, and $|h_{\text{T-to-R}}|^2$ is the gain between STAR-RIS and a receiver. For the first part, according to the Friis' formula, the received power from a far-field antenna with a directivity of D is given as follows:

$$P_r = D\frac{A_T}{4\pi d^2} P_t, \tag{5.9}$$

where P_t is the transmit power. For the second part, the proof is straightforward by substituting (5.4) into (5.6):

$$|h_{\text{T-to-R}}|^2 = \int_{V_R}\int_{V_T}\int_{V_T} G_{yy}^*(\mathbf{r},\mathbf{r}_1')J_y(\mathbf{r}_1')G_{yy}(\mathbf{r},\mathbf{r}_2')J_y(\mathbf{r}_2')\mathrm{d}^3\mathbf{r}_1'\mathrm{d}^3\mathbf{r}_2'\mathrm{d}^3\mathbf{r} \tag{5.10}$$

Since in (5.10), only the Green's functions G_{yy} are functions of the field point $\mathbf{r}$, the integral within V_R can be evaluated separately as a kernel, i.e., $K(\mathbf{r}_1',\mathbf{r}_2')$. □

Remark 12. *The kernel function can be understand as a measurement of the coupling strength of two source point (located at $\mathbf{r}_1'$ and $\mathbf{r}_2'$) which is then averaged within V_R. According to its definition, $K(\mathbf{r}_1',\mathbf{r}_2')$ is a Hermitian operator, i.e., $K(\mathbf{r}_1',\mathbf{r}_2') = K^*(\mathbf{r}_2',\mathbf{r}_1')$, and thus is diagonalizable under a complete set of basis functions in V_T. According to linear algebra [61], the quantity in* (5.7) *is maximized when $J_y(\mathbf{r}')$ is chosen to be the eigenfunction of $K(\mathbf{r}_1',\mathbf{r}_2')$ with the largest eigenvalue. In other words, we have the following relation for $h_{T\text{-}to\text{-}R}$, $J_y(\mathbf{r}')$, and $K(\mathbf{r}_1',\mathbf{r}_2')$:*

$$|h_{T\text{-}to\text{-}R}|^2 \cdot J_y(\mathbf{r}_1') = \int_{V_T} K(\mathbf{r}_1',\mathbf{r}_2')J_y(\mathbf{r}_2')\mathrm{d}^3\mathbf{r}_2'. \tag{5.11}$$

In practice, $J_y(\mathbf{r}')$ is determined by the phase-shift configuration of the STAR-RIS elements and the kernel $K(\mathbf{r}_1',\mathbf{r}_2')$ is determined by the positional information of the receiver as well as the environment. In addition, the DoF of the end-to-end channel is related to the number of eigenfunctions of the kernel function in (5.11) *with significant eigenvalues [62]. In the following sections, we can obtain the closed-form channel gain by choosing different current distribution $J_y(\mathbf{r}')$ for transmitting/reflecting-only RISs and STAR-RISs.*

5.2.4 Modeling of Reflecting-Only RISs, Transmitting-Only RISs, and STAR-RISs with Equivalent Current Distributions

Before commencing with deriving the closed-form channel gain for the metasurface-based RISs and STAR-RISs, we elaborate on the relation between the distribution of $J_y(\mathbf{r}')$

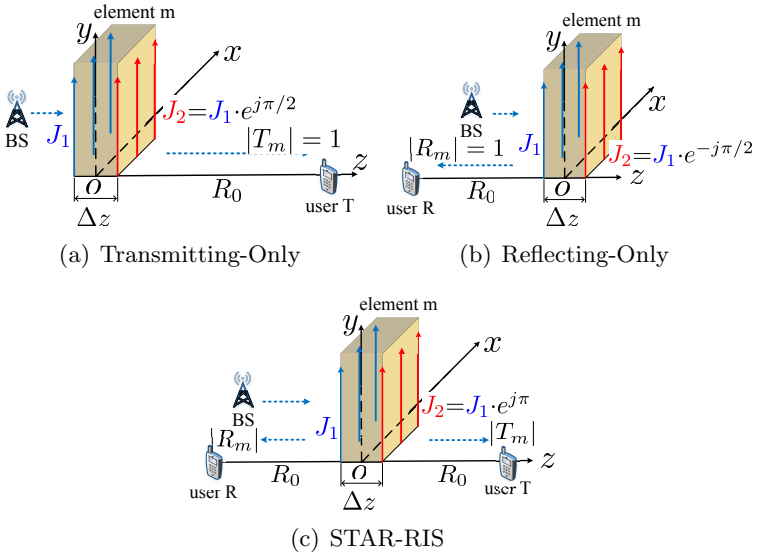

(a) Transmitting-Only (b) Reflecting-Only

(c) STAR-RIS

Figure 5.2: Illustration of current distributions for different RIS types.

and the types of RISs, i.e., reflecting-only RISs, transmitting-only RISs, and STAR-RISs. As shown in (5.2) and (5.3), the T&R coefficients are determined by the distribution of $J_y(\mathbf{r}')$ within each macroscopic element (V_m). To give the readers a better idea of the Green's function-based channel model, we give examples of the exact distributions of $J_y(\mathbf{r}')$ which corresponds to the different RIS types.

As shown in Fig. 5.2, the considered element is centered at the origin and one/two receivers are located on the z-axis with distances R_0 to the element[2]. Assume that the width of the element $\Delta z = \lambda/4$ and the size of the element is small compared to R_0. Thus, the Green's function can be reduced to a function of z', i.e., $G_{yy}(z') = \beta e^{-jk|R_0 - z'|}/(4\pi|R_0 - z'|)$, where $\beta = j\omega\mu_0 + \frac{k^2}{j\omega\epsilon_0}$. In this example, we consider that the induced currents are only present on the front and back surfaces of the element. As illustrated in Fig. 5.2, we denote the surface density of the currents on the incident side and on the transmission side as J_1 and J_2, respectively. Under these assumptions, the

[2]For illustration purposes, the dimensions of this figure is not to scale.

integration in (5.2) and (5.3) simply reduce to two-sum:

$$T_m = J_1 \cdot G_{yy}\left(|R_0 + \Delta z/2|\right) + J_2 \cdot G_{yy}\left(|R_0 - \Delta z/2|\right), \tag{5.12}$$

$$R_m = J_1 \cdot G_{yy}(|R_0 - \Delta z/2|) + J_2 \cdot G_{yy}(|R_0 + \Delta z/2|). \tag{5.13}$$

Note that both J_1, J_2, and G_{yy} are complex values with amplitudes and phases. Exploiting the fact that $R_0 \gg \Delta z$ and $e^{jk\Delta z} = e^{j\pi/2}$, the macroscopic T&R coefficients of this element can be further simplified as:

$$T_m = G_0\left(J_1 \cdot e^{j\pi/2} + J_2\right), \text{ and, } R_m = G_0\left(J_1 + J_2 \cdot e^{j\pi/2}\right), \tag{5.14}$$

where $G_0 = \beta e^{|R_0 - \Delta z/2|}/(4\pi R_0)$. Here, (5.14) reveals the relation between the surface current configuration, i.e., J_1, J_2 and the T&R coefficients. Suppose that the surface currents have the same amplitudes and we rewrite them as $J_1 = |J_0|e^{j\phi_1}$ and $J_2 = |J_0|e^{j\phi_2}$. The reflecting-only RISs, transmitting-only RISs, and STAR-RISs can be modeled by the phase differences of the currents, i.e., $\phi_1 - \phi_2$, according to Table 5-A.

RIS Types	Transmitting-Only	Reflecting-Only	STAR
Configuration of J_y	$\phi_2 - \phi_1 = \pi/2 \pm 2\pi n$	$\phi_1 - \phi_2 = \pi/2 \pm 2\pi n$	$\phi_2 - \phi_1 = \pi \pm 2\pi n$
T&R Amplitudes	$\lvert T_m\rvert = 1$, $\lvert R_m\rvert = 0$	$\lvert R_m\rvert = 1$, $\lvert T_m\rvert = 0$	$\lvert T_m\rvert = \lvert R_m\rvert = 1/\sqrt{2}$

Table 5-A: Relations between RIS types, T&R coefficients and distribution of $J_y(\mathbf{r}')$, where $n = 0, 1, 2, \cdots$.

Note that the configuration shown in the above table are not the only way to achieve these three RIS types. In practice, the current may exhibit a continuous distribution within each element and have x and z components as well. As a result, the STAR-RIS elements can potentially achieve more complex and intricate phase-shift control. For example, the overall T&R coefficients for an element may change with the angle of arrival or different polarization of the incident signal [63]. In this work, we only focus on scalar currents, i.e., $\mathbf{J}(\mathbf{r}') = \hat{\mathbf{y}} J_y(\mathbf{r}')$.

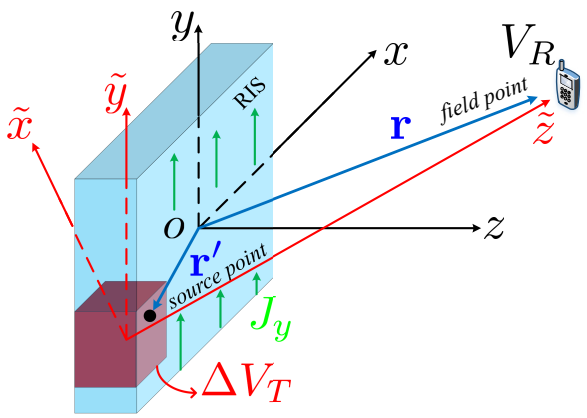

Figure 5.3: Geometrical illustration of transmitting/reflecting-only RIS and ΔV_T.

5.3 Fundamental Performance Limits of Transmitting-Only and Reflecting-Only RIS-Aided Single-User Scenario

Exploiting the proposed channel model, we first analyze the fundamental performance limits for transmitting-only and reflecting-only RISs, including the best achievable end-to-end channel gain, the maximum degrees of freedom of the end-to-end channel, and the power scaling law. The performance analysis of STAR-RIS-aided multi-user scenario is presented in the next section. As illustrated in Fig. 5.3, assume that the user is located in the x-z plane. Thus, the kernel function defined in (5.8) can be calculated since the geometry of the problem is given. Based on the Green's tensor in (5.5), the kernel function should take the following form:

$$K(\mathbf{r}_1', \mathbf{r}_2') = \int_{V_R} \beta^2 \frac{\exp\left[-jk(|\mathbf{r}-\mathbf{r}_2'| - |\mathbf{r}-\mathbf{r}_1'|)\right]}{16\pi^2 |\mathbf{r}-\mathbf{r}_1'||\mathbf{r}-\mathbf{r}_2'|}, \tag{5.15}$$

where $\beta = j\omega\mu_0 + \frac{k^2}{j\omega\epsilon_0}$.

5.3.1 Field Boundary

In previous studies, the field boundary is usually considered to be $r_b = \frac{2L^2}{\lambda}$ [64], where L is the largest dimension of the smart surface aperture. However, this result does not consider the angular position of the receiver, nor the physical size of the receiver. In our

work, we investigate the field boundary exploiting the kernel function given in (5.15). For a receiver to be located within the far-field regime of the RIS, the phase-term in (5.15) should not vary within the receiving volume V_R [62, eq. (88)]. At the same time, the phase-term should also stay roughly constant for any two source point $\mathbf{r}_1'$ and $\mathbf{r}_2'$ within V_T. If we use half of a period as the criteria, we have the following:

$$\frac{k\Delta x_{T,max}\Delta x_{R,max}}{r} < \frac{\pi}{2}, \text{ and } \frac{k\Delta y_{T,max}\Delta y_{R,max}}{r} < \frac{\pi}{2}, \tag{5.16}$$

where $\Delta x_{T,max}$, $\Delta y_{T,max}$ are the largest dimensions of V_T in the x/y direction and $\Delta x_{R,max}$, $\Delta y_{R,max}$ are the largest dimensions of V_R. By multiplying these results, we have the following lemma:

Lemma 4. *The boundary between the radiating near-field and far-field, i.e., the maximum distance for near-field communication is given by:*

$$r_b = \sqrt{\frac{2\Delta x_{T,max}\Delta y_{T,max}}{\lambda}}\sqrt{\frac{2\Delta x_{R,max}\Delta y_{R,max}}{\lambda}}, \tag{5.17}$$

or equivalently, for a user with a distance of r to fall within the far-field regime of the RIS, the maximum volume of the RIS is given as follows:

$$\Delta V_{T,max} = \frac{\lambda r}{2\Delta x_{R,max}}\frac{\lambda r}{2\Delta y_{R,max}}2\Delta z_{T,max}, \tag{5.18}$$

where $z_{T,max}$ is the maximum width of the RIS.

Proof. The proof is straightforward by multiplying the results in (5.16) and exploiting $k = 2\pi/\lambda$, and $\Delta V_{T,max} = (2\Delta x_{T,max})(2\Delta y_{T,max})(2\Delta z_{T,max})$. □

Remark 13. *According to **Lemma** 4, the field boundary not only depends on the size of the RIS, but also on the carrier frequency and the aperture size of the receiver. The near-field region expands with the increase of carrier frequency and the size of the receiver. For example, if the receiving device is also a large intelligent surface (LIS) [65], then the*

field boundary r_b will be significantly larger so that near-field effect need to be considered. In Table 5-B, we provide the value of r_b for several typical communication scenarios.

	f_c	λ_c	RIS dimension	Receiver dimension	Boundary (r_b)
1	1000 MHz	0.3 m	0.5 m	0.1 m	0.33 m
2	5 GHz (802.11a)	60 mm	0.5 m	0.1 m	1.67 m
3	10 GHz	30 mm	0.5 m	0.1 m	3.33 m
4	10 GHz	30 mm	0.5 m	0.5 m	16.67 m
5	60GHz (802.11ay)	5 mm	0.5 m	0.1 m	20 m
6	$\sim$ 500 THz (Li-Fi)	$\sim$ 600 nm	0.5 m	0.1 m	$\sim 1.6 \times 10^5$ m

Table 5-B: Position of the near-field/far-field boundary.

As can be observed from the above table, for wireless communication in higher frequency, the volume of usable near-field regime is significantly larger. Moreover, for visible light frequency, if the RIS dimension is still considered to be in the order of magnitude of meters, the position of the field boundary is farther than any practical communicating distances. This indicates that near-field effect should always be considered for visible light communication. As will be discussed in later sections, the near-field channel has higher degrees of freedom compare to the far-field channel.

5.3.2 An Upper Bound of the End-to-End Channel Gain

According to previous results discussed in **Remark 12**, to obtain the best available received power for the receiver V_R, we need to find the eigenfunction and eigenvalues of $K(\mathbf{r}_1', \mathbf{r}_2')$, i.e., to solve for $J_y(\mathbf{r}_1')$ in the integral equation (5.11). In order to keep our derivations cleaner, we simply the kernel function. Recall in (5.8), the kernel function measures the averaged received power (within V_R) for two source point. If $\mathbf{r}_1'$ and $\mathbf{r}_2'$ are two far away from each other, their corresponding kernel will tend to zero due to the fast oscillating phase terms in (5.15). As a result, in (5.7), the integral can be separately evaluated within smaller volumes of sizes ΔV_T whose sizes are given in (5.18). Since we are now evaluating the integral in smaller volumes, we can assume that each volume of ΔV_T and V_R are far apart compared with their sizes. As a result, exploiting the paraxial

approximation, the kernel function can be expressed as follows [62]:

$$K(\mathbf{r}_1', \mathbf{r}_2') = \beta^2 \int_{V_R} \frac{1}{(4\pi r)^2} F(\mathbf{r}_1') F^*(\mathbf{r}_2') \exp\left[-\frac{jk\tilde{x}(\tilde{x}_1' - \tilde{x}_2')}{r} - \frac{jk\tilde{y}(\tilde{y}_1' - \tilde{y}_2')}{r}\right] \mathrm{d}V_R, \tag{5.19}$$

where

$$F(\mathbf{r}') = \exp\left\{-jk\left[\tilde{z}' - \frac{1}{2r}\left((\tilde{x}')^2 + (\tilde{y}')^2\right)\right]\right\} \tag{5.20}$$

is the focusing phase function within V_T and r is the distance between the chosen small volume of ΔV_T and V_R, $\tilde{x}'$, $\tilde{y}'$, and $\tilde{z}'$ are the coordinates of the source point $\mathbf{r}'$ in the coordinate originated at the center of ΔV_T (as illustrated in Fig. 5.3). For the above approximation to be valid, the phase terms in (5.19) should not osculate within the volume of V_R. Based on **Lemma** 4, this is guaranteed if we take $\Delta V_T \approx \frac{\lambda r}{2\Delta x_{max}} \frac{\lambda r}{2\Delta y_{max}} 2\Delta z_T$. We denote $N = \frac{V_T}{\Delta V_T}$ as the number of smaller volumes which V_T is divided into. Thus, we can evaluate the integral separately within each volume of ΔV_T, i.e.,

$$\int_{V_T} K(\mathbf{r}_1', \mathbf{r}_2') J_y(\mathbf{r}_2') \mathrm{d}^3\mathbf{r}_2' = \sum_{i=1}^{N} \int_{(\Delta V_T)_i} K_i(\mathbf{r}_1', \mathbf{r}_2') J_y(\mathbf{r}_2') \mathrm{d}(\Delta V_T)_i, \tag{5.21}$$

where $i \in [1, N]$ is the index of each volume ΔV_T, r_i is the distance between $(\Delta V_T)_i$ and V_R, and

$$K_i(\mathbf{r}_1', \mathbf{r}_2') = \beta^2 F(\mathbf{r}_1') F^*(\mathbf{r}_2') \frac{V_R}{(4\pi r_i)^2} \tag{5.22}$$

is the value of the kernel function within $(\Delta V_T)_i$. To obtain the upper bound of the channel gain, we assume that $J_y(\mathbf{r}')$ can be configured to a detailed distribution within ΔV_T. According to (5.19), the following current source distribution yields the largest eigenvalue (see also [62, Eq. (92)]):

$$J_y(\mathbf{r}')_i = \begin{cases} F_i(\mathbf{r}')/\sqrt{\Delta V_T}, & \text{if } \mathbf{r}' \in (\Delta V_T)_i \\ 0, & \text{otherwise,} \end{cases} \tag{5.23}$$

where $F_i(\mathbf{r}')$ is the focusing function given in (5.20). Note that for $F_i(\mathbf{r}')$, the coordinate $\tilde{x}-\tilde{y}-\tilde{z}$ used in (5.20) is located at the center of $(\Delta V_T)_i$. The focusing function ensures that the phase terms of all source point $\mathbf{r}'$ within $(\Delta V_T)_i$ add up constructively at V_R. Thus, by substituting (5.23) into (5.21), we have the following theorem.

Theorem 16. *The maximum channel gain between the RIS and a near-field receiver takes the following form:*

$$|h_{\textit{end-to-end}}|^2 = \begin{cases} \frac{DA_T}{4\pi d^2}\left(j\omega\mu_0 + \frac{k^2}{j\omega\epsilon_0}\right)^2 \cdot \sum_{i=1}^{N} \frac{V_R \Delta V_T}{(4\pi r_i)^2}, & \textit{if } V_T > \Delta V_T \\ \frac{DA_T}{4\pi d^2}\left(j\omega\mu_0 + \frac{k^2}{j\omega\epsilon_0}\right)^2 \cdot \frac{V_R V_T}{(4\pi r)^2}, & \textit{if } V_T \leq \Delta V_T. \end{cases} \tag{5.24}$$

Proof. Substituting (5.23) into (5.21) and (5.7), we have the following:

$$|h_{\text{end-to-end}}|^2 = \frac{DA_T}{4\pi d^2}\int_{V_T} J_y^*(\mathbf{r}_1')\sum_i^N \left[\int_{(\Delta V_T)_i} K(\mathbf{r}_1', \mathbf{r}_2')\frac{F_i(\mathbf{r}_2')}{\sqrt{\Delta V_T}}\mathrm{d}(\Delta V_T)_i\right]\mathrm{d}^3\mathbf{r}_1' \tag{5.25}$$

Note that the integration within V_T can be split into N-sum since $J_y(\mathbf{r}_i')$ is zero outside $(\Delta V_T)_i$. Thus, the other integral can be evaluated in a similar way where the focusing function in J_y cancels out the phase terms in the kernel function:

$$|h_{\text{end-to-end}}|^2 = \frac{A_T}{4\pi d^2}\beta^2 \sum_{i=1}^{N} \frac{V_R \Delta V_T}{(4\pi r_i)^2}. \tag{5.26}$$

Finally, by using the definition of β in (5.15), the theorem is proved. □

5.3.3 Maximum Degrees of Freedom of the End-to-End Channel

According to (5.24), the maximum channel gain is a summation of N terms. In the following corollary, we prove that these N components are in fact parallel channels. This demonstrates an important difference between near-field and far-field RIS-aided communication. Within the far-field regime, the channel is a rank-one matrix for free-space transmission. However, as we will show in the next corollary, due to the varying path lengths between different parts of the RIS and the receiver, the near-field end-to-end

channel potentially has higher degrees of freedom.

Corollary 7. *Consider the patch-array-based RIS is composed of $N_T = N_T^x \times N_T^y$ antenna elements with spacing d_T^x and d_T^y along the two directions, and the receiver is composed of $N_R = N_R^x \times N_R^y$ antenna elements with spacing d_R^x and d_R^y along the two directions. For near-field communication, the maximum degrees of freedom for multiplexing is:*

$$N = \begin{cases} \frac{2V_T V_R}{(\lambda r)^2 \Delta z_T \Delta z_R}, & \textit{metasurface-based} \\ \min\{N_T, N_R, 2A_T A_R (\lambda r)^{-2}\}, & \textit{patch-array-based}, \end{cases} \tag{5.27}$$

where r is the distance between the centers of RIS and the receiving volume, z_T and z_R are the maximum width of the RIS and the receiver, respectively, $A_T = (N_T^x - 1)d_T^x (N_T^y - 1)d_T^y$ and $A_R = (N_R^x - 1)d_T^x (N_R^y - 1)d_T^y$ are the aperture of the RIS and receiving antenna array, respectively.

Proof. For the case for metasurface-based RISs, we denote the current distribution within $(\Delta V_T)_i$ as $J_y^{(i)}(\mathbf{r}')$ and its generated E-field within V_R as $E_y^{(i)}(\mathbf{r})$. We only need to prove that $E_y^{(i)}(\mathbf{r})$ are orthogonal to each other within V_R. Note that two functions are orthogonal if their inner product is zero, i.e., $< \mathbf{E}_1, \mathbf{E}_2 >= \int_{V_R} \mathbf{E}_1^T \mathbf{E}_2^* \, dV_R = 0$, where $\mathbf{E}^T$ is the transpose of vector $\mathbf{E}$ and * denotes the complex conjugate. Thus, we have $< E_y^{(p)}(\mathbf{r}), E_y^{(q)}(\mathbf{r}) >=< J_y^{(p)}, \mathcal{K} J_y^{(q)} >$, where $\mathcal{K}$ is the operator of the kernel function K, i.e., $\mathcal{K} J_y(\mathbf{r}') = \int_{V_T} K \cdot J_y(\mathbf{r}') dV_T$. According to (5.23), $< J_y^{(p)}, J_y^{(q)} >= 0$ if $p \neq q$ and $J_y^{(q)}$ is the eigenfunction of $\mathcal{K}$. As a result, we have $< E_y^{(p)}(\mathbf{r}), E_y^{(q)}(\mathbf{r}) >= 0$ for $p \neq q$. This is to say, the number of orthogonal equivalent source functions is equal to the number of volumes ΔV_T, i.e., $N = V_T/(\Delta V_T)$. Finally, by exploiting the expression for ΔV_T in (5.18), the corollary is proved. For the case of patch-array-based RISs, the maximum degrees of freedom is further limited by the number of RIS element (N_T) and the number of receiving antenna (N_R). □

Remark 14. *According to* (5.27)*, for the case where the aperture size of the RIS is*

larger and the carrier frequency is higher, the available DoF is higher. However, utilize these DoF is a challenge due to the lack of RF chains on RISs. In theory, it is possible to send a superimposed signal to the RIS and these parallel signals excited different surface current patterns, and thus, at the receiver, the signals can be independently decoded by summing up the signals with weights according to the eigenfunctions within the V_R [65, Fig. 2].

5.3.4 Power Scaling Law

Next, we present the near-field and far-field power scaling laws. In (5.23), we used normalized currents within V_T, i.e., $\int_{V_T} J_y^* J_y \mathrm{d}V_T = 1$. However, in practice, if we consider the RIS is illuminated by a far-field base station, we need to use the unnormalized currents[3], i.e., $J_y(\mathbf{r}') = F(\mathbf{r}')$. Thus, we have the following corollary:

Corollary 8. *Suppose that the RIS has M elements, the power scaling law is given as follows:*

$$P_r \propto \begin{cases} V_R \sum_i^N \frac{V_{ele}^2}{(4\pi r_i)^2} M_i^2, & \textit{metasurface-based} \\ V_R \sum_i^N \frac{V_{ele}^2}{(4\pi r_i)^2} \left(\frac{\sin(\pi \Delta z_T/\lambda)}{\pi \Delta z_T/\lambda} \right)^2 M_i^2, & \textit{patch-array-based}, \end{cases} \tag{5.28}$$

where P_r is the received power, V_{ele} is the volume of each RIS element M_i is the number of element within $(\Delta V_T)_i$, such that $\sum_{i=1}^N M_i = M$, and Δz_T is the width of the RIS.

Proof. For the case of metasurface-based RISs, the corollary is proved by substituting $J_y(\mathbf{r}') = F(\mathbf{r}')$ into (5.7) and following the similar derivations in **Theorem 16**. For patch-array-based RISs, each element can only perform an uniform phase-shift at a time. Thus, we consider the equivalent current distribution of the mth element as constant, i.e., $J_y(\mathbf{r}') = J_y(\mathbf{r}'_m)$, where $\mathbf{r}'_m$ is the center position of element m. The corollary is proved by substituting $J_y(\mathbf{r}') = J_y(\mathbf{r}'_m)$ into (5.7). □

[3]The unnormalized current is practically-relevant since a larger RIS collects more incident energy. In Theorem 1, however, the normalized current is used since we already involve the aperture area of STAR-RIS (A_T) in the equation.

	Field region	End-to-end channel gain	Degrees of freedom (N)	Power scaling law
Far-field	$r > r_b$	$\propto \frac{V_R V_T}{(4\pi r)^2}$	1	$\propto M^2$
Near-field	$r_r < r \leq r_b$	$\propto \sum_i^N \frac{V_R \Delta V_T}{(4\pi r_i)^2}$	$\frac{2V_T V_R}{(\lambda r)^2 \Delta z_T \Delta z_R}$	$\propto \sum_i^N (M_i^2/r_i^2)$

Table 5-C: Comparing fundamental performance limits of the radiating near-field and far-field regimes,
where r_r indicates the boundary of the reactive near-field. According to antenna theory, this value is typically given by $r_r = 0.62\sqrt{L^3/\lambda}$, where L is the largest dimension of the RIS [66].

Remark 15. *Far away from the field boundary, the power scaling law in* (5.28) *can be further simplified. Within the far-field regime, the volume* $\Delta V_{T,max}$ *given in* (5.18) *is larger than the entire volume of RIS. Thus, the summation can be simply removed and we arrive at the similar far-field power scaling law as given in previous works:*

$$P_r^{\textit{far-field}} \propto V_R \left(\frac{V_{ele}}{4\pi \bar{r}}\right)^2 \cdot M^2, \tag{5.29}$$

Within the near-field region when the volume $\Delta V_{T,max}$ *is smaller or equal to the size of* V_{ele}*, there are only one element within each* $(\Delta V_T)_i$ *and* $N = M$*. Thus, the received power starts to scale linearly with* M*:*

$$P_r^{\textit{near-field}} \propto V_R \sum_{m=1}^{M} \left(\frac{V_{ele}}{4\pi r_m}\right)^2 \approx V_R \left(\frac{V_{ele}}{4\pi \bar{r}}\right)^2 \cdot M, \tag{5.30}$$

where $\bar{r}$ *is the distance between the centers of the RIS and the receiver.*

5.3.5 Summary

For the convenience of the readers, we summarize and compare the performance limits for near-field and far-field regimes as derived in the above subsections in Table 5-C. In summary, the end-to-end channel gain, DoF, and power scaling law exhibit differences between the far-field and near-field regions. The near-field region allows for potentially higher DoF and more complex channel characteristics, while the far-field region follows more conventional power scaling laws with fixed DoF. Understanding these differences is crucial for optimizing the design and performance of RIS-aided wireless communication systems.

5.4 Performance Analysis for the STAR-RIS-Aided Multi-User Scenario

In this section, we extend our analysis to the case where multiple users are simultaneously served by the STAR-RIS. We first consider the case where the multiple users are all within the near-field regime and propose three configuration strategies. Then, we consider the hybrid near-field and far-field case where the transmission-side (indoor) user is within the near-field and the reflection-side (outdoor) user is within the far-field. As illustrated in Fig. 5.4, assume that the total number of user is U. To demonstrate the *STAR* functionality, we assume that the users are located on both sides of the STAR-RIS. According to our proposed channel model, for the multi-user case, the channel gain for user p is given as follows:

$$|h^{(p)}|^2 = \frac{DA_T}{4\pi d^2} \int_{V_T} J_y^*(\mathbf{r}_1') \int_{V_T} K^{(p)}(\mathbf{r}_1', \mathbf{r}_2') J_y(\mathbf{r}_2') \mathrm{d}^3\mathbf{r}_1' \mathrm{d}^3\mathbf{r}_2', \tag{5.31}$$

where $K^{(p)}(\mathbf{r}_1', \mathbf{r}_2')$ is the kernel function corresponding to user p. Similar to the single-user case, we evaluate the above integral within each smaller volumes of sizes ΔV_T. However, the difference is that for the multi-user case, $J_y(\mathbf{r}_2')$ need to be optimized for all users. In the following, we give the fundamental performance limit of STAR-RIS serving multiple near-field users in terms of the sum of their channel gains.

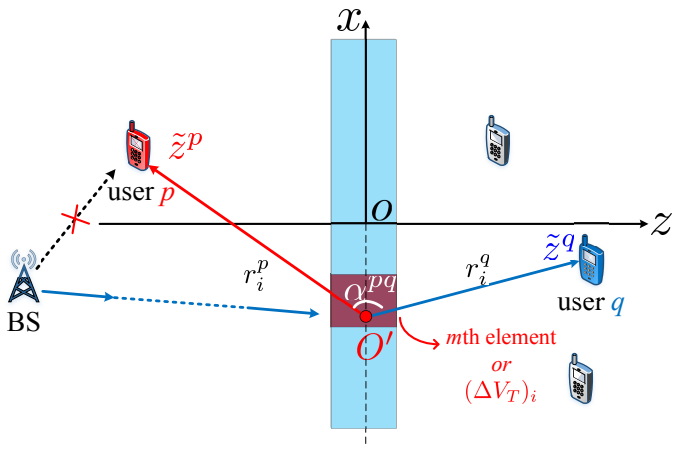

Figure 5.4: Illustration for the STAR-RIS-aided multi-user scenario.

To start with, we exploit the fact that only the term $K^{(p)}(\mathbf{r}'_1, \mathbf{r}'_2)$ in (5.31) is related to the users position. Thus, the sum of the channel gains for all U users can be expressed as follows:

$$\sum_{p}^{U} |h^{(p)}|^2 = \frac{DA_T}{4\pi d^2} \int_{V_T} J_y^*(\mathbf{r}'_1) \int_{V_T} \left(\sum_{p}^{U} K^{(p)}(\mathbf{r}'_1, \mathbf{r}'_2) \right) J_y(\mathbf{r}'_2) \mathrm{d}^3\mathbf{r}'_1 \mathrm{d}^3\mathbf{r}'_2, \tag{5.32}$$

where $\sum_{p}^{U} K^{(p)}(\mathbf{r}'_1, \mathbf{r}'_2)$ is the sum of the kernel function for all users. Here, we assume that the STAR-RIS elements are smaller than $V_{T,max}$. According to last section, the value of the kernel function for user p within the mth element (V_m) is given in (5.22) as $K_i^{(p)}(\mathbf{r}'_1, \mathbf{r}'_2) = \beta^2 F_i(\mathbf{r}'_1) F_i^*(\mathbf{r}'_2) \frac{V_R}{(4\pi r_i^{(p)})^2}$, where the focus function is given as follows:

$$F_i(\mathbf{r}') = \exp\left\{ -jk \left[\tilde{z}'_i - \frac{1}{2r} \left((\tilde{x}'_i)^2 + (\tilde{y}'_i)^2 \right) \right] \right\}. \tag{5.33}$$

Note that the $\tilde{x}'_i$, $\tilde{y}'_i$, and $\tilde{z}'_i$ are evaluated in the *local* coordinate centered at $(\Delta V_T)_i$ where its z_i-axis points in the direction of user p. Thus, calculating the sum of the kernel functions involves transformations between all these *local* coordinates:

$$\sum_{p}^{U} K^{(p)}(\mathbf{r}'_1, \mathbf{r}'_2) = \beta \cdot V_R \sum_{p}^{U} \sum_{i}^{N} \frac{1}{(4\pi r_i^p)^2} F_i^{(p)}(\mathbf{r}'_1) F_i^{(p)*}(\mathbf{r}'_2), \tag{5.34}$$

$$= \frac{\beta \cdot V_R}{(4\pi)^2} \sum_{i}^{N} \left(\sum_{p}^{U} \frac{F_i^{(p)}(\mathbf{r}'_1)}{(r_i^p)^2} F_i^{(p)*}(\mathbf{r}'_2) \right), \tag{5.35}$$

where $F_i^{(p)}(\mathbf{r}')$ is the focus function for $(\Delta V_T)_i$ and user p. Unlike the single-user case in (5.22), variables $\mathbf{r}'_1$ and $\mathbf{r}'_2$ in (5.35) are not separable in the summed kernel functions. As a result, there are no trivial solutions for $\mathbf{J}_y(\mathbf{r}')$ which could maximize the summed channel gain in (5.32). In practice, the channel and positional information of users are difficult to obtain in real time. As a result, we propose three heuristic strategies for configuring $\mathbf{J}_y(\mathbf{r}')$ in the multi-user scenario, namely the power splitting (PS), the selective element grouping (SEG), and the random element grouping (REG) strategies.

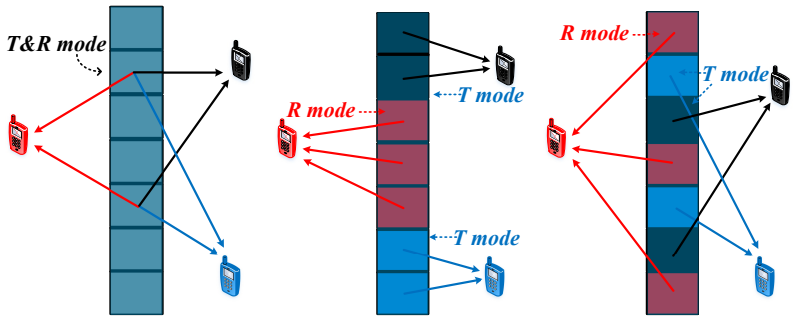

(a) PS (b) SEG (c) REG

Figure 5.5: Conceptual illustration of STAR-RIS configuration strategies, where *T mode* refers to full transmission mode, *T mode* refers to full reflection mode, and *T&R mode* refers to simultaneous transmission and reflection mode [1].

As illustrated in Fig. 5.5, for the PS strategy, all the STAR-RIS elements split their power equally to simultaneously serve all users. For the REG and SEG strategies, elements are divided into U groups so that each group has roughly M/U elements. Elements in each group are dedicated to serve one single user. In REG, the element grouping is randomly assigned whereas in SEG, we select M/U elements which are closest to the user on the STAR-RIS. In the following, we discuss the current distribution configuration and performance of these three strategies in detail.

5.4.1 Power Splitting (PS) Strategy

As illustrate in Fig. 5.5(a), in PS strategy, all STAR-RIS elements simultaneously serve all users. To achieve that, for the mth element, the current is configured as the linear superposition of the focusing functions for all users, normalized by the volume of the element (V_m), i.e.,

$$J_{y,m}(\mathbf{r}') = \sum_{p=1}^{U} F_m^{(p)}(\mathbf{r}') / \left(\sqrt{V_m A_m}\right), \tag{5.36}$$

where $F_m^{(p)}(\mathbf{r}')$ is the focus function for user p within the mth element (defined in (5.20)) and $V_m A_m = \int_{V_m} ||\sum_{p=1}^{U} F_m^{(p)}(\mathbf{r}')|| \mathrm{d}V_m$ is the normalization factor. Next, we evaluate the channel gain for the users. To obtain tractable results, we further assume that the size of each STAR-RIS element is small compared to r_i^p. Thus, the kernel function for

the mth element can be reduced to $K_m^{(p)}(\mathbf{r}'_1, \mathbf{r}'_2) \approx \frac{\beta^2 V_R}{(4\pi r_m^p)^2} e^{-jk\tilde{z}_1^p} e^{+jk\tilde{z}_2^p}$, where $\tilde{z}_{1/2}^p$ is the z-coordinate of the source point $\mathbf{r}'_{1/2}$ in its own orientates originated at the center of the mth element and r_m^p is the distance between the mth element and user p. With this simplification, the end-to-end channel gain can be formulated in a closed-form expression.

Theorem 17. *For the PS strategy, the end-to-end channel gains for user q is given as follows:*

$$|h^{(q)}|^2 = \frac{DA_T\beta^2}{4\pi d^2} \sum_{m=1}^{M} \frac{V_R V_m}{(4\pi r_m^q)^2 A_m} \left(1 + \sum_{p\neq q} \mathrm{sinc}(\xi_m^{pq})\right)^2, \tag{5.37}$$

where where $\beta = j\omega\mu_0 + \frac{k^2}{j\omega\epsilon_0}$ is the constant defined earlier, $\xi_m^{pq} = \pi \cdot (1 - \cos\alpha_m^{pq})\Delta z_m/\lambda$, Δz_m is the width of each STAR-RIS element, and α_m^{pq} is the angle between $O'p$ and $O'q$, for O' being the center of the mth element, as illustrated in Fig. 5.4.

Proof. See Appendix C.1. □

5.4.2 Random Element Grouping (REG) Strategy

As illustrate in Fig. 5.5(c), in REG strategy, the STAR-RIS elements are randomly assigned to focus a single user. Similar to the last subsection, we assume that the STAR-RIS elements are small so that within the volume of ΔV_T, there are multiple elements. Thus, the current configuration for REG strategy is given as follows:

$$J_{y,m}(\mathbf{r}')_i = \begin{cases} F_m^{(p)}(\mathbf{r}')/\sqrt{V_m}, & \text{if } \mathbf{r}' \in V_m \text{ and } m \in \mathcal{M}^p \\ 0, & \text{otherwise,} \end{cases} \tag{5.38}$$

where $F_m^{(p)}$ is the focus function for user p within V_m defined in (5.20) and $\mathcal{M}^p$ denotes the group of elements chosen to focus user p. For this configuration, we show the channel gain in the following theorem.

Theorem 18. *For the REG strategy, the end-to-end channel gains for user p are given*

as follows:

$$|h^{(p)}|^2 = \frac{DA_T\beta^2}{4\pi d^2}\sum_{i=1}^{N^{(p)}}\frac{V_R V_m}{(4\pi r_i^p)^2}\left(M_i^{(p)} + \sum_{q\neq p} M_i^{(q)}\mathrm{sinc}(\xi_i^{pq})\right)^2, \tag{5.39}$$

where $r_i^{(p)}$ *is the distance between the center of* $(\Delta V_T)_i$ *and user* p, V_m *is the volume of each STAR-RIS element,* $M_i^{(p)}$ *is the number of elements in* $(\Delta V_T)_i$ *whose phase shifts are optimized for user* p, $N^{(p)} = \frac{2V_T V_R}{(\lambda r^p)^2 \Delta z_T \Delta z_R}$ *is the achievable degrees of freedom for user* p, $\xi_i^{pq} = \pi \cdot (1 - \cos\alpha_i^{pq})\Delta z_m/\lambda$, Δz_m *is the width of each STAR-RIS element, and* α_i^{pq} *is the angle between* $O'p$ *and* $O'q$, *for* O' *being the center of* $(\Delta V_T)_i$, *as illustrated in Fig. 5.4.*

Proof. See Appendix C.2. □

Remark 16. *The channel gain for user* p *should reduce to the single-user case if all elements are configured for this user. This can be easily verified by letting* $M_i^{(q)} = 0$ *in* (5.37). *In other cases, the channel gain for a given user is always smaller compared to the upper bound given in* (5.24). *This gap is determined by the argument of* ξ_i^{pq}, *which itself depends on the locations of the users.*

5.4.3 Selective Element Grouping (SEG) Strategy

The path lengths between the near-field user and different STAR-RIS elements varies significantly. Thus, unlike in the far-field region, element grouping has a greater effect on the overall channel gains for all users. As illustrated in Fig. 5.5(b), for the SEG strategy, the elements which are closest to one user are all assigned to this particular user. In this case, the STAR-RIS can be regrouped into U volumes, the pth volume contains all elements assigned to user p. The channel gain can be calculated as follows:

Corollary 9. *For the SEG strategy, the end-to-end channel gains for user* p *are given*

as follows:

$$|h^{(p)}|^2 = \frac{DA_T\beta^2}{4\pi d^2}\left(\sum_{i\in\mathcal{V}^p}\frac{V_R V_m}{(4\pi r_i^p)^2}M_i^2 + \sum_{i'\in\mathcal{V}^q, q\neq p}\frac{V_R V_m}{(4\pi r_{i'}^p)^2}\left(M_{i'}\mathrm{sinc}(\xi_{i'}^{pq})\right)^2\right), \tag{5.40}$$

where $\mathcal{V}^p$ denotes the volume of STAR-RIS which is assigned to user p, the index i denotes the volume $(\Delta V_T)_i$, r_i^p is the distance between $(\Delta V_T)_i$ user p, M_i is the number of elements within $(\Delta V_T)_i$.

Proof. Since SEG is a special case of REG strategy, (5.40) can be derived from (5.39) by using the fact all element within $(\Delta V_T)_i$, $i \in \mathcal{V}^p$ is assigned to user p and thus $M_i^q = 0$ if $q \neq p$. □

Remark 17. *The performance of SEG strategy is strictly better than that of the REG strategy. Comparing the the results in* (5.39) *and* (5.40)*, we have $r^p \leq r_i^p$, $\forall i$. Thus, for each element, the coefficients in the SEG is larger than those in the REG strategy. This difference is more significant within the near-field regime due to the greater differences between path-lengths r_i^p. However, to obtain the element grouping configuration for SEG, positional information for all users is required which may significantly increase the overhead of the channel estimation procedure.*

5.4.4 Performance Analysis in the Hybrid Near-Field and Far-Field Regimes

In the above sections, we investigated the performance of the PS, SEG, and REG strategies within the near-field regime. However, in practical applications, users could be located in both the near-field and the far-field regimes. Here, we evaluate the performance of STAR-RISs in the hybrid near-field and far-field regimes. Specifically, we inves-

f_c	λ_c	z_{STAR}	L_{STAR}	$A_{F/N}$	r_b	r_{SF}	r_{SN}
30GHz	9.9mm	0.05m	0.5m	$0.01\mathrm{m}^2$	10m	2m	20m

Table 5-D: Parameters for the considered hybrid near-field and far-field scenario.

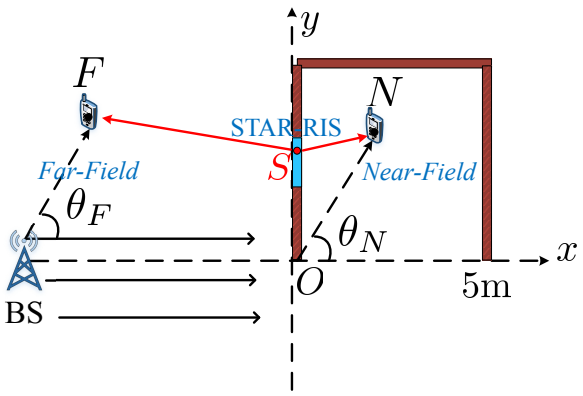

Figure 5.6: Geometrical setup for the considered hybrid near-field and far-field scenario.

tigate an outdoor-to-indoor communication scenario where the STAR-RIS is deployed on the window to simultaneously transmit and reflect wireless signals to indoor and outdoor users, respectively. As illustrated in Fig. 5.6, we consider the case where mobile users are located both indoor and outdoor. The origin O is at bottom left of the room. The BS is far from the origin and its main lobe is pointing in the x-direction. Thus, the wireless signal can be regarded as a plane wave near the origin. As shown in the figure, the wireless signal cannot penetrate walls and can only enters through the opened bottom edge of the room (x-axis) or through the STAR-RIS on the y-axis. For simplicity, we further assume that the system is translation invariant in the z-direction. In terms of multiple access, we assume that all users are served simultaneously. This can be achieved by employing frequency division multiple access. Furthermore, we assume that the base station antenna follows the 3GPP model where the radiation pattern within each sector is as follows [67]:

$$D(\theta) = -\min\left\{12\left(\frac{\theta}{\theta_{3\text{dB}}}\right)^2, 30dB\right\}, \tag{5.41}$$

where $\theta_{3\text{dB}} = 65^\circ$ is the horizontal 3 dB beamwidth.

As illustrated in Fig. 5.6, user F is an outdoor, far-field receiver in the direction of θ_F with respect to the BS. User N is an indoor user where the angle between ON and the x-axis is θ_N. In the following, we investigate how the end-to-end channel gain for the two users change with θ_F and θ_N.

5.4.4.1 Distribution of Signal Strength Without STAR-RISs

First, we consider the benchmark scenario without STAR-RIS. Assuming the wall along the y-axis is completely sealed so that the signal cannot penetrate. Nevertheless, a small portion of the signal strength can still be received by user F and N. This is because for user N, the wireless signal is diffracted at point O, and for user F, there are sidelobes of the BS antenna which radiates towards the horizontal direction of θ_2. According to the radiation pattern given in (5.41), the channel gain between BS and user F can be expressed as follows:

$$\left|h^F_{\text{end-to-end}}\right| \propto -\min\left\{12\left(\frac{\theta_F}{\theta_{3\text{dB}}}\right)^2, 30dB\right\}\cdot\frac{A_F}{r_{OF}}, \tag{5.42}$$

where A_F is the aperture area of user F and r_{OF} is the length of OF. Here, we assume that the contribution of the reflected signals (by the wall) at user P is weak and can be neglected. For user N, the received signal power can also be expressed in terms of θ_N and distance ON. According to [26, eq. (39)], the angular distribution of the signal power within the shadow edge (the first quadrant in Fig. 5.6) can be expressed as follows[4]:

$$\left|h^N_{\text{end-to-end}}\right| \propto \frac{A_N}{k^2 r_{ON}\lambda\sin^2\theta_N}, \tag{5.43}$$

where A_N is the aperture area of user N and r_{ON} is the length of ON. It is shown in (5.43) that the channel gain for user N falls off inversely with $\sin^2\theta_N$ and the distance r_{ON}. This is consistent with common intuition that the top-left corner of the room should have the worst signal (see Fig. 5.11(a) for the simulated result for the indoor radiation power distribution).

5.4.4.2 Distribution of Signal Strength With the aid of STAR-RIS

To improve the channel gain for both the outdoor and indoor users, we open a window in the wall on the y-axis and deploying a STAR-RIS. As illustrated in Fig. 5.6, the STAR-RIS is plotted as a blue rectangle. Exploiting the criteria given in (5.17), we identify the

[4]Here, the secondary reflections from the walls are neglected.

field boundary for the STAR-RIS and user pair. According to the parameters in Table 5-D, the field boundary is $r_b = 10$ m. This indicates that the indoor user N always located within the near-field region and the outdoor user can be considered as far-field if the distance $r_{SF} > 10$ m. Next, we calculate the critical volume given in **Lemma** 4:

$$\Delta V_T^{F/N} = \frac{(\lambda r_{SF/SN})^2}{2A_{F/N}} z_{\text{STAR}} \approx 2.5 \times 10^{-4} \text{ m} \cdot r_{SF/SN}^2. \tag{5.44}$$

For near-field user N, we have $r_{SN} = 2$ m, then we have $\Delta V_T^N \approx 0.02$ m$^2 \cdot z_{\text{STAR}}$. This means that the degrees of freedom of the channel between STAR-RIS and user N is $N^N = V_T/\Delta V_T \approx 12$. For far-field user F, we have $r_{SF} = 20$ m, then $\Delta V_T^F \approx 2$ m$^2 \cdot z_{\text{STAR}}$. This volume is significantly larger than the STAR-RIS since the volume of STAR is only $V_{\text{STAR}} = 0.25$ m$^2 \cdot z_{\text{STAR}}$.

To further obtain the channel gains for the indoor and outdoor users, we consider the use of the three proposed STAR-RIS configuration strategies, i.e., PS, REG, and SEG strategies.

Corollary 10. *For the PS strategy, the end-to-end channel gains between the BS and user P/Q through STAR-RIS are given as follows:*

$$|h_{PS}^F|^2 = \frac{D_0 A_T \beta^2}{4\pi d^2} \frac{V_R V_{STAR} (1 + \text{sinc}(\xi^{FN}))^2}{(4\pi r^F)^2 A_m}, \tag{5.45}$$

$$|h_{PS}^N|^2 = \frac{D_0 A_T \beta^2}{4\pi d^2} \sum_{m=1}^{M} \frac{V_R V_m}{(4\pi r_m^N)^2 A_m} (1 + \text{sinc}(\xi_m^{FN}))^2, \tag{5.46}$$

where $D_0 = D(\theta = 0)$ is the directivity of the BS antennas, A_T is the aperture size of STAR-RIS, d is the distance between BS and STAR-RIS, V_R is the volume of the receiver, V_{STAR} is the volume of the STAR-RIS, $\xi^{FN} = \pi(1 - \cos\alpha^{FN})\Delta z_m/\lambda$, α^{FN} is the angle between user F and user N observed at the center of STAR-RIS, and V_m is the volume of each STAR-RIS element.

Proof. For the far-field user F, its distances and angles to different STAR-RIS elements

are almost the same. Thus, by using $r_m^F = r^F$ and $\xi_m^{FN} = \xi^{FN}$ in (5.37), (5.45) can be proved. For the near-field user F, its channel gain follows the same form in (5.37). □

Corollary 11. *For the REG and SEG strategy, the end-to-end channel gains between the BS and user P/Q through STAR-RIS are given as follows:*

$$|h_{REG}^F|^2 = |h_{SEG}^F|^2 = \frac{D_0 A_T \beta^2}{4\pi d^2} \frac{V_R V_m}{(4\pi r^F)^2} \left[(M^F)^2 + (M^N \mathrm{sinc}(\xi^{FN}))^2 \right], \tag{5.47}$$

$$|h_{REG}^N|^2 = \frac{D_0 A_T \beta^2}{4\pi d^2} \sum_{i=1}^{12} \frac{V_R V_m}{(4\pi r_i^N)^2} \left[M_i^N + M_i^F \mathrm{sinc}(\xi_i^{FN}) \right]^2, \tag{5.48}$$

$$|h_{SEG}^N|^2 = \frac{D_0 A_T \beta^2}{4\pi d^2} \left[\sum_{i \in \mathcal{V}^Q} \frac{V_R V_m}{(4\pi r_i^N)^2} M_i^2 + \sum_{i \in \mathcal{V}^F} \frac{V_R V_m}{(4\pi r_i^N)^2} \left(M_i \mathrm{sinc}(\xi_i^{FN}) \right)^2 \right], \tag{5.49}$$

where $\xi_i^{FN} = \pi(1 - \cos\alpha_i^{FN})\Delta z_m/\lambda$, α_i^{FN} *is the angle between user* F *and user* N *observed at* $(\Delta V_T)_i$, *and* M_i *is the number of STAR-RIS element within* $(\Delta V_T)_i$.

Proof. For the far-field user F, its distances and angles to different STAR-RIS elements can be regarded as the same. Thus, by using $r_m^F = r^F$ and $\xi_m^{FN} = \xi^{FN}$ in (5.39), (5.47) can be proved. For the near-field user N, its channel gain follows similar forms in (5.48) and (5.49). □

Remark 18. *Comparing the channel gains for user* F *and* N *with and without the aid of STAR-RIS, it can be observed that the undesirable angle dependencies with* θ_F *and* θ_N *in* (5.42) *and* (5.43) *are removed in the STAR-RIS-aided links. This will be further illustrated in our numerical results (see Fig. 5.12).*

5.5 Numerical Results

In this section, numerical results are provided to validate the proposed Green's function based channel model and power scaling laws for the transmitting/reflecting-only RIS-aided single user scenario. We also present simulation results for the three STAR-RIS

configuration strategies and coverage simulation results for the STAR-RIS-aided multi-user scenario.

5.5.1 Transmitting/Reflecting-Only RIS-Aided Single User Scenario

5.5.1.1 RIS Power Scaling Laws

In Fig. 5.7 we investigate the power scaling laws for the near-field and far-field regimes proposed in (5.30) and (5.29), respectively. In the simulation, we assume that the receiver is located at a distance of $d = 0.7$ m to the center of RIS and the dimension of the receiver is $z_R \approx 1.0$ cm. The number of RIS elements range from 1 to 16 and its size range from 1 cm to 10 cm. The wavelength of the carrier signal is 0.01 m. As can be observed from the figure, since the position of the receiver is fixed, the user is within the far-field regime if the RIS has smaller size and the user is within the near-field regime if the RIS becomes larger. Within the far-field regime, the power scales with M^2, as derived in (5.29). However, by increasing the size of the RIS, this quadratically growth cannot continue forever. As the size of the RIS reach the volume correspond to the boundary position, i.e., (5.18), the user falls into the near-field regime. As indicated with the red dashed line, a linear power scaling law is observed, as derived in (5.30).

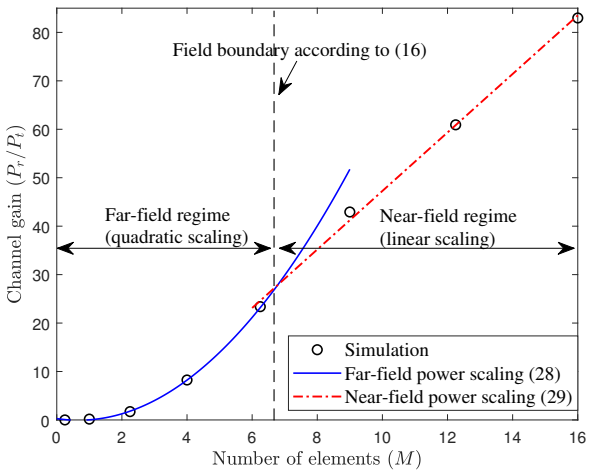

Figure 5.7: Near-field and far-field power scaling laws of transmitting/reflecting-only RIS.

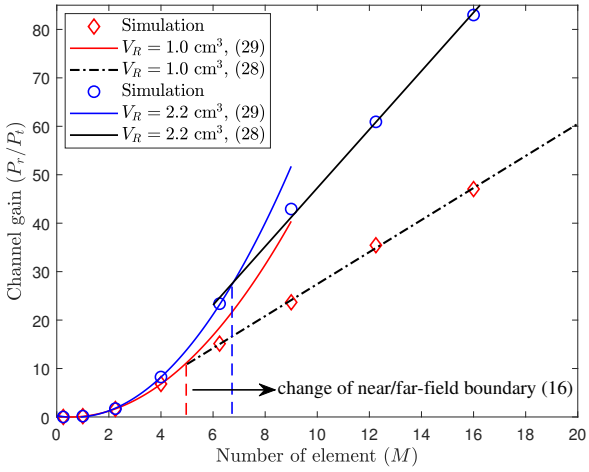

Figure 5.8: Power scaling laws of metasurface-based transmitting/reflecting-only RIS with receivers of different sizes.

5.5.1.2 Power Scaling Laws for Receivers with Different Sizes

In Fig. 5.8, we investigate the power scaling laws of conventional RISs for receivers with different sizes. The red markers are the simulation results for a receiver with volume $V_R = 1$ cm^3 while the blue markers are the results for $V_R = 1.7$ cm^3. As can be shown in the figure, the simulations fit well with the derived near-field and far-field power scaling laws. Within the far-field regime, both receivers exhibit linear power scaling. As derived in (5.29), the blue curve has a larger slope because its larger volume. Also, the field boundary positions differ for the two receivers.

5.5.2 STAR-RIS-Aided Multi-User Scenario

5.5.2.1 Channel Gain and Field Boundary for STAR-RISs

Fig. 5.9 illustrates the results for the upper bound of the end-to-end channel gain. The STAR-RIS is configured to split power equally on both sides. However, the volumes of the receivers are different. User 1 (receiver with $d < 0$) has a dimension of $V_R = 0.125$ cm^3 and the user 2 with $d > 0$ has volume $V_R = 1$ cm^3. The STAR-RIS is located at the center with $d = 0$. As shown in the figure, within the near-fields, the channel gains of both users oscillates with the change of distance. In contrast, the far-field regimes, the

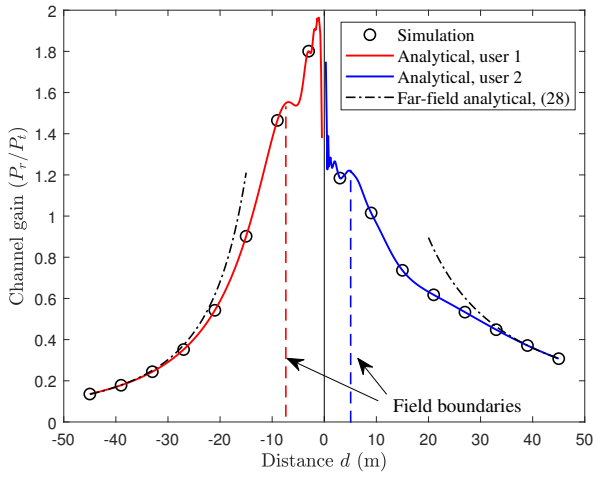

Figure 5.9: Simulation and analytical results for the channel gain of metasurface-based STAR-RIS.

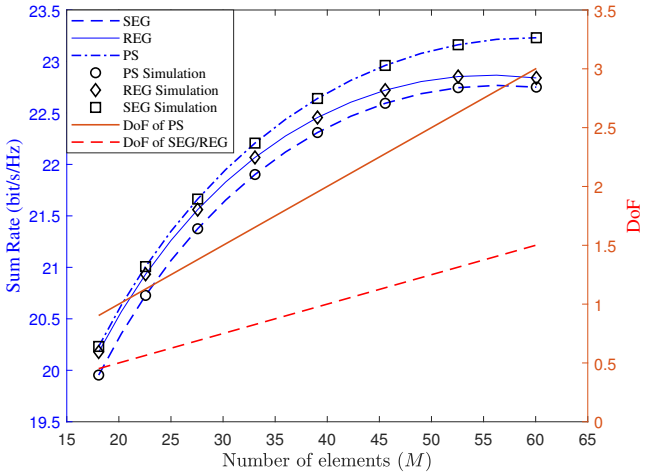

Figure 5.10: Simulation and analytical results for the sum rate and DoFs for two near-field users.

channel gain follows the d^{-2} dependency as derived in (5.29).

5.5.2.2 Comparison between the PS, REG, and SEG Strategies within Near-Field Regime

In Fig. 5.10, we investigate the sum rate performance of the three proposed configuration strategies. We consider two users, p and q, located on different sides of the STAR-RIS. Both users are located in the x-z plane with $d = 0.5$ m to the center of the STAR-RIS

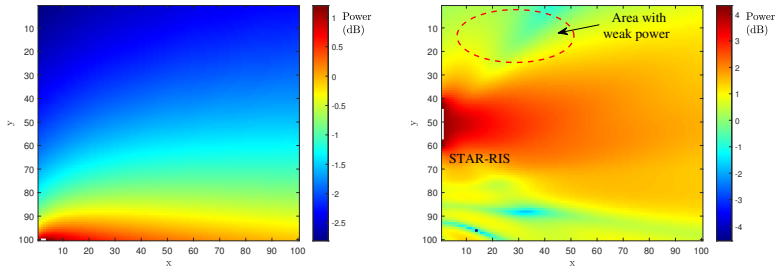

(a) Without STAR-RIS or window (b) Open window

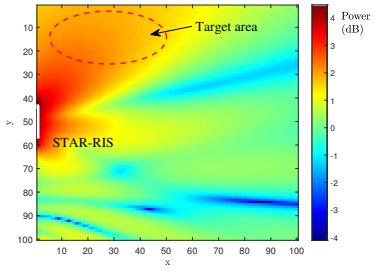

(c) STAR-RIS

Figure 5.11: Simulated indoor radiation coverage.

(refer to Fig. 5.4 for the coordinate system). Specifically, we assume that $x_p = -0.5$ m and $x_q = 0.3$ m. The carrier wavelength is set at $\lambda_c = 0.01$ m and the dimension of the STAR-RIS ranges from 20 cm to 60 cm. The dimension of the receiver is $z_R \approx 1$ cm. As can be observed in the figure, the SEG strategy outperform both REG and PS strategies, and the PS strategy has the lowest sum rate. This result is in accordance with remark 17. Although SEG and REG strategies achieve higher sum rate, the DoFs of their corresponding channels are lower than the PS strategy. Recall that in (5.27), the DoF is proportional to the total volume of operating STAR-RIS elements. In SEG and REG, only a portion of the elements are designated to one user. As a result, for a particular user, the volume V_T is smaller than the overall volume of the STAR-RIS. Thus, Fig. 5.10 reveals a trade-off between the sum rate and channel DoF within the near-field regime. A similar trade-off is also present in the far-field regime between the beam-forming gain and multiplexing gain of RISs or phased-array antennas [68].

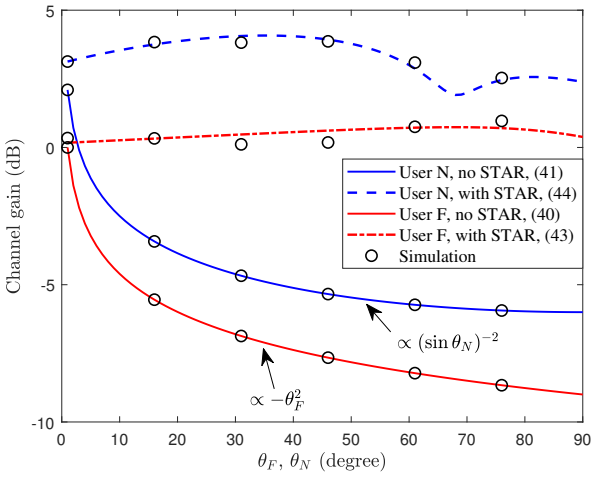

Figure 5.12: Simulation and analytical results for the channel gains of user F and user N.

5.5.3 STAR-RIS within Hybrid Near-Field and Far-Field Regimes

5.5.3.1 Radiation Pattern for the Indoor User

In Fig. 5.11 we plot the radiation pattern for the indoor space under the setting of the case study. Fig. (5.11(a)) shows the power distribution without the STAR-RIS deployed. The radiation pattern agrees with the derived analytical result given in (5.43). The power falls off with $1/\sin^2\theta_N$, where θ_N is angle between the x-axis and the field-point N. Thus, the power is the lowest near the top-left corner of the room. Fig. (5.11(b)) shows the power distribution if a square window with size $L = 0.5$ m is opened on the center of the wall. The open window performs no passive beamforming and only lets the signal penetrates the wall within the area of $L^2 = 0.25$ m^2. As can be observed, the signal power is significantly better near the center of the room. However, near the top-left and bottom-left of the room, there are still regions where the signal power falls under 0 dB. Without the passive beamforming of STAR-RIS, the signal power within these regions cannot be improved because the geometrical setting of the room is fixed. In Fig. (5.11(c)), we show the power distribution in which the STAR-RIS is configured to improved the signal power near the top-left of the room. It can be observed that the STAR-RIS improves the received power within the area of interest by about 5 dB

compared to the case without STAR-RIS and 3 dB compared to the case with an open window (without passive STAR-RIS beamforming). Furthermore, by employing the three proposed STAR-RIS configuration strategies, it is also achievable to improve the signal power at multiple locations simultaneously.

5.5.3.2 Channel Gains for the Outdoor and Indoor Users

In Fig. 5.12, we investigate the channel gains for user F amd N as a function of the angles of θ_F and θ_N (as illustrated in Fig. 5.6). The indoor and outdoor channel gains with and without deploying the STAR-RIS are compared where the STAR-RIS adopts the PS strategy. As can be observed, the channel gains for both users without STAR-RIS decreased significantly with θ_F and θ_N, as derived in (5.42) and (5.43). Specifically, the channel gain for the indoor user N decreases with $(\sin\theta_N)^{-2}$ and the channel gain for the outdoor user F decreases with $-\theta_F^2$. The channel gains for both users are significantly improved with the aid of STAR-RIS. With the STAR-RIS deployed, the undesired angle-dependency is removed and the channel gains for both users remain high (compared to the case where $\theta_{F/N} = 0$ but without STAR-RIS) within the entire angle range of $(0°, 90°)$.

5.6 Summary

In this chapter, a channel model based on Green's function method was proposed for investigating the performance limit of metasurface-based RISs and STAR-RISs. Instead of modeling the RIS elements with the transmission and/or reflection coefficients, we used the distribution of the induced electric currents within the metasurface-based RIS. We also gave revealed how transmitting-only RISs, reflecting-only RISs and STAR-RISs can be achieved by configuring the distribution of the induced electric current. For the single-user scenario with transmitting/reflecting-only RISs, the upper bound of the end-to-end channel gain was derived by choosing the current distribution that is optimized for the receiver. In addition, the position of the near-field and far-field boundary, the maximum DoF of the channel, and the power scaling law were derived. It was shown that

the size of RIS, the carrier signal frequency, and the size of the receiver all affect the above performance metrics. For the multi-user scenario with STAR-RISs, we proposed three configuration strategies, i.e, the PS, SEG, and REG strategies. Closed-form expressed were derived for the channel gains for all three strategies. By comparing the results, it was shown that the SEG performs better than REG, especially within the near-field regime. We further analyzed the performance of STAR-RIS in the hybrid near-field and far-field regimes. Specifically, we conducted study where the STAR-RIS assists the transmission of the signal from outdoor to indoor. Analytical and numerical results shown that the STAR-RIS significantly improved the signal power in the indoor "blind zone". The results obtained in this chapter confirm the effectiveness of metasurface-based RIS-aided and STAR-RIS-aided wireless communication.

Chapter 6

Conclusions and Future Works

6.1 Contributions and Insights

This thesis proposes, models, and analyzes the novel concept of STAR-RIS. At the time of writing, STAR-RISs has had a noticeable impact in the field of wireless communications and has also attracted research interest from the industry. In the following, I conclude this thesis by summarizing the four-year journey I have taken with the research of RISs:

The idea of manipulating the communication channel fascinated me at first glance. However, as soon as I started researching on the topic of RISs in early 2019, I quickly found that there was a huge knowledge gap between the physical/hardware and communication aspects of RISs. This imposed challenges for both performance analysis and system optimization for RIS-aided communication networks. For example, it was not clear what is the channel response of the RIS, how to formulate path-loss of the cascaded RIS channel, and what statistical multipath fading model is appropriate for RISs. These burning questions motivated me to reconcile knowledge in Electromagnetics, antenna theory, and information theory. My first transaction paper [8] gave answers to the above questions and proposed a Rician fading-based statistical channel model for RISs. It was later commonly accepted that multiplicative path-loss and Rician fading

should be used to modeled the RIS-aided channels. Motivated by this small achievement, my colleagues and I dug deeper into the hardware capabilities of RISs and realized state-of-the-art design of RISs didn't fully exploit the tunability of the smart surface. In 2020, after carefully researching the field of metamaterial and reviewing theories in Electromagnetics, I found out that it is possible to achieve independent phase-shift control of both reflected and transmitted signals through adjusting the electric and magnetic impedances of the metasurface. By allowing not only the electric surface currents but also the magnetic (vortex) currents, the symmetry constraint of RISs is removed. In my second work [24], I proposed a way to simultaneously control signals on the two sides of the RISs and presented the hardware model, signal model, and channel models. This was to connect the physical quantities (EM field) with the communication quantities (channel and signals powers). Also, the paper rigorously proved that the proposed method can simultaneously achieve full diversity order for users on both sides, which significantly outperform the conventional reflecting-only RISs. We later named this invention as simultaneous transmitting and reflecting RISs (STAR-RISs). STAR-RIS has opened new lines of research and enabled various promising technologies for future-generation wireless networks. Inspired by the fundamental STAR signal model and channel models proposed in [2], significant research interest has been focused on STAR-RIS-aided wireless communication, including beamforming design, multi-user communications, resource allocation, and channel estimation. STAR-RISs have also attracted research interest from industry. After STAR-RIS is proposed, our team also received criticisms on the practicability of independent phase-shift control. Since RISs are envisioned to be a purely passive device (with no power source), some researchers have raised doubts about the independent capability of the STAR-RIS to adjust the phase-shifts of both transmitted and reflected signals, given that RISs are intended to function as purely passive devices without a power source.. However, I wasn't disheartened by these challenging criticisms. Instead, I proved that the STAR-RISs are practically relevant even for under the passive-lossless constraint. After several discussions and collaborations with the antenna design group in our university, in [60], I proposed the signal model and practical phase-shift

designs for passive-lossless STAR-RISs. It was proved that the transmission and reflection phase-shifts are indeed coupled. However, full diversity order can still be achieved on both sides exploiting the proposed diversity-preserving phase-shift design. Moreover, in [69], my co-authors and I discussed how STAR-RIS can be implemented. This work is the first time where smart surfaces are classified into the spatially-discrete patch-array case and the spatially-continuous metasurface case.

6.2 Future Works

6.2.1 Extensions of Current Works

In this subsection, the potential applications for STAR-RISs in future generation wireless communication networks are discussed in the following.

6.2.1.1 STAR-RIS-Aided NOMA

RISs are capable of enhancing the performance of NOMA networks by providing distinct channel conditions for NOMA users. Nevertheless, for RIS-aided NOMA networks, all the users have to be set in the reflection space. As a result, the channel conditions of users in reflected space are generally similar, which is not easy to fully exploit the benefits of NOMA. STAR-RISs can properly solve this issue. More particularly, a pair of users at the transmission and reflection side can be grouped together for facilitating NOMA. As a result, asymmetric channel conditions among transmit and reflect users can be realized and thus high-performance gain over OMA can be achieved by adopting flexible resource allocation. There are still several research opportunities and challenges in STAR-RIS-NOMA design based on our proposed framework, for example, 1) the appearance of STAR-RIS makes the joint user assignment and beamforming design challenging, how to efficiently align and allocate different NOMA users into suitable beams and to provide proper optimization for mitigating intra-cluster and inter-cluster interference requires further study. 2) Another unsolved problem is facilitating coupled phase-shift design in the proposed STAR-RIS-NOMA framework.

6.2.1.2 STAR-RIS-Aided Physical Layer Security (PLS) Enhancement

Compared to the reflecting only RIS, the appearance of STAR-RIS provides extended coverage from 180 degrees to 360 degrees. Nevertheless, such changes inevitably result in full-space wiretapping. As a result, the PLS issue needs to be reinvestigated. As the basic model of STAR-RIS consists of both transmitted and reflected users, we can broadly classify the PLS problems into a couple of categories, namely, external eavesdropper case and internal eavesdropper case. 1) For the external eavesdropper case, as shown in Fig. 9a, a few eavesdroppers try to eavesdrop on both transmit and reflect users. 2) For the Internal Eavesdropper case, due to the multi-user nature of STAR-RIS, internal eavesdropping may exist. More particularly, for a pair of transmitted and reflected users, one transmitted/reflected user may wiretap the other reflect/transmit user's confidential information, which is regarded as STAR-RIS networks in presence of an untrusted user. Such cases pose new challenges for the PLS in STAR-RIS networks and therefore deserve further research efforts. Furthermore, how to invoke artificial noise to further enhance the PLS for both external and internal eavesdropping cases is another promising direction to carry out.

6.2.1.3 STAR-RIS-Aided Integrated Sensing and Communication (ISAC)

ISAC is a technology that serves the dual purpose of sensing and communication through a shared hardware platform and waveform. Typically, ISAC relies on the line-of-sight (LoS) channel to facilitate the sensing function between the ISAC transceiver and the desired targets. Carrying out target sensing without LoS links presents a significant challenge. However, RIS can overcome this issue by establishing virtual LoS links between the RIS and desired targets. This capability enhances the sensing coverage and resolution. Compared to conventional reflecting-only RIS, STAR-RIS offers several advantages for ISAC. Firstly, STAR-RIS can enable full-space sensing and communication, which is a straightforward benefit. Secondly, STAR-RIS opens up new possibilities for carrying out sensing and communication in physically separated spaces using a shared hardware platform and waveform. Specifically, the STAR-RIS can divide the full space into two

halves: the sensing half-space and the communication half-space. The ISAC node transmits a joint signal, which is then split by the STAR-RIS into two separate signals, for carrying out sensing and communication in the respective half-spaces. Nevertheless, STAR-RIS also poses new challenges. The transmission and reflection properties of the STAR-RIS can result in mixed echo signals from the two half-spaces in the link between the STAR-RIS and the ISAC node, making it difficult to identify the signals. Additionally, the multiple hops of the echo signal and energy splitting at the STAR-RIS can result in a low sensing SNR, leading to low sensing accuracy.

6.2.1.4 STAR-RIS-Aided Near-Field Communications (NFC)

In order to meet the demanding criteria for spectral efficiency, energy efficiency, latency, coverage, and other performance metrics in 6G, STAR-RIS follows primary developmental trends. The first involves the utilization of extremely large surfaces, while the second focus on the use of high-frequency bands, such as millimetrewave (mmWave) and THz bands. These two trends will inevitably cause the near-field effect. More particularly, the Rayleigh distance, which is known as the boundary between the near-field and the far-field, is proportional to the aperture of the antenna array and the operating frequency. An illustrative example of the challenges posed by the near-field effect can be observed in the case of a surface with a dimension of 0.5 meters operating at a frequency of 60 GHz. In this scenario, the near-field region can extend up to 100 meters, signifying that the impact of the near-field effect cannot be disregarded. In comparison to the conventional reflecting-only RIS, which features a fixed near-field region due to the fixed size and shape of the surface, the STAR-RIS offers a novel approach to dynamically adjust the near-field region through the allocation of distinct elements for transmission and reflection. Hence, it is imperative to consider the impact of the near-field effect in the development of advanced STAR-RIS-aided systems.

Appendix A

Proofs in Chapter 3

A.1 Proof of Theorem 1

Since the expressions for the outage probabilities for OMA and NOMA in (3.34), (3.36), and (3.37) have similar forms, the respective proofs required for **Theorem 1** can be given at the same time. According to the system model presented in Section 3.4, both $|g_m|$ and $|h_m^R|$ follow Rician distributions. Hence, $h_m = \beta^R |g_m||h_m^R|$ is the product of two independent Rician random variables. The PDF of $|h_m|$ can be expressed as follows [56]:

$$\begin{aligned} f_{|h_m|}(x) &= \frac{x}{(\beta^R)^2 \beta_h \beta_g} e^{-(K_h+K_g)} \\ &\cdot \sum_{i=0}^{\infty} \sum_{l=0}^{\infty} \frac{\left(\frac{\alpha_h \sqrt{x}}{2\beta_h}\right)^{2i} \left(\frac{\alpha_g \sqrt{x}}{2\beta_g}\right)^{2l}}{i!l!\Gamma(i+1)\Gamma(l+1)} \left(\frac{\beta_h}{\beta_g}\right)^{\frac{i-l}{2}} K_{i-l}\left(\frac{x}{\beta^R \sqrt{\beta_h \beta_g}}\right), \end{aligned} \tag{A.1.1}$$

where $\alpha_{h/g}^2 = \frac{K_{h/g}\Omega_{h/g}}{K_{h/g}+1}$, $\beta_{h/g} = \frac{\Omega_{h/g}}{2(K_{h/g}+1)}$, $\Gamma(x)$ denotes the Gamma function, and K_n is the modified Bessel function of the second kind. For the asymptotic behavior, we consider the PDF of $|h_m|$ near the origin using a Taylor series expansion:

$$f_{|h_m|}(x) = \frac{e^{-(K_h^R+K_g)}}{(\beta^R)^2 \beta_h \beta_g} \cdot x + o(x), \tag{A.1.2}$$

where $o(\cdot)$ is the little-o notation and $o(f(x))$ denotes a function which is asymptotically smaller than $f(x)$. The Laplace transform of the asymptotic PDF in (A.1.2) is given by:

$$\mathcal{M}_{|h_m|}(t) = \mathcal{L}\{f_{|h_m|}\} = \frac{1}{(\beta^R)^2\beta_h\beta_g} e^{-(K_h^R+K_g)} t^{-2} + o(t^{-2}). \tag{A.1.3}$$

According to (3.40), the overall channel of user R is the summation of $M+1$ terms. Using the convolution theorem of the Laplace transform, we obtain the Laplace transform of the asymptotic PDF of H^R as follows:

$$\begin{aligned}\mathcal{M}_{|H^R|}(t) = \mathcal{L}\{f_{|H^R|}\} = \left(\frac{e^{-(K_h+K_g)}}{(\beta^R)^2\beta_h\beta_g}\right)^M \cdot \frac{2(K_d^R+1)}{\Omega_d^R} \\ \cdot e^{-K_d^R} t^{-2M-2} + o(t^{-2M-2}).\end{aligned} \tag{A.1.4}$$

Finally, $f_{|H^R|}(x)$ can be obtained by performing the inverse transform term by term. By further substituting $\beta_{h/g}$ with $\frac{\Omega_{h/g}}{K_{h/g}+1}$, we arrive at

$$\begin{aligned}f_{|H^R|}(x) = \frac{2^{M+1}(K_h^R+1)^M(K_g+1)^M(K_d+1)}{(\beta^R)^{2M}\Omega_h^M\Omega_g^M\Omega_d} \\ \cdot e^{-MK_h^R - MK_g - K_d} \cdot \frac{x^{2M+1}}{(2M+1)!}.\end{aligned} \tag{A.1.5}$$

Finally, **Theorem 1** can be proved by integrating the asymptotic PDF in (A.1.5) according to (3.36) and (3.34) for NOMA and OMA.

A.2 Proof of Lemma 1

As shown in Section 3.5, for the secondary user for the PS-PSC strategy and both users for the DP-PSC strategy, the STAR-RIS-aided channel (h_s^χ) can be expressed as follows:

$$h_s^\chi = |g|\beta^\chi \sum_{m=1}^{M} |h_m^\chi| \exp\{j(\angle h_d^\chi + \delta_m^\chi)\}, \tag{A.2.1}$$

where δ_m^χ models the phase error of the mth element for user χ. For both considered PSC strategies, this phase error is bounded, i.e., $|\delta_p^\chi - \delta_q^\chi| \leq \Delta^\chi, \forall p, q$. For the PS-PSC

strategy, $\Delta^T = \pi$, and for the DP-PSC strategy, $\Delta^R = \Delta^T = \pi/2$. Hence, as was shown in [17, Corollary 2], the PDF of the magnitude of h_s^χ can be approximated by a Rician distribution:

$$f_{|h_s^\chi|}(x) = \frac{x}{\beta^2} e^{-\frac{x^2+\alpha^2}{2\beta^2}} I_0\left(\frac{x\alpha}{\beta}\right), \tag{A.2.2}$$

where

$$\alpha = M\mathbb{E}[|H_m|]\text{sinc}(\frac{\Delta^\chi}{2}),\ \beta^2 = \frac{M}{2}\mathbb{E}[|H_m|^2][1-\text{sinc}(\Delta^\chi)]. \tag{A.2.3}$$

Thus, for the PS-PSC strategy, the PDF of $|h_s^\chi|$ is obtained by plugging $\Delta^T = \pi$ into (A.2.2).

Appendix B

Additional Results in Chapter 4

B.1 OMA Baseline

Recall that in Chapter 4, we formulated the outage probability for OMA users. Consider FDMA, the outage probabilities for user r and t in OMA are given as follows:

$$P_{out}^{r} = \Pr\{\mathrm{SNR}_{r}^{\mathrm{O}} < 2^{2\tilde{R}_r} - 1\} \tag{B.1}$$

$$P_{out}^{t} = \Pr\{\mathrm{SNR}_{t}^{\mathrm{O}} < 2^{2\tilde{R}_t} - 1\}, \tag{B.2}$$

where $\mathrm{SNR}_{r/t}^{\mathrm{O}} = p\left|\sum_m^M g_m^{r/t} h_m e^{j\phi_m^{R/T}}\right|^2/\sigma_0^2$ is the SNR for FDMA. Note that in (B.1), the factor 2 before the data rate in the exponent $2^{2\tilde{R}_r}$ comes from the fact that each user can only occupy half the bandwidth in FDMA. By defining $\gamma_{r/t} = 2^{2\tilde{R}_{r/t}}$, the outage probabilities in (B.1) and (B.2) reduce to $\Pr\{|H_{r/t}|^2 < \gamma_{r/t}\sigma_0^2/p\}$. Thus, the outage probability of both users can be expressed as the cumulative distribution function of $|H_{r/t}|^2$, which is given as follows:

$$P_{out}^{r/t} = 1 - Q_{1/2}\left(\frac{\sqrt{M}\mu^{r/t}}{\sigma^{r/t}}, \frac{\sqrt{\gamma_{r/t}}\sigma_0}{\sqrt{pM}\beta^{R/T}\sigma^{r/t}}\right), \tag{B.3}$$

where $\mu^{\chi} = \frac{1}{4}\sqrt{\frac{\pi\Omega_h}{(K_h+1)}}L_{1/2}(-K_h)\sqrt{\frac{\pi\Omega_g^{\chi}}{(K_g^{\chi}+1)}}L_{1/2}(-K_g^{\chi})$ is the expectation value of $|h_m||g_m^{\chi}|$, $(\sigma^{\chi})^2 = \Omega_h\Omega_g^{\chi} - (\mu^{\chi})^2$ is its variance, and $Q_{1/2}(x)$ is the Marcum Q-function.

Appendix C

Proofs in Chapter 5

C.1 Proof of Theorem 17

We start from the formulation in (5.31), and substituting the current distribution (5.36) and the approximated kernel function $K_m^{(q)}(\mathbf{r}'_1, \mathbf{r}'_2) \approx \frac{\beta^2 V_R}{(4\pi r_m^q)^2} e^{-jkz_1^q} e^{+jkz_2^q}$ into (5.31), we have the following:

$$|h^{(q)}|^2 = \frac{DA_T}{4\pi d^2} \int_{V_T} J_y^*(\mathbf{r}'_1) \int_{V_T} \sum_m \left[\frac{\beta^2 V_R}{(4\pi r_m^q)^2} e^{-jkz_1^q} e^{-jkz_2^q} \right] J_y(\mathbf{r}'_2) \mathrm{d}^3\mathbf{r}'_1 \mathrm{d}^3\mathbf{r}'_2, \tag{C.1.1}$$

$$= \frac{DA_T}{4\pi d^2} \int_{V_T} \sum_{p=1}^{U} e^{jkz_1^p} \int_{V_T} \sum_m \left[\frac{\beta^2 V_R}{(4\pi r_m^q)^2} e^{-jkz_1^q} e^{jkz_2^q} \right] \sum_{p'=1}^{U} e^{-jkz_2^{p'}} / V_m A_m \mathrm{d}V_T \mathrm{d}V_T. \tag{C.1.2}$$

We first simplify the integration for z_2 within V_T. For each term in the summation of m, if $p' = q$ then the two exponential cancel out. And if $p' \neq q$, the we have the following integration:

$$\int_{V_T} e^{jk(-z_2^q + z_2^{p'})} \mathrm{d}V_T = \int_{V_T} e^{jk(-z_2^q + \cos\alpha_m^{pq} z_2^q)} S_m \mathrm{d}z_2^q = \frac{2\sin\left(k(1-\cos\alpha_m^{pq})\right)}{k(1-\cos\alpha_m^{pq}))} V_m, \tag{C.1.3}$$

where in the first equality, $z_2^{p'}$ is transformed into the coordinate of centered at element m with the z-axis pointing towards user q, α_m^{pq} is the angle between user p and user q from the perspective of the mth element, and S_m is the aperture area of the mth element. The integration of z_1 in (C.1.2) can be evaluated similarly. Thus, by substituting (C.1.3) into (C.1.2), we have:

$$|h^{(q)}|^2 = \frac{DA_T}{4\pi d^2} \sum_m^M \frac{\beta^2 V_m V_T}{(4\pi r_m^q)^2 A_m} \left(1 + \frac{2\sin\left(k(1-\cos\alpha_m^{pq})\right)}{k(1-\cos\alpha_m^{pq})}\right)^2. \tag{C.1.4}$$

C.2 Proof of Theorem 18

Again, we start from the formulation in (5.31), and substituting the current distribution for REG in (5.38) and the approximated kernel function into (5.31), we have the following:

$$|h^{(p)}|^2 = \frac{DA_T}{4\pi d^2} \int_{V_T} J^*_{y,m}(\mathbf{r}'_1) \int_{V_T} \sum_m \left[\frac{\beta^2 V_R}{(4\pi r_m^p)^2} e^{-jkz_1^p} e^{-jkz_2^p}\right] J_{y,m}(\mathbf{r}'_2) \mathrm{d}^3\mathbf{r}'_1 \mathrm{d}^3\mathbf{r}'_2. \tag{C.2.1}$$

For the integration for $\mathbf{r}'_2$ within element m, the value depends on the element's grouping. For the elements assigned for user p, the focusing factor in the kernel function is cancelled by $J_{y,m}(\mathbf{r}'_2)$. However, for other elements, the integrated value yields a similar result as in (C.1.3). Thus, by evaluating the integral within each volume $(\Delta V_T)_i$ the we have:

$$\begin{aligned} &\int_{V_T} \sum_i^{N^{(p)}} \left[\frac{V_R}{(4\pi r_i^p)^2} e^{-jkz_2^p}\right] J_{y,m}(\mathbf{r}'_2) \mathrm{d}^3\mathbf{r}'_2 \\ &= \sum_i \frac{\beta V_R \sqrt{V_m}}{(4\pi r_i^p)^2} \left(M^{(p)} + M^{(q)} \frac{2\sin\left(k(1-\cos\alpha_m^{pq})\right)}{k(1-\cos\alpha_m^{pq})}\right), \end{aligned} \tag{C.2.2}$$

where M_i^p denote the number of element assigned to user p within $(\Delta V_T)_i$. Thus, the overall integration can be calculated as follows:

$$|h^{(q)}|^2 = \frac{DA_T}{4\pi d^2} \sum_i \frac{\beta V_R V_m}{(4\pi r_i^p)^2} \left(M^{(p)} + M^{(q)} \frac{2\sin\left(k(1-\cos\alpha_m^{pq})\right)}{k(1-\cos\alpha_m^{pq})}\right)^2, \tag{C.2.3}$$

References

[1] X. Mu, Y. Liu, L. Guo, J. Lin, and R. Schober, "Simultaneously transmitting and reflecting (STAR) RIS aided wireless communications," *IEEE Trans. Wireless Commun.*, vol. 21, no. 5, pp. 3083–3098, 2022.

[2] M. Alsabah, M. A. Naser, B. M. Mahmmod, S. H. Abdulhussain, M. R. Eissa, A. Al-Baidhani, N. K. Noordin, S. M. Sait, K. A. Al-Utaibi, and F. Hashim, "6G wireless communications networks: A comprehensive survey," *IEEE Access*, vol. 9, pp. 148 191–148 243, 2021.

[3] E. Basar, M. Di Renzo, J. De Rosny, M. Debbah, M.-S. Alouini, and R. Zhang, "Wireless communications through reconfigurable intelligent surfaces," *IEEE Access*, vol. 7, pp. 116 753–116 773, 2019.

[4] Y. Liu, X. Liu, X. Mu, T. Hou, J. Xu, M. Di Renzo, and N. Al-Dhahir, "Reconfigurable intelligent surfaces: Principles and opportunities," *IEEE Commun. Surv. Tutor.*, vol. 23, no. 3, pp. 1546–1577, 2021.

[5] M. Di Renzo, A. Zappone, M. Debbah, M. S. Alouini, C. Yuen, J. de Rosny, and S. Tretyakov, "Smart radio environments empowered by reconfigurable intelligent surfaces: How it works, state of research, and the road ahead," *IEEE J. Sel. Areas Commun.*, vol. 38, no. 11, pp. 2450–2525, 2020.

[6] M. Di Renzo, M. Debbah, D.-T. Phan-Huy, A. Zappone, M.-S. Alouini, C. Yuen, V. Sciancalepore, G. C. Alexandropoulos, J. Hoydis, H. Gacanin *et al.*, "Smart radio environments empowered by reconfigurable ai meta-surfaces: An idea whose time has come," *EURASIP Journal on Wireless Communications and Networking*, vol. 2019, no. 1, pp. 1–20, May 2019.

[7] Y. Li, W. Wang, J. Kong, and M. Peng, "Subcarrier pairing for amplify-and-forward and decode-and-forward OFDM relay links," *IEEE Commun. Lett.*, vol. 13, no. 4, pp. 209–211, 2009.

[8] J. Xu and Y. Liu, "A novel physics-based channel model for reconfigurable intelligent surface-assisted multi-user communication systems," *IEEE Trans. Wireless Commun.*, vol. 21, no. 2, pp. 1183–1196, 2022.

[9] N. DOCOMO. "DOCOMO conducts world's first successful trial of transparent dynamic metasurface". [Online]. Available: www.nttdocomo.co.jp/english/info/media_center/pr/2020/0117_00.html

[10] E. J. Rothwell and M. J. Cloud, *Electromagnetics*. CRC Press, 2018.

[11] I. Vágó, "On the interface and boundary conditions of electromagnetic fields," *Period. Polytech. Elec. Eng.*, vol. 38, no. 2, pp. 79–94, 1994.

[12] W. Tang, M. Z. Chen, X. Chen, J. Y. Dai, Y. Han, M. Di Renzo, Y. Zeng, S. Jin, Q. Cheng, and T. J. Cui, "Wireless communications with reconfigurable intelligent surface: Path loss modeling and experimental measurement," *IEEE Trans. Wireless Commun.*, vol. 20, no. 1, pp. 421–439, 2021.

[13] H. Zhang, S. Zeng, B. Di, Y. Tan, M. Di Renzo, M. Debbah, Z. Han, H. V. Poor, and L. Song, "Intelligent omni-surfaces for full-dimensional wireless communications: Principles, technology, and implementation," *IEEE Commun. Mag.*, vol. 60, no. 2, pp. 39–45, 2022.

[14] M. Nemati, B. Maham, S. R. Pokhrel, and J. Choi, "Modeling ris empowered outdoor-to-indoor communication in mmwave cellular networks," *IEEE Trans. on Commun.*, vol. 69, no. 11, pp. 7837–7850, 2021.

[15] W. Zhu, D. B. Farmer, K. A. Jenkins, B. Ek, S. Oida, X. Li, J. Bucchignano, S. Dawes, E. A. Duch, and P. Avouris, "Graphene radio frequency devices on flexible substrate," *Appl. Phys. Lett.*, vol. 102, no. 23, p. 233102, 2013.

[16] B. O. Zhu, J. Zhao, and Y. Feng, "Active impedance metasurface with full 360 reflection phase tuning," *Scientific reports*, vol. 3, p. 3059, 2013.

[17] N. K. Emani, A. V. Kildishev, V. M. Shalaev, and A. Boltasseva, "Graphene: a dynamic platform for electrical control of plasmonic resonance," *Nanophotonics*, vol. 4, no. 1, pp. 214–223, 2015.

[18] S. Abeywickrama, R. Zhang, and C. Yuen, "Intelligent reflecting surface: Practical phase shift model and beamforming optimization," *arXiv:1907.06002*, 2019.

[19] R. J. Bell, K. R. Armstrong, C. S. Nichols, and R. W. Bradley, "Generalized laws of refraction and reflection," *JOSA*, vol. 59, no. 2, pp. 187–189, 1969.

[20] J. Huang and J. A. Encinar, "Reflectarray antennas, a john wiley & sons," *Inc.,*

Publication, 2008.

[21] F. H. Danufane, M. Di Renzo, J. de Rosny, and S. Tretyakov, "On the path-loss of reconfigurable intelligent surfaces: An approach based on green's theorem applied to vector fields," *arXiv preprint arXiv:2007.13158*, 2020.

[22] H.-T. Chen, A. J. Taylor, and N. Yu, "A review of metasurfaces: physics and applications," *Reports on progress in physics*, vol. 79, no. 7, p. 076401, 2016.

[23] V. Arun and H. Balakrishnan, "Rfocus: Beamforming using thousands of passive antennas," in *17th USENIX Symposium on Networked Systems Design and Implementation (NSDI 20)*. USENIX Association, Feb. 2020, pp. 1047–1061.

[24] J. Xu, Y. Liu, X. Mu, and O. A. Dobre, "STAR-RISs: Simultaneous transmitting and reflecting reconfigurable intelligent surfaces," *IEEE Commun. Lett.*, vol. 25, no. 9, pp. 3134–3138, May, 2021.

[25] R. J. Mailloux, *Phased array antenna handbook*. Artech house, 2017.

[26] H. G. Booker and P. Clemmow, "The concept of an angular spectrum of plane waves, and its relation to that of polar diagram and aperture distribution," *Proceedings of the IEE-Part III: Radio and Communication Engineering*, vol. 97, no. 45, pp. 11–17, 1950.

[27] C. Liaskos, S. Nie, A. Tsioliaridou, A. Pitsillides, S. Ioannidis, and I. Akyildiz, "A new wireless communication paradigm through software-controlled metasurfaces," *IEEE Commun. Mag.*, vol. 56, no. 9, pp. 162–169, 2018.

[28] C. Huang, S. Hu, G. C. Alexandropoulos, A. Zappone, C. Yuen, R. Zhang, M. D. Renzo, and M. Debbah, "Holographic MIMO surfaces for 6G wireless networks: Opportunities, challenges, and trends," *IEEE Wireless Commun.*, vol. 27, no. 5, pp. 118–125, Oct. 2020.

[29] E. Basar, M. Di Renzo, J. De Rosny, M. Debbah, M.-S. Alouini, and R. Zhang, "Wireless communications through reconfigurable intelligent surfaces," *IEEE Access*, vol. 7, pp. 116 753–116 773, 2019.

[30] Ö. Özdogan, E. Björnson, and E. G. Larsson, "Intelligent reflecting surfaces: Physics, propagation, and pathloss modeling," *IEEE Wireless Commun. Lett.*, 2019.

[31] Z. Ding, R. Schober, and H. V. Poor, "On the impact of phase shifting designs on

IRS-NOMA," *IEEE Wireless Commun. Lett.*, vol. 9, no. 10, pp. 1596–1600, 2020.

[32] Z. Zhang, Y. Cui, F. Yang, and L. Ding, "Analysis and optimization of outage probability in multi-intelligent reflecting surface-assisted systems," *arXiv preprint arXiv:1909.02193*, 2019.

[33] M.-A. Badiu and J. P. Coon, "Communication through a large reflecting surface with phase errors," *IEEE Wireless Commun. Lett.*, vol. 9, no. 2, pp. 184–188, 2019.

[34] X. Qian, M. Di Renzo, J. Liu, A. Kammoun, and M. . S. Alouini, "Beamforming through reconfigurable intelligent surfaces in Single-User MIMO systems: SNR distribution and scaling laws in the presence of channel fading and phase noise," *IEEE Wireless Commun. Lett.*, vol. 10, no. 1, pp. 77–81, 2021.

[35] Z. Ding and H. V. Poor, "A simple design of IRS-NOMA transmission," *IEEE Commun. Lett.*, vol. 24, no. 5, pp. 1119–1123, 2020.

[36] M. Fu, Y. Zhou, and Y. Shi, "Intelligent reflecting surface for downlink non-orthogonal multiple access networks," in *2019 IEEE Globecom Workshops (GC Wkshps)*. IEEE, 2019, pp. 1–6.

[37] X. Mu, Y. Liu, L. Guo, J. Lin, and N. Al-Dhahir, "Exploiting intelligent reflecting surfaces in NOMA networks: Joint beamforming optimization," *IEEE Trans. Wireless Commun.*, vol. 19, no. 10, pp. 6884–6898, 2020.

[38] T. Hou, Y. Liu, Z. Song, X. Sun, Y. Chen, and L. Hanzo, "Reconfigurable intelligent surface aided NOMA networks," *IEEE J. Sel. Areas Commun.*, vol. 38, no. 11, pp. 2575–2588, 2020.

[39] Y. Liu, X. Liu, X. Mu, T. Hou, J. Xu, Z. Qin, M. Di Renzo, and N. Al-Dhahir, "Reconfigurable intelligent surfaces: Principles and opportunities," *IEEE Commun. Surv. Tutor.*, Early Access, 2021, doi: 10.1109/COMST.2021.3077737.

[40] C. Huang, A. Zappone, G. C. Alexandropoulos, M. Debbah, and C. Yuen, "Reconfigurable intelligent surfaces for energy efficiency in wireless communication," *IEEE Trans. Wireless Commun.*, vol. 18, no. 8, pp. 4157–4170, Aug. 2019.

[41] A. R. Ndjiongue, T. M. N. Ngatched, O. A. Dobre, and H. Haas, "Towards the use of re-configurable intelligent surfaces in VLC systems: Beam steering," *arXiv*

preprint arXiv:2009.06822, 2020.

[42] X. Mu, Y. Liu, L. Guo, J. Lin, and R. Schober, "Intelligent reflecting surface enhanced indoor robot path planning: A radio map based approach," *IEEE Trans. Wireless Commun.*, Early Access, 2021, doi: 10.1109/TWC.2021.3062089.

[43] G. C. Alexandropoulos, N. Shlezinger, I. Alamzadeh, M. F. Imani, H. Zhang, and Y. C. Eldar, "Hybrid reconfigurable intelligent metasurfaces: Enabling simultaneous tunable reflections and sensing for 6G wireless communications," *arXiv preprint arXiv:2104.04690*, 2021.

[44] N. DOCOMO. "DOCOMO conducts world's first successful trial of transparent dynamic metasurface". [Online]. Available: www.nttdocomo.co.jp/english/info/media_center/pr/2020/0117_00.html

[45] J. Zhang, Z. Li, L. Shao, and W. Zhu, "Dynamical absorption manipulation in a graphene-based optically transparent and flexible metasurface," *Carbon*, vol. 176, pp. 374–382, May 2021.

[46] X. Wang, J. Ding, B. Zheng, S. An, G. Zhai, and H. Zhang, "Simultaneous realization of anomalous reflection and transmission at two frequencies using bi-functional metasurfaces," *Sci. Rep.*, vol. 8, no. 1, pp. 1–8, Jan. 2018.

[47] N. M. Estakhri and A. Alu, "Wave-front transformation with gradient metasurfaces," *Phys. Rev. X*, vol. 6, no. 4, p. 041008, Oct. 2016.

[48] L. La Spada, C. Spooner, S. Haq, and Y. Hao, "Curvilinear metasurfaces for surface wave manipulation," *Sci. Rep.*, vol. 9, no. 1, pp. 1–10, Feb. 2019.

[49] S. Loyka and A. Kouki, "On MIMO channel capacity, correlations, and keyholes: analysis of degenerate channels," *IEEE Trans. Commun.*, vol. 50, no. 12, pp. 1886–1888, 2002.

[50] B. O. Zhu, K. Chen, N. Jia, L. Sun, J. Zhao, T. Jiang, and Y. Feng, "Dynamic control of electromagnetic wave propagation with the equivalent principle inspired tunable metasurface," *Sci. Rep.*, vol. 4, no. 1, pp. 1–7, 2014.

[51] T. L. Marzetta and H. Q. Ngo, *Fundamentals of massive MIMO*. Cambridge University Press, 2016.

[52] C. Wu, C. You, Y. Liu, X. Gu, and Y. Cai, "Channel estimation for STAR-RIS-

aided wireless communication," *IEEE Commun. Lett.*, vol. 26, no. 3, pp. 652–656, 2022.

[53] Y. Liu, X. Mu, J. Xu, R. Schober, Y. Hao, H. V. Poor, and L. Hanzo, "STAR: Simultaneous transmission and reflection for 360° coverage by intelligent surfaces," *IEEE Wireless Commun.*, vol. 28, no. 6, pp. 102–109, 2021.

[54] Y. Liu, Z. Qin, M. Elkashlan, Y. Gao, and L. Hanzo, "Enhancing the physical layer security of non-orthogonal multiple access in large-scale networks," *IEEE Trans. Wireless Commun.*, vol. 16, no. 3, pp. 1656–1672, 2017.

[55] T. Wang, G. Chen, J. P. Coon, and M.-A. Badiu, "Study of intelligent reflective surface assisted communications with one-bit phase adjustments," in *Proc. IEEE Global Commun. Conf. (GLOBECOM)*, 2020, pp. 1–6.

[56] M. K. Simon, *Probability distributions involving Gaussian random variables: A handbook for engineers and scientists*. Springer, 2002.

[57] F. Gao, B. Wang, C. Xing, J. An, and G. Y. Li, "Wideband beamforming for hybrid massive MIMO terahertz communications," *IEEE J. Sel. Areas Commun.*, vol. 39, no. 6, pp. 1725–1740, Jun. 2021.

[58] D. V. Hinkley, "On the ratio of two correlated normal random variables," *Biometrika*, vol. 56, no. 3, pp. 635–639, 1969. [Online]. Available: http://www.jstor.org/stable/2334671

[59] H. Tohyama and H. Mizuno, "23-GHz band GaAs MESFET reflection-type amplifier," *IEEE Trans. Microw. Theory Tech.*, vol. 27, no. 5, pp. 408–415, 1979.

[60] J. Xu, Y. Liu, X. Mu, R. Schober, and H. V. Poor, "STAR-RISs: A correlated T&R phase-shift model and practical phase-shift configuration strategies," *IEEE J. Sel. Top. Signal Process.*, vol. 16, no. 5, pp. 1097–1111, 2022.

[61] D. Porter, D. S. Stirling, and P. David, *Integral equations: a practical treatment, from spectral theory to applications*. Cambridge university press, 1990, vol. 5.

[62] D. A. Miller, "Communicating with waves between volumes: evaluating orthogonal spatial channels and limits on coupling strengths," *Applied Optics*, vol. 39, no. 11, pp. 1681–1699, 2000.

[63] X. Liu, F. Yang, M. Li, and S. Xu, "Generalized boundary conditions in surface

electromagnetics: Fundamental theorems and surface characterizations," *Applied Sciences*, vol. 9, no. 9, p. 1891, 2019.

[64] C. A. Balanis, *Antenna theory: analysis and design*. John wiley & sons, 2015.

[65] D. Dardari, "Communicating with large intelligent surfaces: Fundamental limits and models," *IEEE J. Sel. Areas Commun.*, vol. 38, no. 11, pp. 2526–2537, 2020.

[66] K. T. Selvan and R. Janaswamy, "Fraunhofer and Fresnel distances: Unified derivation for aperture antennas," *IEEE Antennas Propag. Mag*, vol. 59, no. 4, pp. 12–15, Aug. 2017.

[67] M. Rebato, L. Resteghini, C. Mazzucco, and M. Zorzi, "Study of realistic antenna patterns in 5G mmwave cellular scenarios," in *2018 IEEE International Conference on Communications (ICC)*, 2018, pp. 1–6.

[68] L. Zheng and D. Tse, "Diversity and multiplexing: a fundamental tradeoff in multiple-antenna channels," *IEEE Trans. Inf. Theory*, vol. 49, no. 5, pp. 1073–1096, 2003.

[69] J. Xu, Y. Liu, X. Mu, J. T. Zhou, L. Song, H. V. Poor, and L. Hanzo, "Simultaneously transmitting and reflecting intelligent omni-surfaces: Modeling and implementation," *IEEE Veh. Technol. Mag.*, vol. 17, no. 2, pp. 46–54, 2022.